A Liquid Xenon Scintillation Detector to Search for the Lepton Flavor Violating Muon Decay with a Sensitivity of 10^{-13}

Ryu Sawada
Department of Physics, School of Science
University of Tokyo

November 28, 2008

Abstract

The MEG experiment searches for a rare muon decay $\mu^+ \rightarrow \mathrm{e}^+\gamma$, which is forbidden in the standard model. Several new theories beyond the standard model predict branching ratio of the decay just below the current experimental limit. The MEG experiment aims sensitivity of 10^{-13} where most of predictions are covered. The discovery of the muon decay is a probe for new physics beyond the standard model.

To realize such a high sensitivity, a new liquid xenon detector was developed for measuring energy, position and time of gamma rays. The detector is the largest xenon detector ever made. Characteristics of liquid xenon, Large atomic number, high density, large scintillation output and fast decay time allow to build a detector with excellent resolutions and high efficiency. It consists of more than 800 litters of liquid xenon and 846 photo-multiplier tubes. We performed beam tests and evaluated resolutions by using a prototype. During the prototype test, fundamental techniques to operate the detector and to analyze data were developed. The construction of the final detector was completed in 2007. An engineering run was conducted in the year to preparing triggers, to evaluate detector performance and to collect a small amount of physics data. The resolutions of the detector during the engineering run were estimated by using gamma rays from pion decays. The estimated best values of resolutions for 54.9 MeV gamma rays are 2.1 ± 0.2 %, 5.9 ± 1.4 mm and 121 ± 8 psec for energy, position and time respectively. Based on the measured resolutions and counting rate in 2007, it was confirmed that the gamma ray detector has a sufficient performance to improve the current experimental limit and realize a sensitivity better than 10^{-12} in 2008.

Contents

Chapter 1

Introduction

1.1 Physics motivation

The standard model of particle physics successfully explains most of particle phenomena tested by experiments precisely. A missing piece is a direct observation of the Higgs particles, which LHC experiment is expected to find.

One phenomenon that is not explained by the standard model is the neutrino oscillation. The original standard model assumes massless neutrinos and does not allow flavor violating processes in the lepton sector, thus a modification of the theory is needed to explain the phenomenon.

Neutrinos can obtain masses by introducing heavy right-handed neutrinos close to GUT scale into the theory. Addition of such neutrinos requires to introduce new mass scales in addition to that of the standard model. It implies the existence of new physics beyond the standard model.

It is widely believed that the standard model would be a low energy approximation of more fundamental theories such as Super Symmetric Model (SUSY), Grand Unified Theory(GUT), Extra Dimensions and String Theories because the standard model does not answer some questions known as "Gauge problem", "Fermion problem", "Higgs/hierarchy problem", "Strong CP problem" and "Graviton problem". With a minimum modification of the standard model to introduce non-zero neutrino mass, $\mu^+ \to \mathrm{e}^+\gamma$ can occur through flavor mixing of neutrinos. However the branching ratio is far below from observable rate.

$$Br(\mu \to \mathrm{e}\gamma) = \frac{3\alpha}{32\pi} \left| \sum_{i=2,3} U^*_{\mu i} U_{ei} \frac{\Delta m^2_{1i}}{m^2_W} \right| < 10^{-54} \tag{1.1}$$

where U is Pontecorvo-Maki-Nakagawa-Sakata matrix and $\Delta^2_{ij} = m^2_{\nu i} - m_{\mu j}2$.

In SU(5) SUSY-GUT, LFV occurs in the right handed slepton sector as shown in fig.1.1. So, in the model, $\mu^+ \to \mathrm{e}^+_L\gamma$ occurs, while $\mu^+ \to \mathrm{e}^+_R\gamma$ does not occur. These two processes could be distinguished from angular distribution by an experiment with polarized muon decays. Predicted branching ratio is shown in fig1.2 with various values of input parameters of M_2 (the SU(2) gaugino mass) and $\tan\beta$ (the ratio of the two Higgs vacuum expectation values) as a function of the mass of right-handed selectron. The minimal SU(5) SUSY-GUT is ruled out by the experimental limit on the lifetime of protons.

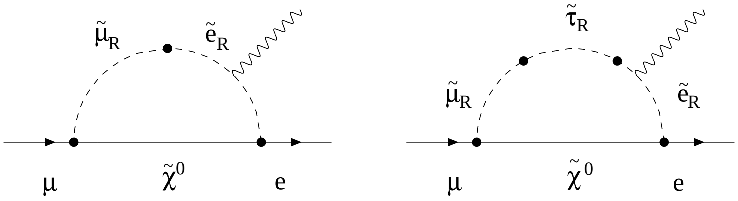

Figure 1.1: Diagrams of $\mu^+ \to e^+\gamma$ in SU(5) SUSY GUT.

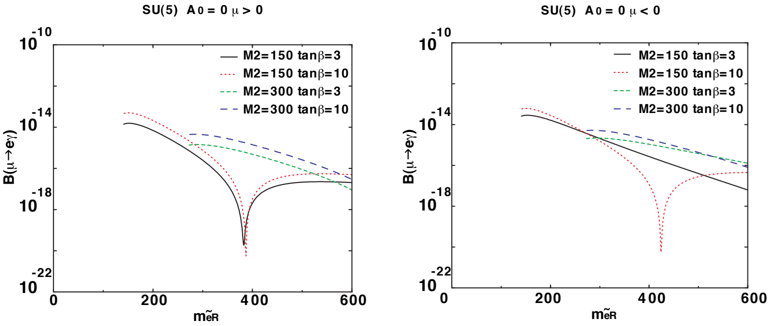

Figure 1.2: Predicted Br($\mu^+ \to e^+\gamma$) in SU(5) SUSY GUT.[1]

In SO(10) SUSY-GUT, Br($\mu^+ \to e^+\gamma$) is enhanced by contribution of the third generation sleptons as shown in fig.1.3. In the model, LFV occurs in the both right and left handed slepton sectors. Figure 1.4 shows predictions by the model. They are close to the current experimental bound, which is 1.2×10^{-11}.

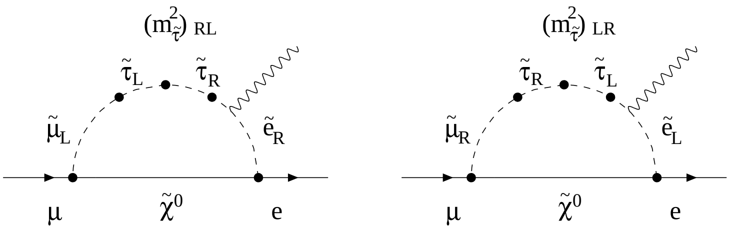

Figure 1.3: Diagrams of $\mu^+ \to e^+\gamma$ in SO(10) SUSY GUT.

From a study of muon anomalous magnetic moment by E821 experiment at Brookhaven National Lab, it was found that there is a significant difference

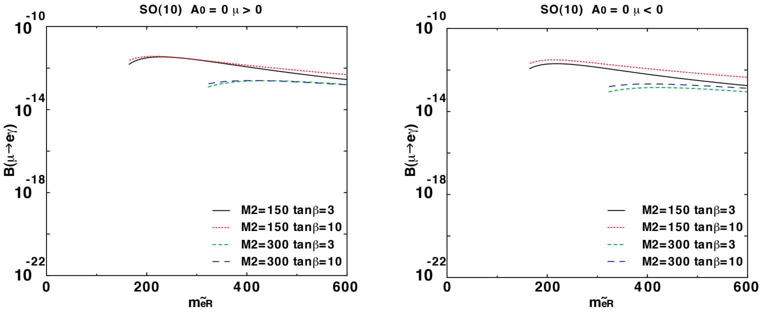

Figure 1.4: Predicted Br($\mu^+ \to \mathrm{e}^+\gamma$) in SO(10) SUSY GUT.[1]

between measurement and SM prediction[2][3][4][5].

$$\Delta a_\mu = a_\mu^{\mathrm{exp}} - a_\mu^{\mathrm{SM}} = 292(63)(58) \times 10^{-11} \tag{1.2}$$

where a_μ^{exp} is experimental value, a_μ^{SM}[6] includes contributions of QED, electroweek and NLO hadronic.

To explain the difference, new theories beyond the SM are necessary. Diagrams to explain the difference in SUSY are shown in fig.1.5, where the process is mediated by super partners of leptons and Gauge bosons.

$$a_\mu^{\mathrm{SUSY}} \simeq \pm 130 \times 10^{-11} \cdot \left(\frac{100\mathrm{GeV}}{m_{\mathrm{SUSY}}} \right)^2 \tan\beta \tag{1.3}$$

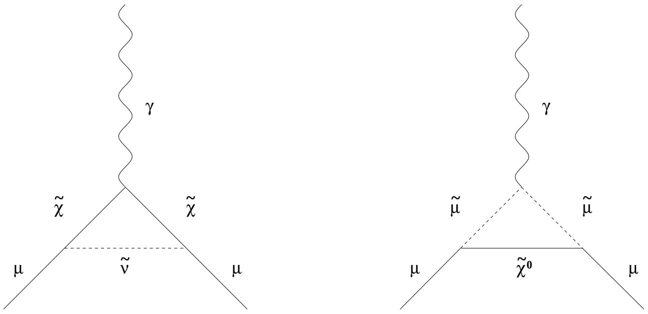

Figure 1.5: Typical SUSY contributions to g-2

$\mu^+ \to \mathrm{e}^+\gamma$ can occur with a similar diagram with adding flavor mixing of super particles, therefore a_μ^{SUSY} and Br($\mu^+ \to \mathrm{e}^+\gamma$) are correlated.

Figure 1.6 shows relation between Br($\mu^+ \to \mathrm{e}^+\gamma$) and a_μ^{SUSY} in SUSY seesaw model. Br($\mu^+ \to \mathrm{e}^+\gamma$) is predicted just bellow the current experimental bound. An experiment with 10^{-13} sensitivity can explore most of the region of the prediction.

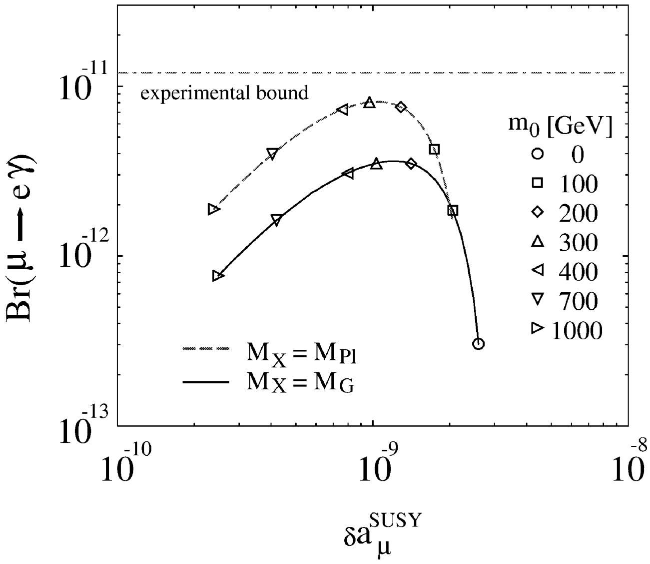

Figure 1.6: Br($\mu^+ \rightarrow e^+\gamma$) and a_μ^{SUSY}. This figure is taken from ref.[7]. Here following parameters are assumed. $V_{13} = 0.01, V_{23} = 1/\sqrt{2}, \tan\beta = 10, M_2 =$ 250 GeV. The solid and dashed lines are for cases where the scale for the generation of the SUSY-breaking terms in the SUSY SM(M_X) are the GUT scale and the reduced Planck scale, respectively.

In this section, predictions of Br($\mu^+ \rightarrow e^+\gamma$) were shown in the case of SU(5) and SO(10) SUSY-GUT. Relation between the muon anomalous magnetic moment and Br($\mu^+ \rightarrow e^+\gamma$) was shown based on SUSY see-saw model. In general, in the SUSY model, lepton flavor violation is predicted with a large branching ratio. In the SUSY-GUT, the flavor mixing in the slepton sector is naturally induced. A discovery of $\mu^+ \rightarrow e^+\gamma$ decay will be a clear evidence of a new physics beyond the standard model. Predictions by new theories are one or two orders of magnitude lower than the current experiment limit for various models and parameters. MEG would have a sensitivity of 10^{-13} when requirements summarized in table 1.3 is realized.

1.2 cLFV search

Since the first experiment to search for $\mu \to e\gamma$ was done in the 1940's, several charged lepton flavor violation (cLFV) search experiments for μ, τ and K have been performed. Upper limits of rare decays are improving, while there is not a clear evidence of cLFV yet.

Muons can be used for study of cLFV by several decay processes such as $\mu \to e\gamma$, $\mu \to 3e$ and $\mu - e$ conversion in nucleus and so on. The ratio of branching ratio of these decay processes strongly depends on models of theory, so studies of different decay process are complementary. Current upper limits of rare muon decays are summarized in table 1.1.

Experiment	Year	Decay mode	Upper limit
1999	MEGA	$\mu^+ \to e^+\gamma$	1.2×10^{-11}[8]
1988	Crystal Box	$\mu^+ \to e^+2\gamma$	7.2×10^{-11}[9]
1988	SINDRUM	$\mu^+ \to e^+e^-e^+$	1.0×10^{-12}[10]
1993	SINDRUM II	$\mu\mathrm{Ti} \to e^-\mathrm{Ti}$	4.3×10^{-12}[11]
1996	SINDRUM II	$\mu\mathrm{Pb} \to e^-\mathrm{Pb}$	4.6×10^{-11} [12]
2006	SINDRUM II	$\mu\mathrm{Au} \to e^-\mathrm{Au}$	7×10^{-13} [13]

Table 1.1: 90 % C.L. upper limits of rare muon decays.

The history of $\mu^+ \to e^+\gamma$ search experiments in this 30 years is shown in table 1.2. Improvements of the limits have been made by improvements of muon beam, i.e. number of muons, and detector resolutions to discriminate signals from backgrounds. The current upper limit of $\mathrm{Br}(\mu \to e\gamma\ )$ was given by MEGA experiment[8] in 1999. Improvements of MEG experiment with compared to MEGA is discussed in this section. The experiment was done by using high intensity surface muon beam at LAMPF. The apparatus of the experiment is shown in fig.1.7. Positrons from muon decays were measured by inner multiwire proportional chambers(MWPCs) and scintillators for timing. The photon detector consists of two 250 μm Pb conversion foils, scintillators, an MWPC and drift chambers. Energy and vertex of both particles were obtained from reconstructed tracks of charged particles in a magnetic field in the apparatus.

Year	Experiment	Upper limit
1977	-	$< 3.6 \times 10-9$[14]
1980	-	$< 1.0 \times 10-9$[15]
1982	-	$< 1.7 \times 10-10$[16]
1988	Crystal Box	$< 4.9 \times 10-11$[9]
1999	MEGA	$< 1.2 \times 10-11$[8]

Table 1.2: History of the upper limit of $\mu^+ \to e^+\gamma$ decay search experiments in this 30 years.

The single event sensitivity was $2.3 \pm 0.2 \times 10^{-12}$. A likelihood analysis was done for 3971 events in an analysis window, and the best fit was 0 signal and $30 \pm 8 \pm 15$ radiative decay events. The rests were accidental pileups.

The 90 % confidence limit was $N_{e\gamma} < 5.1$ which gives the upper limit on the branching ratio of 1.2×10^{-11}

Major improvements of MEG from MEGA are time resolution and detection efficiency of gamma ray detector, and muon stopping rate. Time resolution is better because MEG gamma ray detector contains full energy of a gamma ray, while in case of MEGA, a small fraction of energy deposits in thin scintillators were available. The detection efficiency of gamma ray in MEGA was limited by conversion probability of gamma rays in thin Pb foils. Thanks to DC muon beam, MEG will be able to accumulate more events with lower muon stopping rate which will reduce accidental pileup backgrounds.

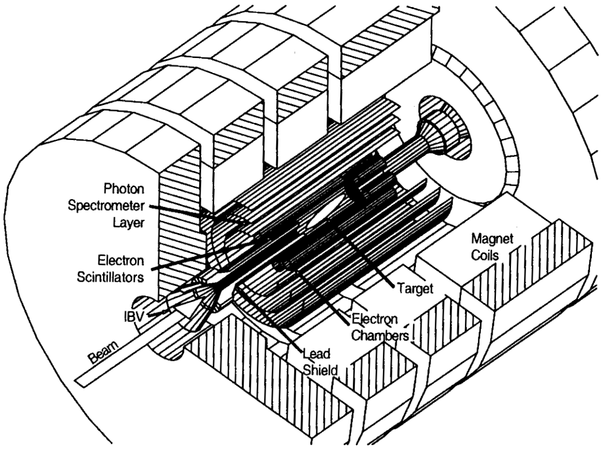

Figure 1.7: MEGA detector.

	MEGA(1999)	MEG goal
ΔE_γ [%]	4.5	4.5~5.0
ΔE_{e^+} [%]	1.2	0.8
$\Delta\theta_{\gamma e^+}$ [mrad]	15	12.4~16.9
$\Delta T_{\gamma e^+}$ [nsec]	1.6	0.18
Acceptance × Efficiency [%]	0.3	>1.6
Muon stopping rate (10^8)	2.5(Pulse, 6~7 % duty)	0.3(DC)
Running time [weeks]	20	100
Single event sensitivity(10^{-13})	23	0.5
90 % C.L. limit(10^{-13})	120	1.7

Table 1.3: Comparison of MEGA and MEG goal. Resolutions are written in FWHM. One week is 4×10^5 seconds in this table.

In chapter 2, the MEG experiment and each component is described. In chapter 3, general properties of liquid xenon to use for scintillation detectors and the liquid xenon detector for MEG are explained. After discussing about simulation of the liquid xenon detector in chapter4, performance tests by using prototype detector are described in chapter 5. In 2007, the final gamma ray detector was constructed and the first beam test was carried out. In chapter 6, the setup of 2007 beam test is described and the analysis of the gamma ray detector for the data is discussed in chapter 7. In chapter 8, 90 % confidence level upper limit of the branching ratio is estimated from 2007 physics data. Expected sensitivity with more statistics is discussed in the chapter with assumed performance in 2008.

Chapter 2

MEG experiment

The MEG experiment takes place at Paul Scherrer Institut (PSI) in Switzerland. The signature of $\mu^+ \to e^+\gamma$ is back-to-back positron and gamma ray, in time, with respective energy of 52.8 MeV. In order to reduce background events, precise measurements of energy, emission angle and time of two particles are important. The apparatus of MEG is shown in fig.2.1. Each components are described in this chapter. In this thesis, a global coordinate system shown in the figure is used, where z is direction along the muon beam, y is the vertical axis, the gamma ray detector is located at the negative side of x. The origin $(0, 0, 0)$ is the center of the target. θ is zero for positive direction of z-axis and ϕ is zero for positive direction of x-axis.

A muon stopping target is located at the center of a super conduction magnet called COBRA. Positrons from muon decays travel through drift chambers and reach timing counters. Momentum and timings of positrons are measured by these sub-detectors. Gamma rays are measured by the liquid xenon detector located outside of COBRA.

2.1 Beam and magnet

To improve the sensitivity, a large amount of muon decays are necessary. The most intense DC muon beam at PSI is used for the MEG experiment. DC beam is better than pulsed beam to correct muon data without increasing accidental pileup backgrounds so much.

PSI operates a 590 MeV proton cyclotron with the maximum current of 2 mA. The power of the beam is 1.2 MW. A production target is put on the primary proton beam line, and produced pions and muons are extracted to the πE5 area where the MEG experiment takes place. A surface muon beam, which is used for the experiment, is produced from pion decays on the surface of the production target. The surface muon beam has high intensity and low range straggling which allow to use a thin muon stopping target, hence multiple scattering of positrons can be reduced. Figure 2.3 shows a schematic view of the MEG beam line layout. Muons are transported from the production target to the stopping target through Triplet I(quadrupole triplet), a Wien filter, Triplet II(quadrupole triplet) and a beam transport solenoid(BTS). A Wien filter separates electrons from muons by 8.1 σ with using crossing magnetic field

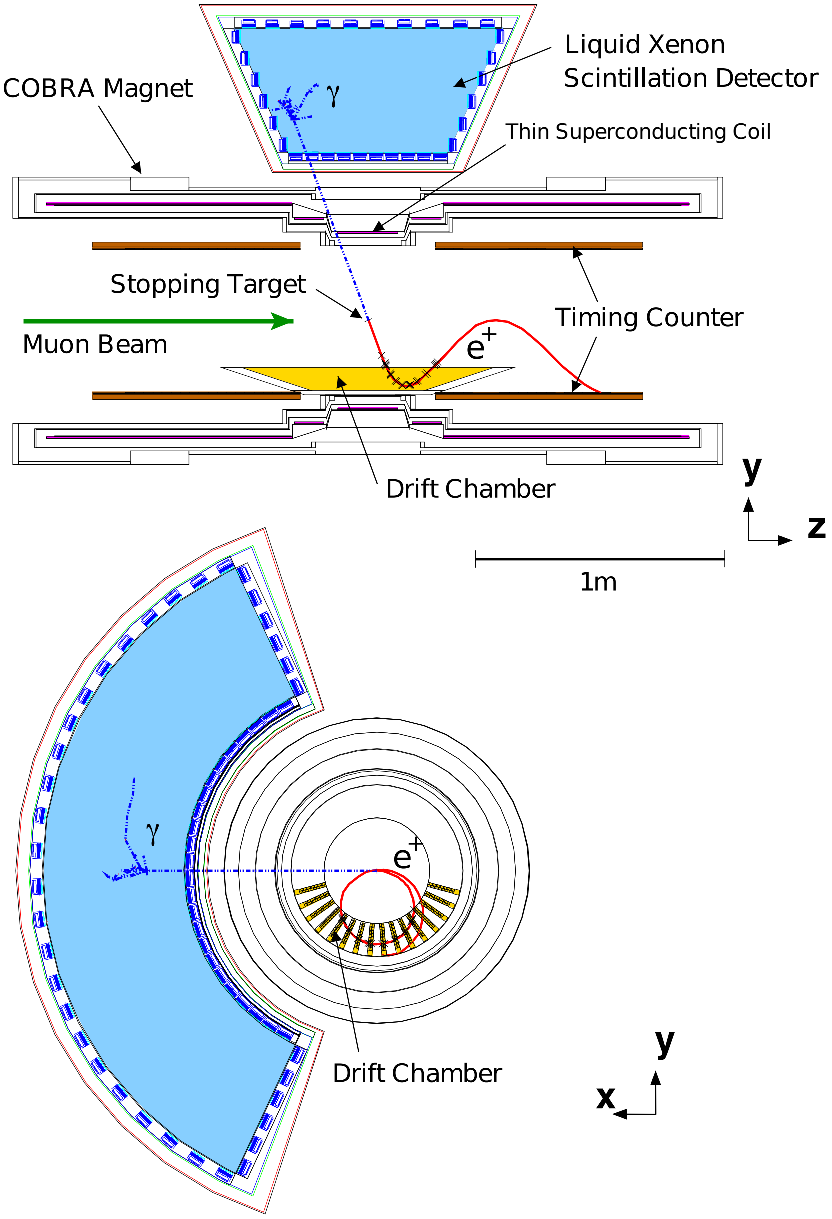

Figure 2.1: MEG apparatus.

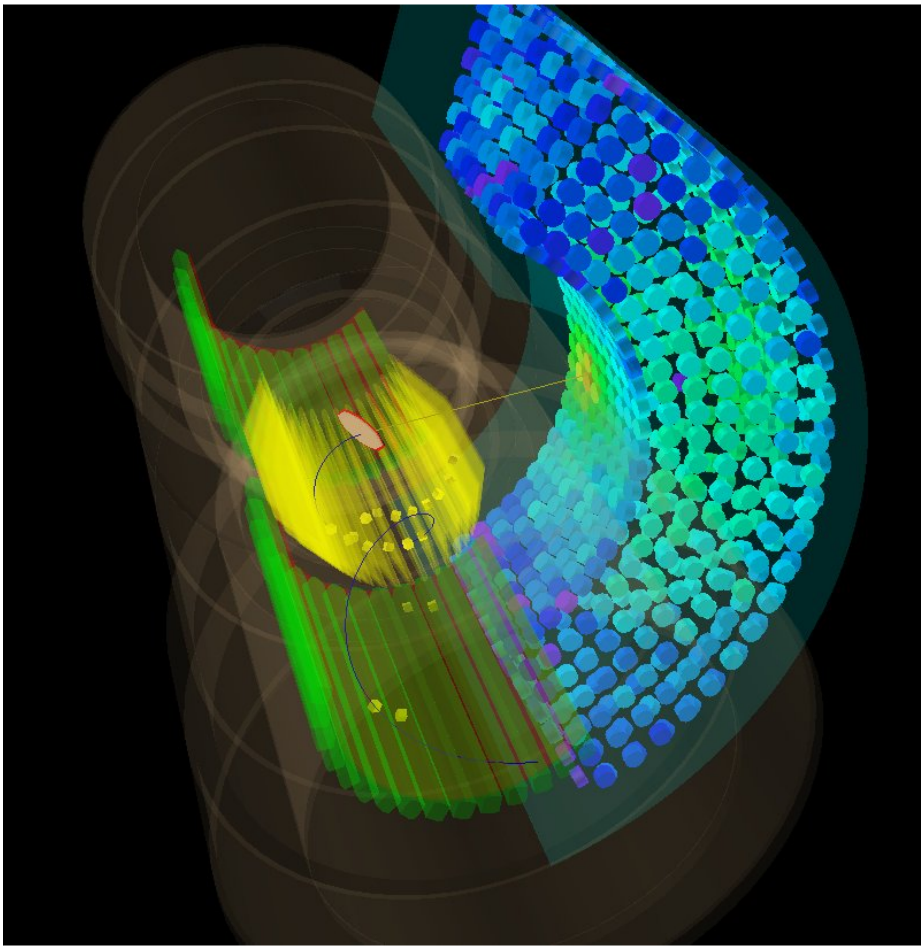

Figure 2.2: An event display during MEG physics run. Reconstructed hits and tracks are shown. Color of PMTs in the display represent its output. In this event, two positrons are observed in time window.

(133 G) and electric field (195 kV). The BTS is used to adjust the oscillation of the beam profile to minimize the beam spot size on the stopping target. A momentum degrader is installed in the BTS to adjust the momentum of muons so that they stop on the thin target. Muon momentum is degraded by Mylar degrader(300 μm), Mylar vacuum window(190 μm) and helium gas in the COBRA magnet (1475 mm). In run 2007, a few percents of air was added artificially for stable operation of the drift chambers to suppress discharges. Effect of the air admixture of 5 % is about 5 % loss of transmission. Different settings of magnets for "high", "normal" and "ultra low" modes for different muon intensities were prepared. In the case of 2007 run, expected muon stopping rates in 100 % helium were 8.6×10^7, 3.2×10^7 and 6.1×10^6 when the proton current is 2 mA. Nominal beam intensity to start physics data accumulation in 2008 is the "normal". The ultra low intensity beam is used for studies and calibrations of the detector and collection of radiative decay events in a cleaner environment where there are less pileups. Measured beam spot sizes(σ_x, σ_y) at the center of the COBRA were $(11.0, 12.7)$ mm and $(9.5, 10.2)$ mm for high and normal intensity beam respectively.

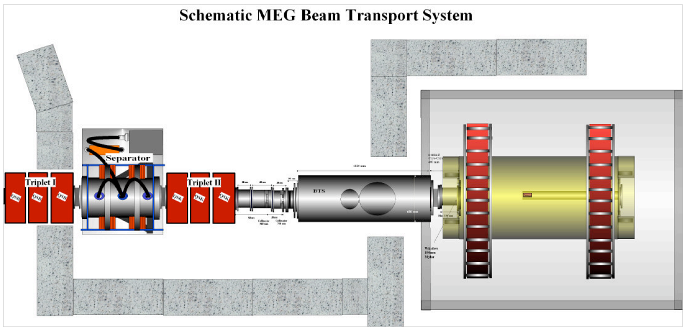

Figure 2.3: Schematic of the MEG beam line layout. A muon beam is injected from the left of this figure.

2.2 Target

Pictures of the muon target are shown in fig.2.4. The target is a polyethylene/polyester sandwich foil supported by a Rohacell frame. The density is 0.895 g/cm^3 The design was optimized for balancing muon leakage and probability of scattering or annihilation in flight of positrons. The shape of the target is ellipse with diameters along minor and major axises of 79.8 and 200.5 mm respectively. The thickness of the target is 205 μm. Since the acceptance of the MEG detector is around $\theta = 90°$, the smaller slant angle is favored to decrease multiple scattering, while the larger slant angle is favored to decrease muon leakage. A simulation work was done to optimize the slant angle by using measured beam profile and straggling. In 2007, slant angle was 12.5° which caused 12.6 % of leakage. In 2008, the angle was modified to be 20.5°. Several holes of 10 mm diameter are made on the target to study the vertex reconstruction resolution.

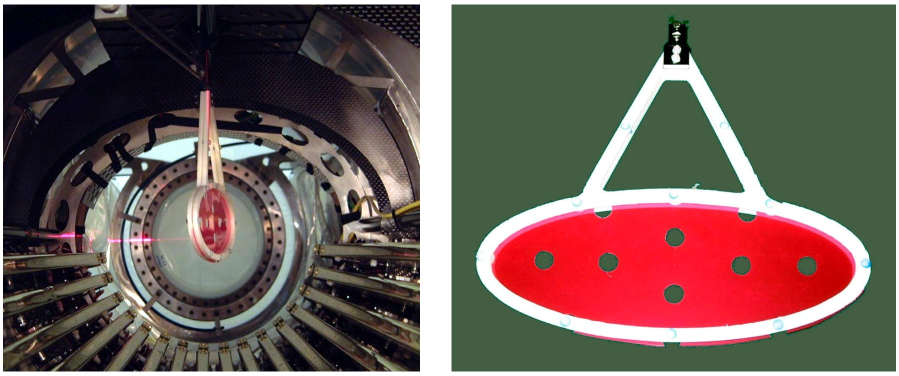
(a) (b)

Figure 2.4: (a) A muon target installed in the spectrometer (b) A picture of the target.

2.3 Detector

Sub-detectors to measure positrons are installed in a super conducting solenoid magnet called COBRA (Constant projected Bending Radius). 16 drift chamber modules are put at the center of z in the COBRA. Positrons emitted on the target travel through the chambers, and they reach to timing counters located at upstream and downstream of the drift chambers.

A liquid xenon detector is used to measure kinematics (energy, time and position) of gamma rays at the first conversion point in the detector. Since, the detector does not have good capability to determine direction of gamma rays, opening angle of a gamma ray and a positron is calculated with assuming the gamma ray was emitted at the decay vertex determined by the spectrometer. Details of the liquid xenon detector are discussed at section 3.2. The gamma ray detector is located in one side viewed from the target, and the geometrical acceptance is about 10 %. Positron detectors are located at corresponding position to measure back-to-back positrons. Sub-detectors are located to observe particles in an acceptance defined to be $|\phi| < 60^\circ$ and $0.08 < \cos\theta < 0.35$.

2.3.1 Positron spectrometer

COBRA

As shown in fig.2.5, the COBRA magnet system consists of a main super-conducting magnet and two normal-conducting compensation coils. The compensation coils were prepared to decrease magnetic field around the gamma detector so that PMTs work. Super-conductor material is NbTi multi-filament embedded in copper matrix and aluminum-stabilizer. Nominal current of the super-conducting magnet is 360 A, and the peak value of the magnetic field is 1.7 T in the central coil. The super-conducting magnet was designed to have smaller radius in the central part and larger radius in large z part to form a gradient magnetic field along z direction. As shown in fig.2.6, radius of positron trajectory in cylindrical coordinates is almost independent of emission angle, and it is approximately determined by energy of the positron. Therefore, it is easier to choose energy range to measure by designing the position of drift chambers so that they cover proper range of radius. This allows to avoid measuring low energy positrons which come with very high intensity (thus it can saturate the drift chamber system). If we use constant magnetic field, positrons emitted almost perpendicular to the beam axis can hit drift chambers many times as shown in fig.2.6-a. On the other hand, in case of the COBRA field, such positrons are swept out quickly.

COBRA was designed to be very thin to minimize interactions of gamma rays in it before reaching the gamma ray detector. The thickness of components used in the coil and the cryostat of the magnet within the acceptance of the gamma ray detector corresponds to 0.197 radiation length.

Relative output of the PMT used in the gamma ray detector as a function of magnetic field is shown in fig.2.7. The tolerance to the magnetic field depends on the direction due to the structure of the PMT. For the most sensitive direction, the maximum allowed field strength is 50 G where output of PMT becomes half compared with zero-field. Figure 2.8 shows the profile of the magnetic field along the boundary of the gamma ray detector. PMT response was measured in the

COBRA field, at 31 points in a region corresponding to the active volume of the gamma ray detector and 1 point where magnetic field is higher. The maximum reduction of the PMT output was 40 % in the active volume. However, output reduction was negligible at almost all PMTs located in the inner face where large fraction of scintillation photons will be observed. Figure 2.9 shows the result of the measurement for PMTs placed along the magnetic field, 4.23 meters away from the axis. The magnetic field at the position is 61.7 G, and this value is higher than that in the gamma ray detector.

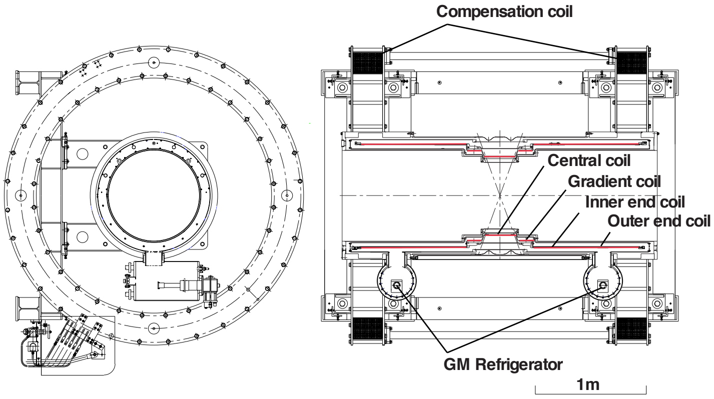

Figure 2.5: The COBRA magnet.

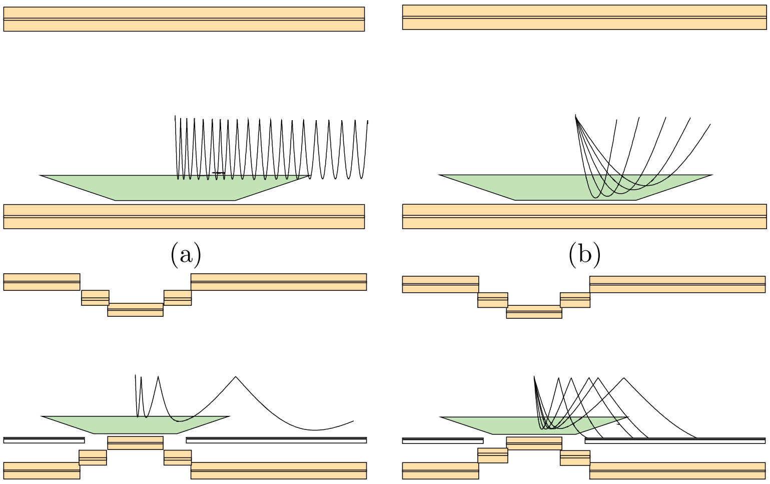
(a)
(b)
(c)
(d)

Figure 2.6: Conceptual picture of positron tracks in the COBRA magnetic field.

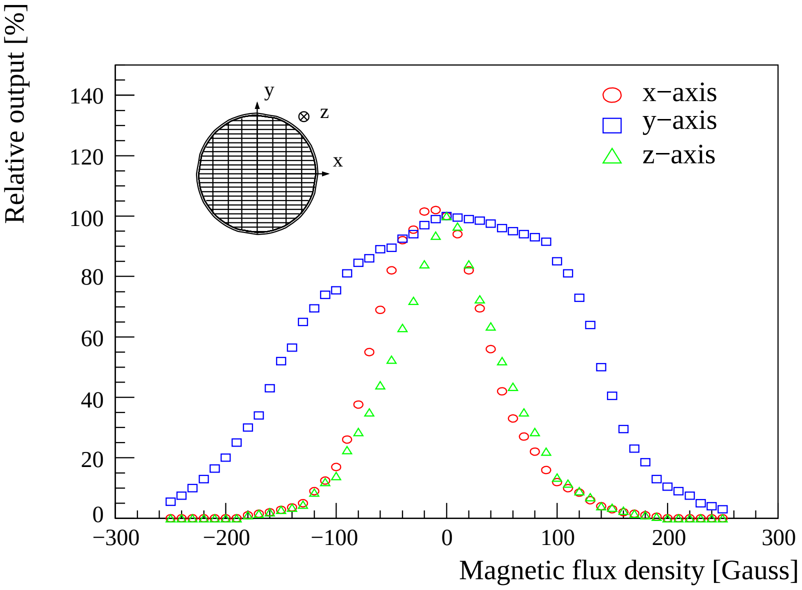

Figure 2.7: PMT response(R6041Q) and magnetic field. Measurement was done by Hamamatsu photonics

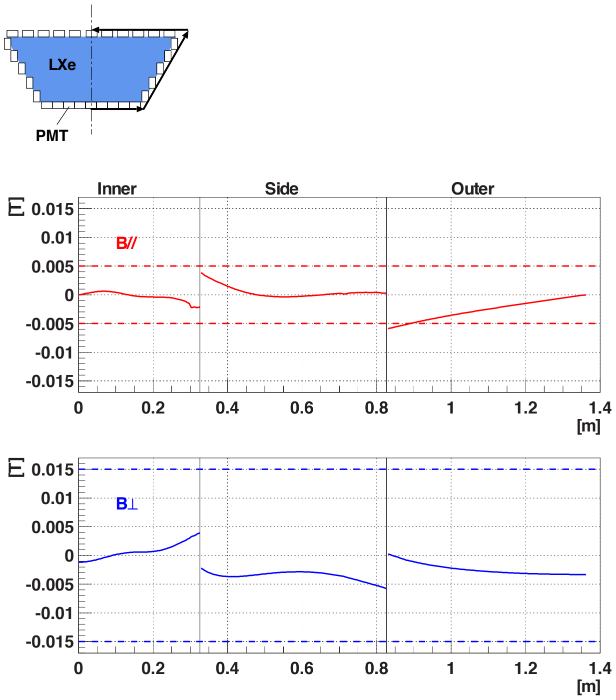

Figure 2.8: The COBRA magnetic field.

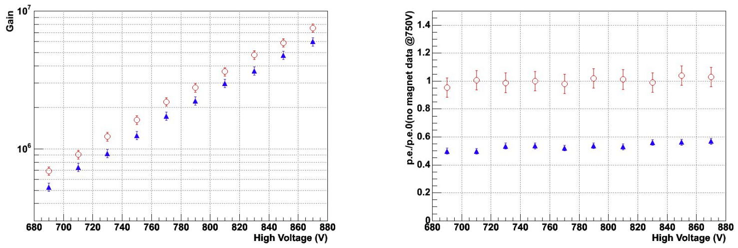

(a) (b)

Figure 2.9: PMT response(R9288) and magnetic field. (a) Gain curves under the magnetic field of 61.7 G (triangle) and in zero magnetic field (circle). (b) Ratio of the effective quantum efficiency to that in zero magnetic field as a function of applied voltage.

Drift chambers

Tracks of positrons are measured mainly by drift chambers located inside the COBRA. Requirements of drift chambers are follows.

- It must be light to reduce probability of scattering of positrons for better detection efficiency and resolutions. It is also needed to reduce the probability of positron annihilation in flight (AIF) which can make accidental backgrounds.
- It must work under a condition with very high rate muon decays on the target.
- It must have good hit position measurement capability and detection efficiency to reconstruct tracks with high precision, without increasing number of readout channels.

Figure 2.10 shows a picture of a chamber module before the final assembly. The main structure of a drift chamber is supported by a thin carbon-fiber frame. One edge of the frame in the direction to the target is open, in order to reduce materials in a region where many positrons transverse. The shape of the frame is designed by taking into account a deformation due to the tension of wires. Cathodes of the chambers are made of 12.5 μm thick polyimide with aluminum deposition. The shape of the chamber walls is maintained by pressure control of chamber gas and helium outside of the chambers. The pressure difference is controlled with a precision better than 0.005 Pa by a feed back control system. Figure 2.11 shows the distribution of radius of positron tracks. Since the drift chamber is designed to find $\mu^+ \rightarrow e^+\gamma$ signal, positrons with a small radius is not interesting, while such positrons can saturate the drift chamber system with a high rate. The fiducial region of the drift chambers fully covers positrons with larger momentum than 40 MeV.

The drift chamber is filled with a gas mixture of 50 % helium and 50 % of ethane.

z coordinate of a hit is roughly estimated from the charge ratio of two ends of a wire with resolutions from 6.58 mm to 11.50 mm depending on wire length. A precise estimation is done by using a so-called vernier pattern on the cathode foil[17][18][19][20] as shown in fig.2.12. The cathode of a drift cell consists of four strips with a special pattern. The pattern has an interval of 5 cm which is large enough than the z measurement precision from the charge ratio. Phases of the pattern are shifted by 1/4 interval for each strip so that a precise z position can be measured from the ratio of charges of four strips. Averaged resolution of z reconstruction is 612 μm.

r position of a hit can be roughly determined from a hit time, and it is estimated with a better precision by connecting several hits and finding a track where angle dependence of drift time to distance relation can be taken into account. The resolution is from 170 μm to 351 μm depending on drift distance.

A momentum resolution of 0.9 % and angular resolution of 6 mrad in σ for 52.8 MeV/c positron have been achieved in the MEG engineering run in 2007.

Construction and performance in 2007 are described in a thesis[21].

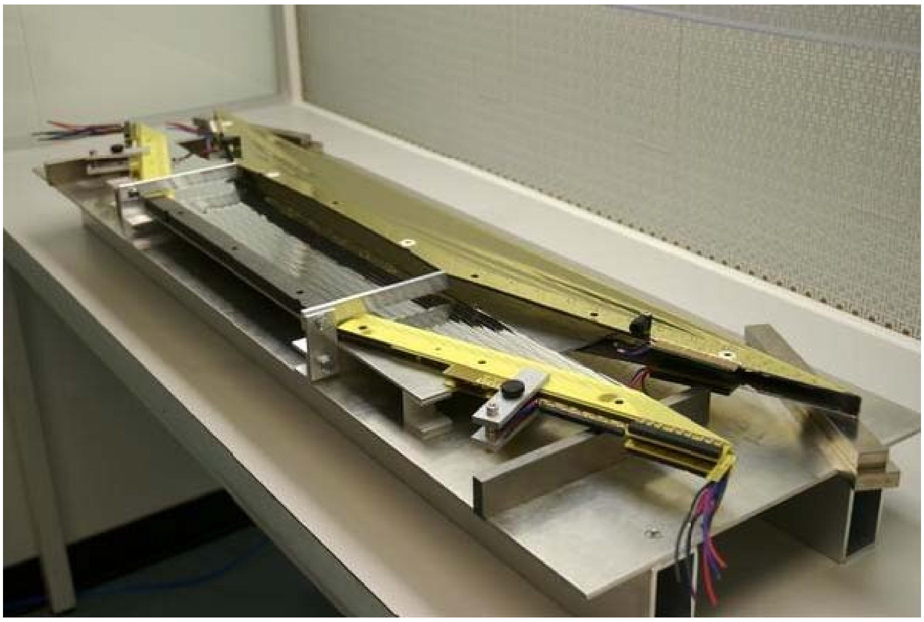

Figure 2.10: A picture of a chamber module before the final assembly.

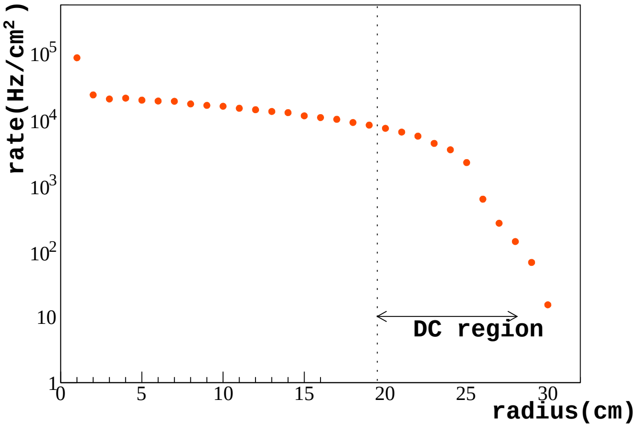

Figure 2.11: Positron rate as a function of radius with assuming muon rate of 3×10^7 / sec.

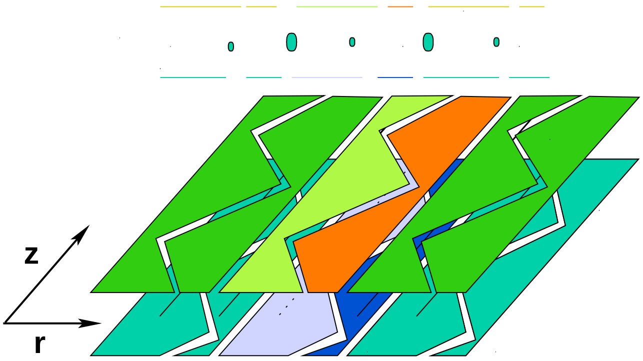

Figure 2.12: Vernier pattern on cathode foils.

Timing counters

The timing counter system consists of 30 ϕ-measuring counters and 512 z-measuring counters.

ϕ counters are straight plastic scintillator bars made of BC404 lying along z direction as shown fig.2.13. Two inch fine-mesh PMTs(R5924) are attached both ends. 15 bars are located in upstream and downstream from the target. Signal positrons in the angular range of $0.08 < |\cos\theta| < 0.35$ hit the counters.

In MEG 2007 run, the time resolution was measured to be 52.0 psec from distribution of time difference between adjacent bars. The resolution of muon decay time was estimated from MC simulation with taking into account the measured time resolution of single bars. Obtained time resolution is 58.7 psec. The difference between the muon decay time resolution and the single bar resolution is uncertainty of track-length reconstruction[21].

A z counter is a curved scintillation fiber put perpendicular to ϕ counters as shown in fig.2.14. The purpose of z counters is to determine the z position of hits with a good resolution, and the counters do not measure hit time. The measured position is used to estimate the time of muon decay with subtracting estimated time of flight from the hit times in ϕ counters.

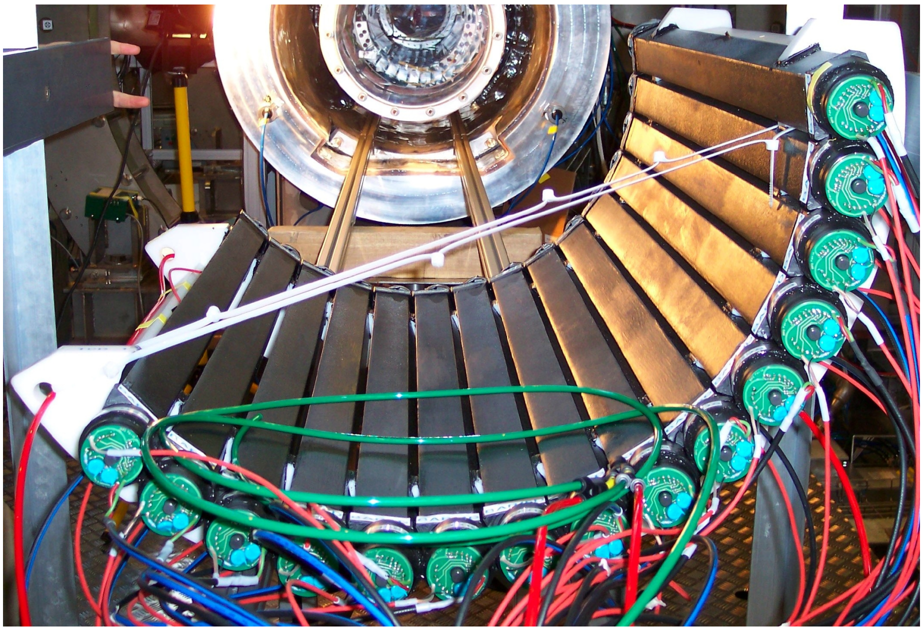

Figure 2.13: A picture of timing counters (ϕ-measuring counters).

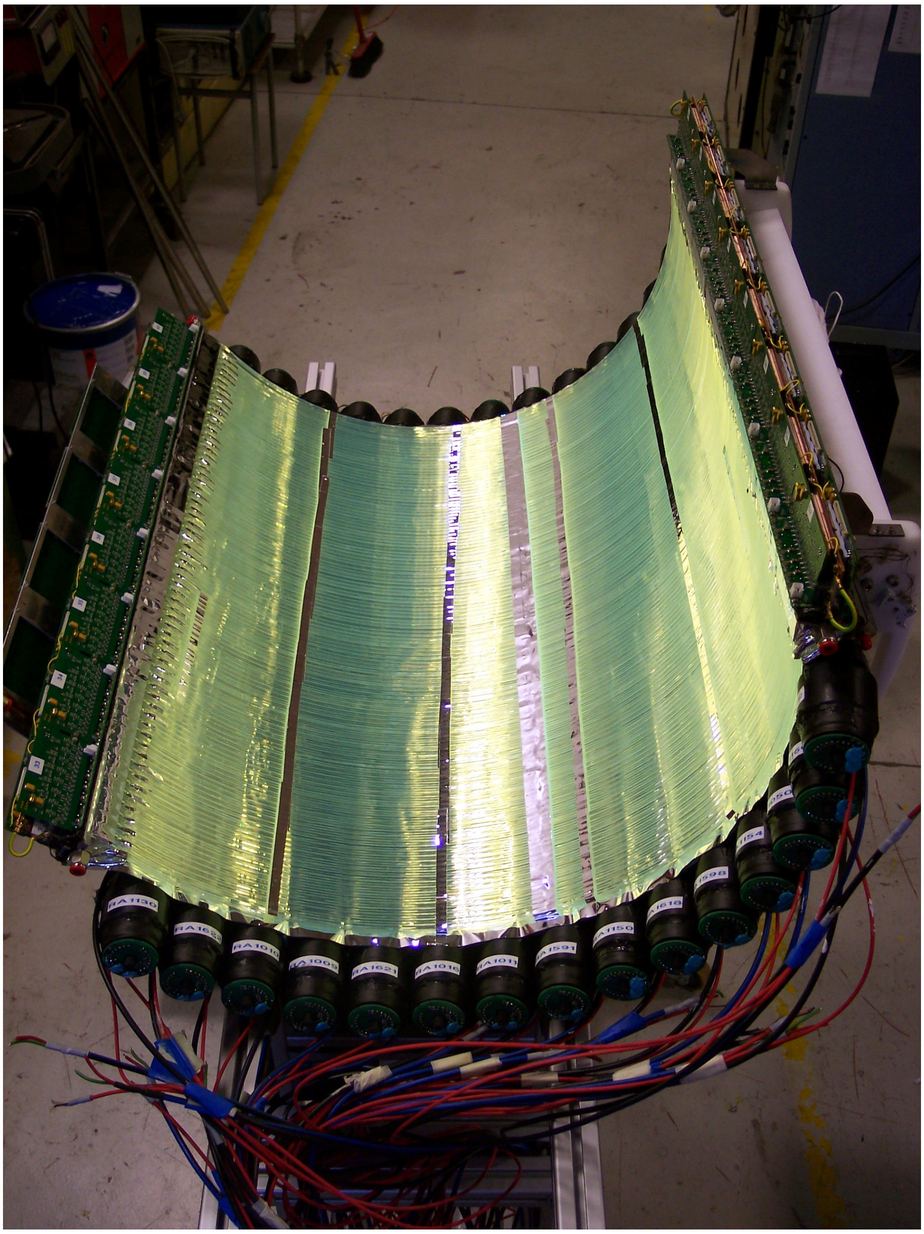

Figure 2.14: A picture of timing counters (z-measuring counters). 256 curved scintillators are put on ϕ-measuring counters in this picture. Readout cards attached to z counters can be seen in the picture.

2.4 Electronics and DAQ

Waveforms of the gamma ray detector and the positron timing counters are sent to active splitters through coaxial cables. Each splitter board has 16 input channels and three types of outputs. For the first type of outputs, high bandwidth(1900 MHz) amplifiers (THS4509) are equipped. These outputs are sent to the primary readout boards named DRS(Domino Ring Sampler). The second and third type of outputs are used for trigger. For the second output, low distortion amplifiers(AD8138) with lower bandwidth(320 MHz) are equipped. The third output is an analog sum waveform of each four input channel. Anode signals of the drift chamber are split by resistive splitter into two groups in the proportion of one to nine. The larger one is sent to DRS, and the smaller one is sent to trigger system after amplified to recover pulse height and summed up according to trigger logic.

Trigger system is equipped with 100 MHz FADC to digitize waveforms and FPGA implemented on VME boards. The system has a tree structure shown in fig.2.15. Analog waveforms are digitized by type 1 boards and serialized data is sent to type 2 boards to determine triggers of sub-systems. Finally data from sub-systems is sent to a type 2 board in the third layer to make trigger decision. When a trigger condition occurs, a stop signal is sent to DRS system. In addition to type 1 and 2, type 3 which is a modified version of type 1 to record waveforms of all individual channels of the gamma ray detector. Data taken by type 3 boards is not used for trigger decision, but it is used in offline analysis. Triggering algorithms were prepared for various kinds of event types such as $\mu^+ \rightarrow e^+\gamma$ (MEG), radiative muon decay(RD), self trigger of each subsystem, random trigger and so on. Several algorithms can be used simultaneously with each pre-scaling factor. The system has scalers of each trigger type. Live time of the system is measured by the system itself.

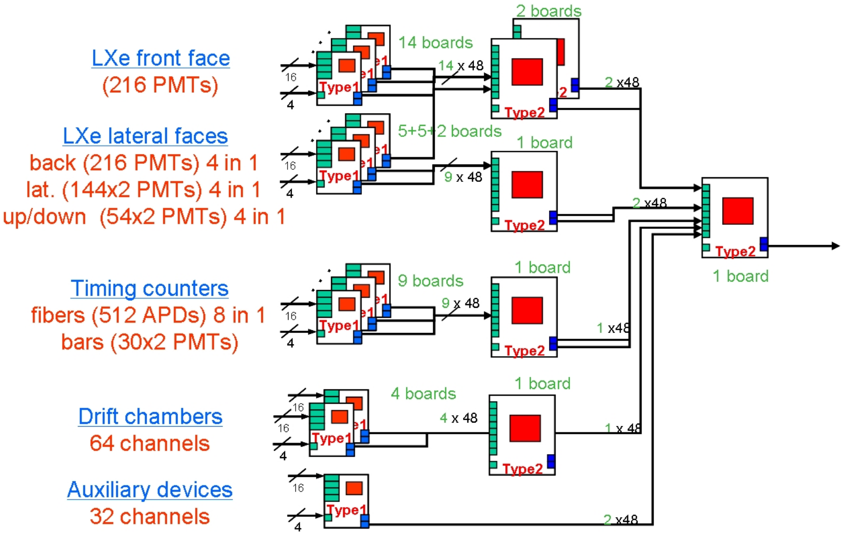

Figure 2.15: MEG trigger tree structure

All the waveforms from PMTs of the gamma ray detector, PMTs of timing counters, wires and cathodes of drift chambers are digitized by DRS[22]. All the waveforms are recorded as raw data. Charge and time of waveforms are extracted in offline analysis, so no ADC or TDC modules are used in the DAQ. The main purpose of recording waveforms is to allow to do pileup identification in offline analysis, because it is a major source of background events in physics analysis. It also allows to use better waveform analysis after improving it. For example, we can try different noise reduction algorithms, time extraction methods by using template fitting or constant fraction.

DRS is a switched capacitor array developed in MEG experiment to digitize fast signal. A simplified schematic is shown in fig.2.16. The second version (DRS2) was used in MEG run 2007. Two DRS2 chips are mounted on a board, and two boards are mounted in a VME module. Each chip has 10 channels, with 1024 capacitive sampling cells. Two channels out of 10 are used for calibration purpose. So actual number of channels per chip is 8. In total, 32 channels per VME module can be read. In MEG experiment, 94 VME modules of DRS in 5 crates are used. Sampling rate of DRS2 is adjustable from 0.5 to 4.5 GHz. The cells are read by an external 12 bit FADC. In 2007, 0.5 GHz was used for the drift chambers and 1.6 GHz was used for the gamma ray detector and the timing counters. The ninth channel is used to record trigger stop signal to allow to know cell number corresponding to the trigger. The last channel is used to read a common clock signal which is distributed to all the DRS boards to align phase of measurement. Analysis of time calibration by using this information is described in section 7.3.1. Measured waveforms of the gamma ray detector by DRS with 1.6 GHz sampling rate are shown in fig.4.2-a,b,c.

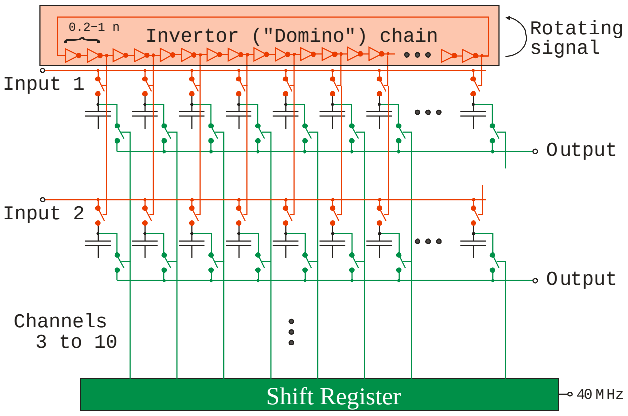

Figure 2.16: Simplified schematic of the DRS2 chip

2.4.1 Data reduction

Because waveforms of each channels of sub-detectors are recorded, raw data event size of the MEG experiment is large. If no data reduction or compression is used, the maximum data size is more than 5 MB/event. Event rate of $\mu^+ \to e^+\gamma$ trigger with the highest beam intensity is expected to be around 20 Hz. Such a large event size could cause many problems, for example I/O of disk, data transfer over network, process speed of data compression in offline system and the amount of storage. The bottle neck of the data flow can be I/O speed of tape system, which is 20 to 30 MB/sec.

Data reduction in 2007 run was done in two steps. The one was done during data acquisition, and the other was ZIP compression of data files in offline system. In the second step, data is compressed by about 50 %. For the first step of data reduction, several kinds of algorithms were implemented for each sub-detector. For the drift chambers and timing counters, region of interest(ROI) and so called zero-suppression work. In case of these sub-detectors, pulse width is relatively short compared to full time window of readout, hence it is possible to choose narrower time window for recording without degrading resolutions or efficiency. Number of channels which have hits is small in each event. So, only channels which have a large enough pulse and related ones (i.e. channels in the same cell of a drift chamber and those in adjacent cells) were recorded.

In the case of the gamma ray detector, about 40 % of channels have hits in each event, and time window of readout is not very large compared to scintillation decay time. Therefore ROI or zero-suppression does not decrease data size so much. Instead of that, rebinning of waveforms was used. To measure time of gamma rays precisely, waveforms of the gamma ray detector are sampled in 1.6∼2.0 GHz. However, such a frequent sampling is required only around the peak of waveforms. To reduce the data size, waveforms of gamma rays were rebinned with wider bin width except around the peak. When changing binning, the new entry is redefined to be an average of original adjacent bins to conserve integrated charge. In run 2007, rebinning size was eight. Namely, data size was reduced to about 1/8.

By all of these compressions, single event size was 1.15 MB/event in 2007.

2.5 Proton accelerator

For calibration of the sub-detectors by using gamma rays from nuclear reactions, a 1 MeV Cockcroft-Walton(C.W.) proton accelerator was prepared. Figure 2.17 shows a photograph of the accelerator. The main purpose of the accelerator is to generate 17.6 MeV line from Li(p,γ)Be which is resonant at E_p = 440 keV with a resonance width of about 15 keV. This energy is 1/3 of $\mu^+ \rightarrow e^+\gamma$ signal, however high rate monochromatic gamma rays allow to calibrate and monitor the performance of the gamma ray detector. In addition to that, two coincident gamma rays with lower energies(4.4 and 11.7 MeV) can be generated with B(p,γ)C reaction. Properties of the accelerator are summarized in table 2.1.

A C.W. accelerator area was prepared at the downstream side of the muon beam line. Protons are transferred through a beam line prepared on the same axis with the muon beam line, from the accelerator to a target. A part of the beam line is made of bellows to allow inserting it into the COBRA volume toward the target. It is possible to switch from the normal muon measurement mode to the calibration mode by moving the muon target to a parking position and inserting another target and beam line for calibration quickly in around 20 minutes. Therefore, daily calibration by using the C.W. accelerator is possible. For actual operation, a LiF crystal is used for lithium reaction. Fluorine has

Figure 2.17: C.W. accelerator seen from the front. RF coil is on the left.

	Nominal	Measured at PSI
Terminal energy range	300~900 keV	200~1100 keV
Energy ripple	$< 500\ \mathrm{V_{rms}}$	$< 50\ \mathrm{V_{rms}}$
Angular divergence	$< (5\times5)\ \mathrm{mrad}^2$	$\sim(4\times4)\ \mathrm{mrad}^2$
Spot size at 3 m	$< (3\times3)\ \mathrm{cm}^2$	$< 1\ \mathrm{cm}^2$
Energy setting reproducibility	0.1 %	OK
Energy stability FWHM	0.1 %	OK
Range of current	$1\sim100\ \mu\mathrm{A}$	$0.1\sim135\ \mu\mathrm{A}$
Current stability	3 %	OK
Current reproducibility	10 %	OK
Start-up time	< 20 min	< 15 min

Table 2.1: Properties of MEG C.W. accelerator

another gamma line of 6.13 MeV. The 17.6 MeV gamma ray generation rate is 1.8 kHz/μA. For boron reaction, a metallic boron piece is used as the target. Figure 2.18 and 2.19 shows spectrum of gamma rays from these reactions.

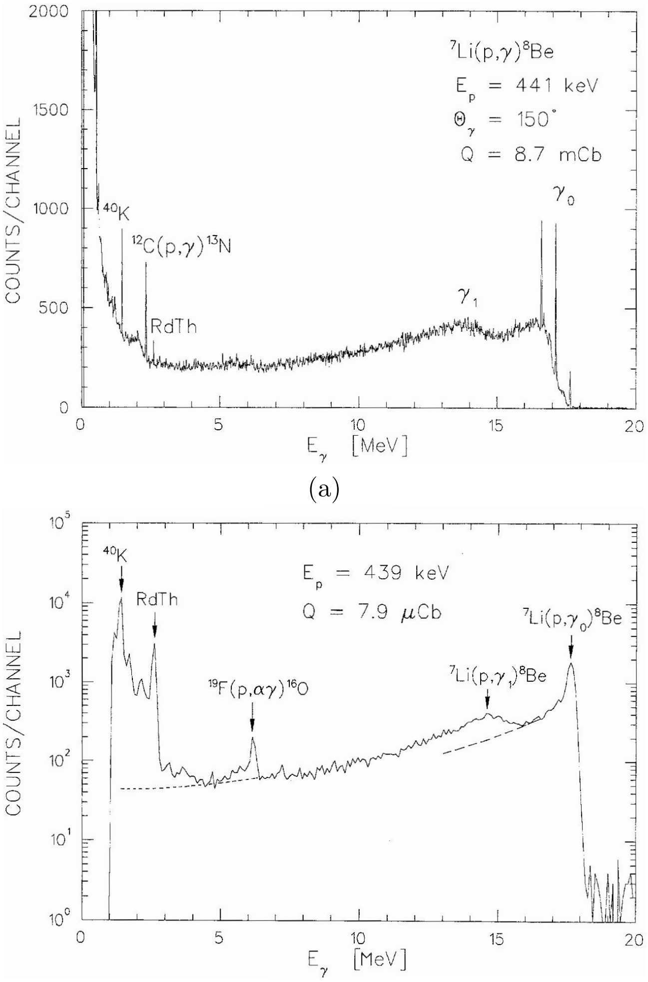

(a)

(b)

Figure 2.18: Gamma ray spectrum from lithium measured with (a)Ge(Li) detector and (b)NaI(Tl) detector.[23]

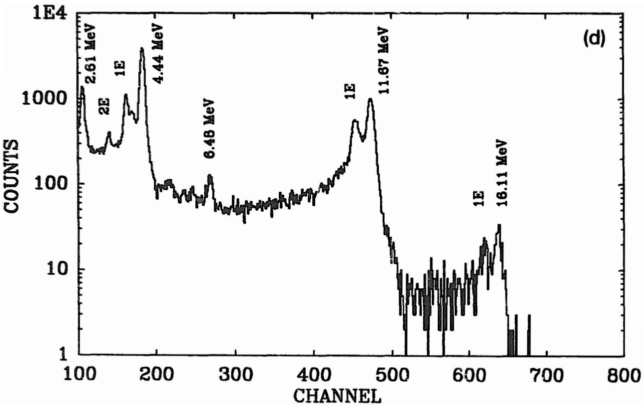

Figure 2.19: Gamma ray spectrum from boron measured with NaI(Tl) detector.[24]

2.6 Signal and backgrounds

Backgrounds of $\mu^+ \to e^+\gamma$ measurement are a radiative muon decay with a high energy gamma ray and a positron (prompt background), and an accidental coincidence of a Michel positron and a particle hit the gamma ray detector (accidental background). Sources of gamma ray detector hits are those from radiative muon decays, those from positron annihilation in flight, low energy cosmic rays or secondaries of them and pile up of these hits. Kinematics of signal, prompt background and accidental background are shown in fig.2.20.

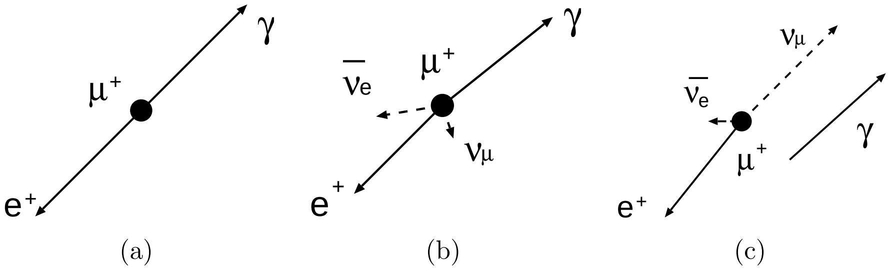

(a) (b) (c)

Figure 2.20: Signal and backgrounds of $\mu^+ \to e^+\gamma$.

Chapter 3

Liquid xenon scintillation detector

Xenon is used for various applications such as dark matter search, neutrinoless double beta decay search, medical applications(PET) and gamma ray astronomy because of its excellent characteristics as ionization or scintillation medium, such as a high light yield, fast decay time. It is also popular to use combination of ionization and scintillation. Details of the scintillation mechanism are described in ref.[25]. In this chapter, general aspects about liquid xenon as a scintillation medium are shown, then structure and construction of the gamma ray detector for MEG experiment are described.

3.1 Liquid xenon

Figure 3.2 shows a comparison of properties of crystal scintillators and those of liquid xenon. As shown in the table, light output of liquid xenon is large and decay time constant is fast. These properties make it possible to make a detector with good energy and time resolutions. Fast decay is suitable for high rate experiment like MEG to identify pileup events by waveform analysis. Large atomic number and high density comparable with crystal scintillators allow to make a rather compact detector, hence a detector can have a good reconstruction capability of interaction positions. Because it is liquid, it is possible to make a large detector with a uniform response. Liquid xenon is not damaged by radioactivity.

Interaction of particles with xenon atoms can form both Xe^+ (ion) and Xe^* (excited) state. Excited atoms lead to the formation of excited dimers(Xe_2^*) which emit scintillation photons in de-excitation process. Two excited states, single and triplet, have different decay time constants of 4 and 22 nano seconds respectively. Ionized atoms emit scintillation photons through a process described from equation.3.2 to equation.3.7. Decay time of recombination differs depending on ionizing particles. In the case of alpha particles or fission fragments, it is less than 1 nano seconds, on the other hand for electrons and gamma rays, it is 45 nano seconds. Fractions of three processes depends on ionizing particle and electric fields. Decay time constants of three processes

Table 3.1: Properties of xenon

Atomic Number	54
Mass Number	131.29
Density at 161.4 K	2.978 g/cm^3 [26]
Boiling point	165.05 K
Melting point	161.25 K
Emission peak	178 nm [27] [28]
Spectrum width	14 nm [27] [28]
Refractive index	1.57 to 1.72 [29] [30] [31]
W$_{ph}$ for 1 MeV electrons	21.6 eV [32]
Decay time(recombination)	45 nsec [25]
Decay time(fast components)	4.2 nsec [25]
Decay time(slow components)	22 nsec [25]
Absorption length	$>$ 100 cm
Scattering length	29 cm to 50 cm [31][33][34][35]

Table 3.2: Comparison of physical properties of crystal scintillators with those of liquid xenon

	NaI	BGO	GSO	LSO	Liq. Xe
Effective atomic number	50	73	58	65	54
Density (g/cm^3)	3.7	7.1	6.7	7.4	3.0
Relative light output (%)	100	15	20-40	45-70	80
Decay time (nsec)	230	300	60	40	2.2,27,45

without electric fields are shown in table 3.3. Figure 3.1 shows scintillation signals of liquid xenon by various particles. Two decay time components are clearly seen in signals by alpha particles and fission fragments, while it seems that the signals by electrons have one slow component by recombination. The recombination component must disappear when an electric field is applied. Scintillation signals with and without electric fields are shown in fig.3.2. When an electric field is applied, the usual two components can be seen. Actual ratio of ionization and recombination can be estimated from the ratio of scintillation and ionization signals with various electric fields. According to ref.[32], it is considered from 0.06 to 0.20.

$$\mathrm{Xe} + \mathrm{Xe}^* \rightarrow \mathrm{Xe}_2^* \rightarrow 2\mathrm{Xe} + h\nu \tag{3.1}$$

$$\begin{aligned}
\mathrm{Xe} &\rightarrow \mathrm{Xe}^+ + e && (3.2)\\
\mathrm{Xe}^+ + \mathrm{Xe} + \mathrm{Xe} &\rightarrow \mathrm{Xe}_2^+ + \mathrm{Xe} && (3.3)\\
\mathrm{Xe}_2^+ + e &\rightarrow \mathrm{Xe}^{**} + \mathrm{Xe} && (3.4)\\
\mathrm{Xe}^{**} &\rightarrow \mathrm{Xe}^* + \mathrm{heat} && (3.5)\\
\mathrm{Xe}^* + \mathrm{Xe} + \mathrm{Xe} &\rightarrow \mathrm{Xe}_2^* + \mathrm{Xe} && (3.6)\\
\mathrm{Xe}_2^* &\rightarrow 2\mathrm{Xe} + h\nu && (3.7)
\end{aligned}$$

Radiation	τ_s	τ_t	τ_r
Electrons	-	-	~ 45
Alpha particles	4.3 ± 0.6	22 ± 1.5	-

Table 3.3: Decay time of liquid xenon

Figure 3.3 shows attenuation coefficients of gamma rays in xenon. It is minimum around 4 MeV. Around 50 MeV, pair production dominates. Mean free path in liquid xenon is 3.46, 9.37 and 5.48 cm for 0.5, 4.0 and 50 MeV respectively.

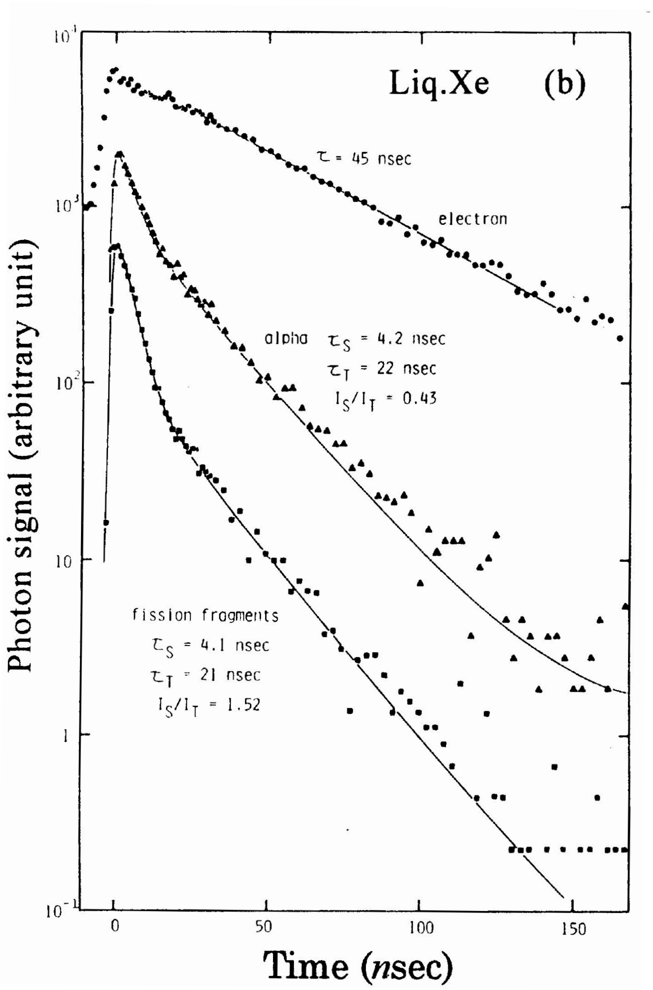

Figure 3.1: Signal of liquid xenon scintillation.[36]

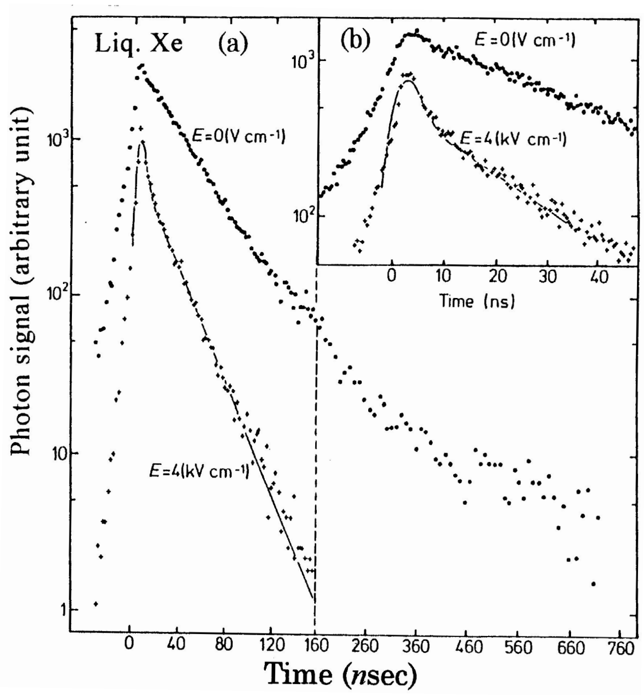

Figure 3.2: Signal of liquid xenon scintillation and electric field.[36]

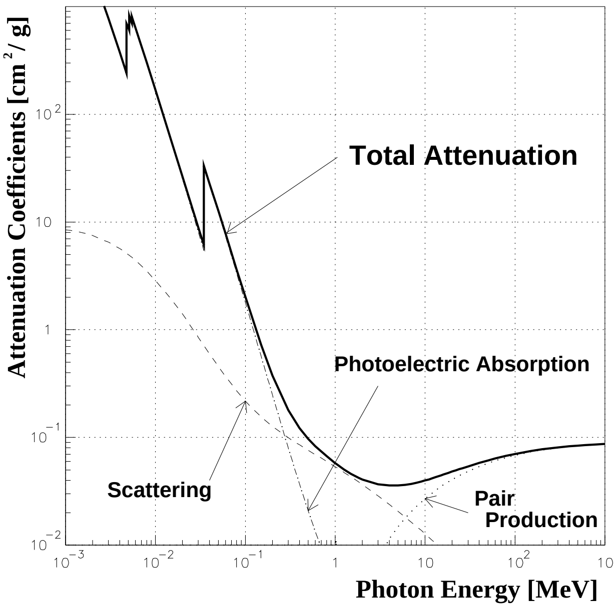

Figure 3.3: Interaction of gamma ray in liquid xenon

3.1.1 Scintillation efficiency

The average value to produce one photon in liquid xenon (W_{ph}) has been measured by several groups, and it is known that there is a linear energy transfer (LET) region so called "flat top response" where scintillation light is fully emitted without any reduction processes. In this region, W_{ph} is 13.8 ± 0.9 eV. Figure 3.4 shows the dependence of relative scintillation yield on LET. Lines in the figure is calculations with using different η_0 parameter. η_0 is the scintillation yield at zero electric field in the limit of zero LET. Low LET region and high LET region have less yields than "flat top response" by different reasons. In the case of electrons and gamma rays in the low LET region, the decrease is due to escaping electrons. Because the mean interval of electron-ion pairs produced by a minimum ionizing particle is comparable with the Onsager radius (49 nm), a large number of electrons will not recombine with the parent ion. At the Onsager radius, Coulomb energy is equal to the thermal energy. By this reason, scintillation yield depends on the density of ions, therefore it depends on LET. Reduction factor of yield of 1 MeV electron was measured to be 0.64 ± 0.03[32]. In the case of the very high excitation density, it is considered that quenching can happen by following process before forming excited molecules. Reduction factor of yield of 5.3 MeV alpha particle was measured to be 0.77 ± 0.04[32].

$$\mathrm{Xe}^* + \mathrm{Xe}^* \rightarrow \mathrm{Xe} + \mathrm{Xe}^+ + e^- \tag{3.8}$$

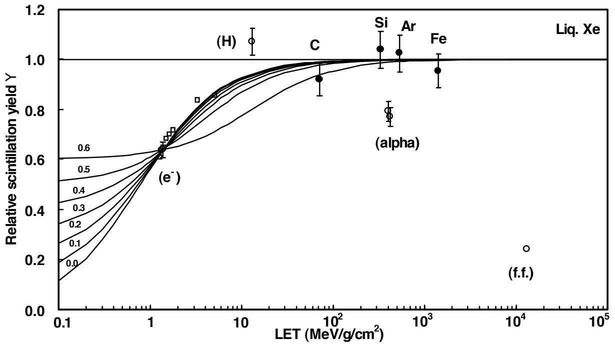

Figure 3.4: Dependence of scintillation yield on LET in liquid xenon. Solid circles represent yields for relativistic heavy particles whereas open circles represent those for electrons, alpha particles and fission fragments. Open squares represent gamma ray.[32]

3.1.2 Attenuation of scintillation light and impurities

Attenuation consists of scattering and absorption. Scattering length depends on wavelength of photons, density and the refractive index of the liquid. Attenuation length of liquid xenon has been measured and reported by several groups[31][33][34][35] to be 30 to 50 cm. Scattering length for a single component system can be calculated using the formula given in Landau and Lifshitz[37].

$$h = \frac{\omega^4}{6\pi c^4}\left[kT\rho^2\kappa_T\left(\frac{\partial\epsilon}{\partial\rho}\right)_T^2 + \frac{kT^2}{\rho c_V}\left(\frac{\partial\epsilon}{\partial T}\right)_\rho^2\right] \tag{3.9}$$

where ω is the angular frequency of the radiation, c is the velocity of light, k is Boltzmann constant, T is the temperature, ρ is the liquid density, c_T is the isothermal compressibility, c_V is the heat capacity at constant volume, and ϵ is the dielectric constant. These thermal properties of rare-gases can be found in ref.[38]. By using measured dielectric constants(2.85), scattering length of pure liquid xenon for 174 nm light was calculated to be 30 cm[31].

Since scintillation photons of xenon are emitted from exited dimers, there is no self-absorption. Hence, if the liquid is completely pure, the liquid would be transparent to its radiation. However, ultra-violet light is very sensitive to impurities. Major impurities for liquid xenon scintillation are water and oxygen. Figure 3.5 shows relative light intensity in liquid xenon as a function of distance from a light source for various amount of impurities. As seen in these figures, contribution of water is much higher than oxygen.

WArP collaboration recently measured effects of nitrogen and oxygen contamination in liquid argon[43][44]. In these articles, effect of quenching by following reaction is discussed.

$$Ar_2^* + N_2 \rightarrow 2Ar + N_2 \tag{3.10}$$

Quenching factor for 1 ppm contamination is about 80 % and 60 % for nitrogen and oxygen respectively. It was reported in these articles that when quenching happens, longer time component is reduced and pulse width becomes narrower than pure argon.

For large liquid xenon detector for MEG, impurities need to be reduced at least down to 10 ppb, 100 ppb, 100 ppb for water, oxygen and nitrogen respectively.

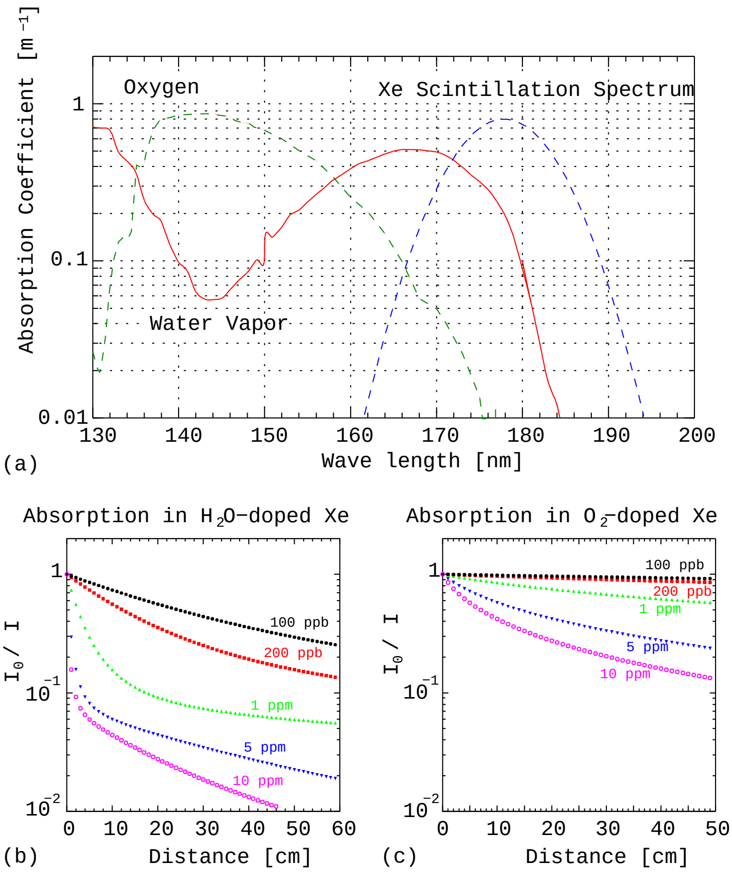

Figure 3.5: (a) Absorption coefficients for 1 ppm water vapor and 1 ppm oxygen [39][40][41][42]. Superimposed is the xenon scintillation spectrum. (b) Scintillation light intensity as a function of the distance from the light source for various concentrations of water in liquid xenon. (c) Same as (b) but for oxygen.

3.2 Liquid xenon gamma ray detector of MEG

Figure 3.6 is a schematic view of the MEG gamma ray detector. A C-shaped gamma ray detector is located beside the positron spectrometer. Definition of six faces of the PMT holders (inner, outer, upstream, downstream, top and bottom) are shown in the figure. It covers 10 % of the solid angle viewed from the muon stopping target. The cryostat of the gamma ray detector is filled with over 800 litters of liquid xenon surrounded by 846 photo-multiplier tubes (PMT). The PMTs are immersed in the liquid xenon to observe scintillation photons directly. Gamma rays from the target enter the active volume of the detector through an entrance window consisting of an aluminum honeycomb and carbon fiber plates. Then a gamma ray interacts with the liquid xenon and deposit energy to excite xenon molecules, resulting in emission of a large amount of scintillation light. The scintillation light yield is as large as 80 % of NaI. The decay time of scintillation is five times faster than that of NaI. Because of these properties, the liquid xenon scintillation detector is expected to have excellent performance to measure energy, position, and time of gamma rays.

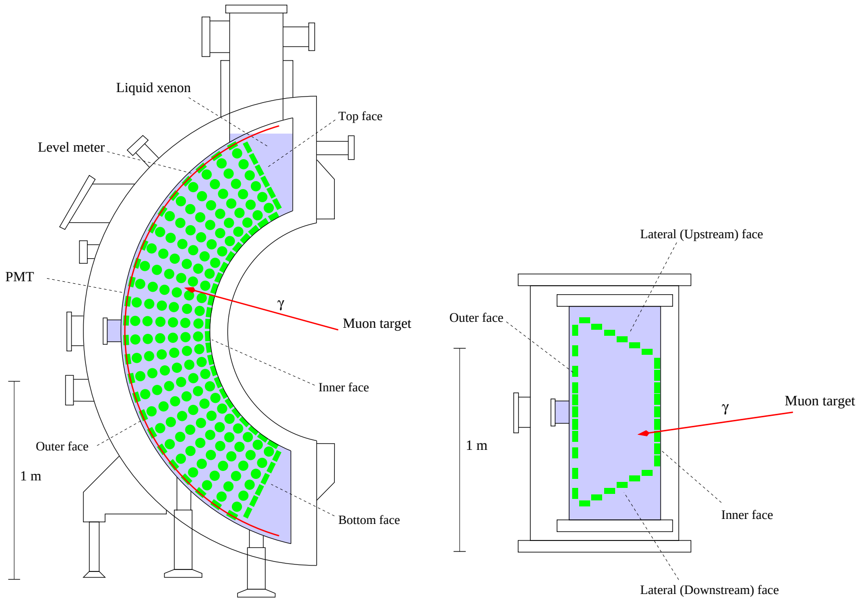

(a) (b)

Figure 3.6: Schematic view of the MEG gamma ray detector. (a) Side view (b) Top view

The acceptance of the experiment corresponds to an area shown in fig.3.7.

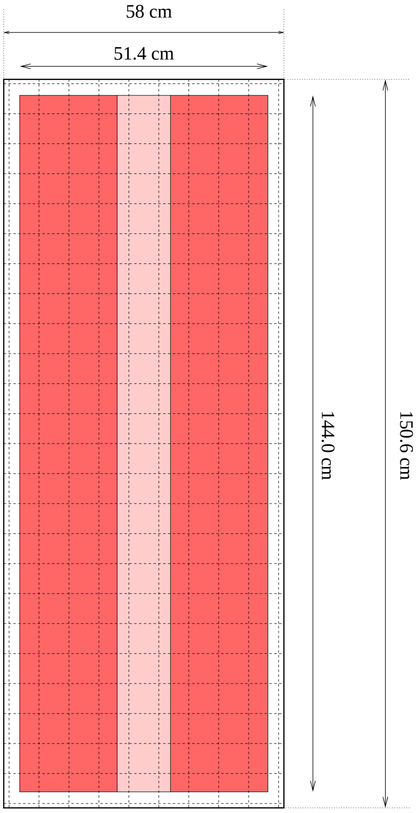

Figure 3.7: Projection of the acceptance of the experiment to the inner face of the gamma ray detector. Red boxes correspond to the acceptance of the experiment. The center part shown in light pink is a part of the acceptance of the gamma ray detector, but corresponding back-to-back direction is not in the acceptance of the positron detector because signal positrons in the angular range do not hit the timing counter.

3.2.1 PMT for the gamma ray detector

A new model of metal channel PMT was developed by MEG collaboration and Hamamatsu photonics. The photo-cathode material is K-ScSb. This is designed such that it can be immersed in liquid xenon and it can observe scintillation light of liquid xenon directly. For this purpose there are several points to take care of. Scintillation light of liquid xenon is vacuum ultraviolet(VUV) which has a peak at 178 nm. Normal PMT windows made of glass is not transparent to the light. Therefore in many experiments, scintillation photons are measured after shifting wavelength longer. The PMT for MEG is equipped with a quartz window which is 80 % transparent to the scintillation light. Pressure of the liquid xenon in the detector is usually controlled to be around 0.12 MPa. However, it can be about 0.2 MPa during transfer. The cryostat is evacuated before filling it with xenon. So, the PMTs must be tolerant to pressure from 0 to 0.2 MPa. Heat generation by PMTs is one of major sources of heat load of the detector. In order to minimize the heat generation, current of the HV line is relatively low. Usually, it is around 60 μA during measurement in MEG. During the measurement of muon decays, there are high rate background scintillations by gamma rays and neutrons. To stabilize PMT gain under high background conditions, Zener diodes are put at the last two steps as shown in fig.3.9. Thanks to these diodes, gain variation due to background is in a few % during the measurement depending on individual PMTs. Resistance of cathode become higher in low temperature than in room temperature. To avoid Q.E to be decreased in a low temperature, aluminum strips are attached on the surface of cathode as shown in fig.3.8-b.

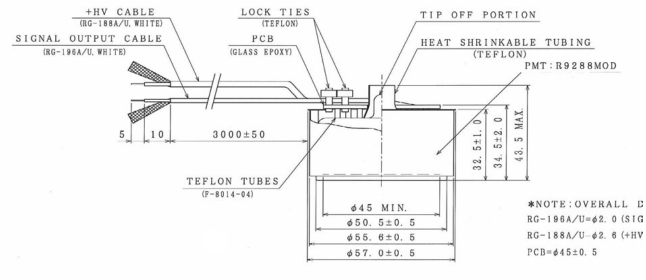

(a)

(b)

Figure 3.8: Hamamatsu R9288.

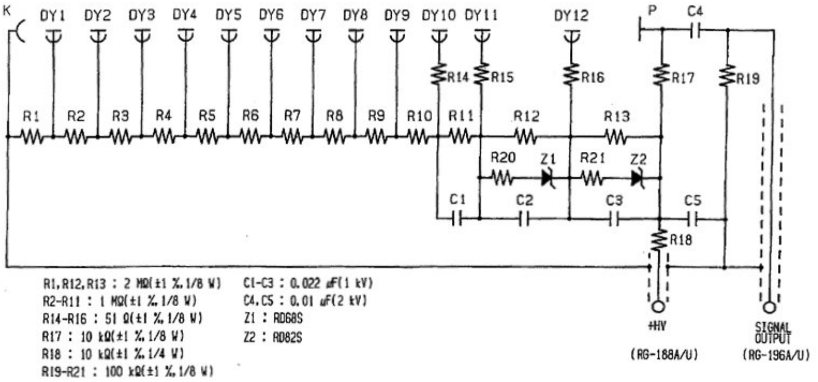

Figure 3.9: Base circuit of R9288.

3.2.2 Cryostat

Because the cryostat is located in a strong magnetic field, it is made of non-magnetic materials. Materials with low permeability were carefully chosen to build the cryostat in order to reduce magnetic field around PMTs. Deformation and stress of the cryostat was studied by using simulation during designing with taking into account weight of liquid xenon.

The cryostat consists of inner and outer vessels. The volume between the two vessels is evacuated for thermal insulation. Super insulation layers are installed between the two vessels to suppress heat income due to radiation.

Xenon is liquefied by a pulse-tube refrigerator and a liquid nitrogen cooling pipe equipped at the top of the cryostat. After the liquefaction, the liquid xenon is kept in a stable condition by the refrigerator. The effective cooling power is controlled by a feed back system. Another line of LN_2 is attached on the outside of the inner vessel to directly cool the vessel. This is used mainly for pre-cooling of the vessel before starting liquefaction. The system can be used also when there is a problem to use the LN_2 at the top of the cryostat. Pictures of the second LN_2 line is shown in fig.3.10.

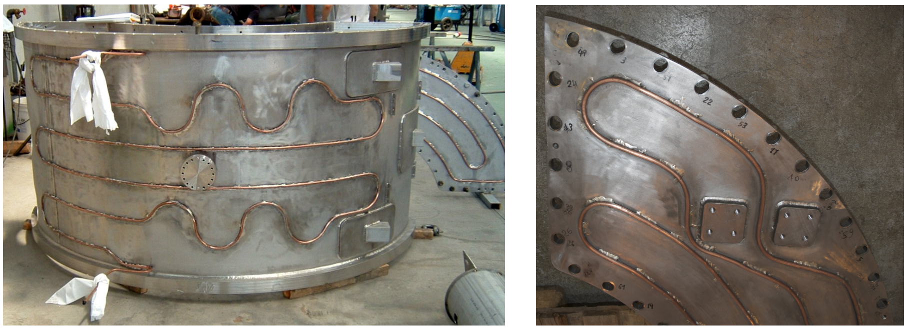

Figure 3.10: Liquid nitrogen pipe attached on inner vessel.

For measuring the level of the LXe, a capacitance level-meter is installed. The temperature of the xenon is measured by 27 pt-100 sensors located at various positions. Additional temperature sensors are attached on the outside of the inner vessel to monitor temperature of the cryostat. All the cables from PMTs and sensors installed in the inner vessel go to feedthroughs attached on chimneys at the top of the detector. A turbo molecular pump and a cryo-pumps are directly attached at the chimney to evacuate with a high conductance. Since water vapor is the largest component of the residual gas in the case of MEG gamma ray detector, a cryo-pump works very well.

The inner vessel is designed to minimize heat coming from room temperature part. For example, bellows plates are used to connect inner vessel with the top chimney. Total heat load is shown in table 3.4. The largest sources are heat generation by PMTs and conduction of PMT cables.

Radiation	Outer Vessel → Inner Vessel (30 Mylar layers)	3.1 W
Conduction	Nozzle via xenon gas	0.2 W
Conduction	Nozzle via bellows	4.6 W
Conduction	Support (brace and supporting pipe)	6.3 W
Heat generation	PMT (65 mW/PMT)	52 W
Conduction	PMT HV and Signal Cables	50 W
Total		116.2 W

Table 3.4: Heat load of the gamma ray detector

Gamma ray entrance window is designed to be as thin as possible in order to minimize the probability of gamma rays converting in it. As well as that, mechanical strength is required in wide range of temperature from 165 K to room temperature. To satisfy these constraints, aluminum honeycomb panel covered with carbon fiber plates was chosen. The panel was produced by an Italian company Plyform. Three types of honeycomb panels was produced with different materials and designs. First two panels failed during pressure tests. In both tests, cracks appeared at the edge of carbon fiber plates. After optimization of the design, the third panel successfully passed all the tests. Pressure test was performed up to 0.5 MPa and no damage was found. For the third panel, low modular and good elongation carbon fiber(T300) was used. The plates consists of eight piles, and the total thickness is 1.5 mm, glued with epoxy-resin (Hysol EA9361). The window consists of the central honeycomb of 24 mm thickness, reinforcement, internal and external skins. The central honeycomb made of aluminum and skins are made of carbon fibers. All these parts are glued. Pictures of these parts and the complete panel are shown in fig.3.11. The gamma ray entrance window on the inner vessel consists of the honeycomb panel and a stainless steel plate of 0.4 mm thickness welded from the inside. That on the outer vessel is a 0.7 mm thickness stainless steel plate welded from the outside

In total, thickness of the window corresponds to 0.075 radiation length.

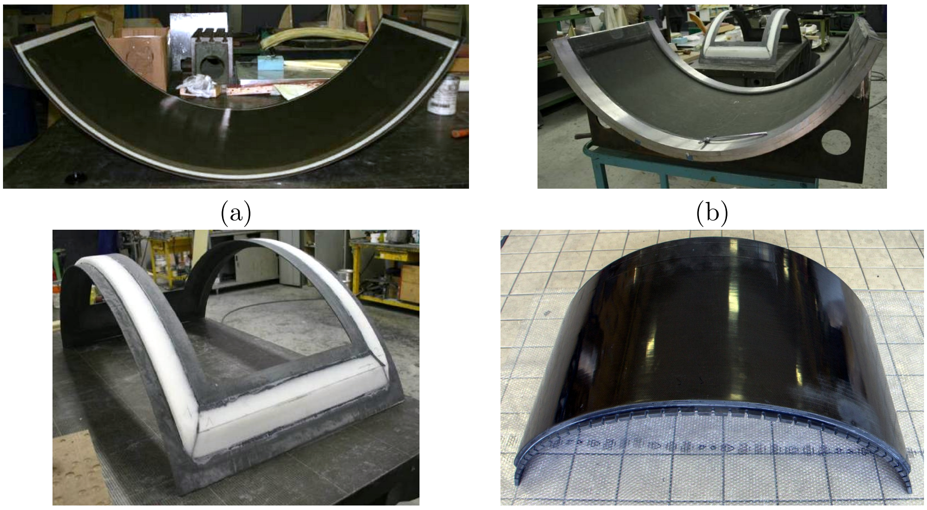

(a) (b)

(c) (d)

Figure 3.11: Pictures of honeycomb panel. (a) Inner skin. (b) Outer skin. (c) Reinforcement. (d) After gluing all the parts.

3.2.3 Handling of xenon

The gamma ray detector for MEG is the largest xenon detector ever made, which utilizes around 1000 litters of liquid xenon. This is the first time to handle such a large amount of xenon. Since xenon is expensive and production is not very fast, the xenon system was designed not to throw away xenon during experiment. Figure 3.12 shows a schematic view of xenon system of MEG. There are two types of storage. The one (GXe storage) consists of eight tanks with each 250 litters of volumes. And the other (LXe storage) can store about 1000 litters of xenon in liquid phase. A purification system is installed between two storage systems to purify GXe when it is transferred from the GXe storage tanks to the LXe storage tank or to the detector.

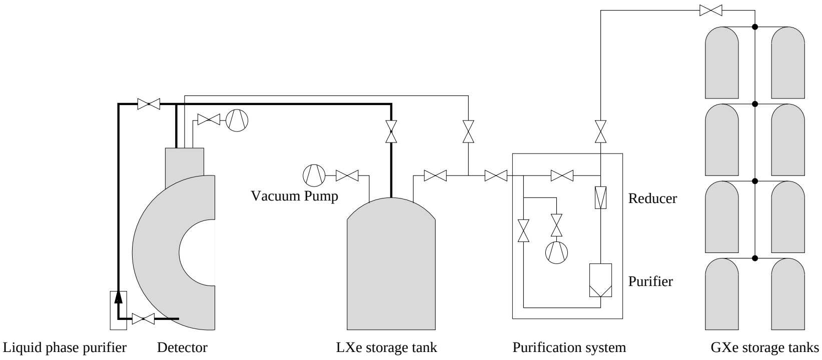

Figure 3.12: Xenon line. Thicker lines in the figure between detector, liquid phase purifier and liquid storage are vacuum insulated pipes for liquid xenon transfer.

Figure 3.13 is a photograph of the GXe storage tanks produced by Taiyo Material Inc. Pressure of xenon is not increased linearly as a function of density as shown in fig.3.14. GXe tanks are tolerant to 8 MPa, thus can contain up to 1.44 g/cm^3, 360kg of GXe (it is equivalent to 120 liters of LXe).

Figure 3.15 shows a schematic view and a photograph of the LXe storage tank produced by Taiyo Nippon Sanso Co. The purification system is shown in the right part of the photograph. The specification of LXe storage tank is summarized in table 3.5. The LXe storage tank consists of inner and outer vessels. Xenon is stored in the inner vessel in liquid phase. The volume of the inner vessel is 1110 liters, and the maximum storage quantity is 1000 liters. From cryogenics point of view, the structure is similar to that of the gamma ray detector. A test of the LXe storage tank was done and it was checked that the heat income is same as expected(20 W). When all cooling systems were stopped, the pressure was increased from 0.11 MPa to 0.2 MPa in 43 hours. So, the cryogenic system is safe even when there is no electric power and control for certain period.

Xenon in the GXe storage tanks can be transferred to the LXe storage tank or the detector by making use of a pressure difference. When GXe is transferred to the LXe storage tank, GXe is liquefied in the LXe storage tank continuously, and the pressure is kept to be around 0.1 MPa. Xenon can be transferred until an equilibrium is established between the pressure of LXe storage tank and the

Figure 3.13: GXe storage tanks in the experimental area

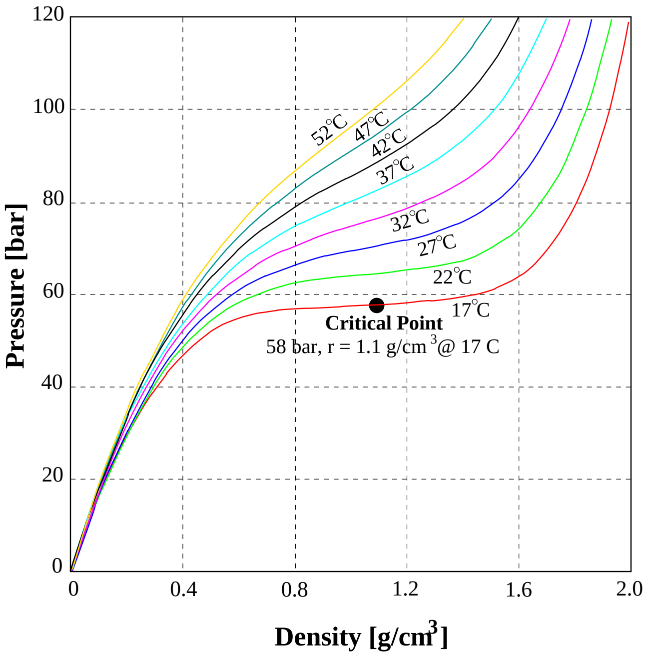

Figure 3.14: Temperature and density of gas xenon.

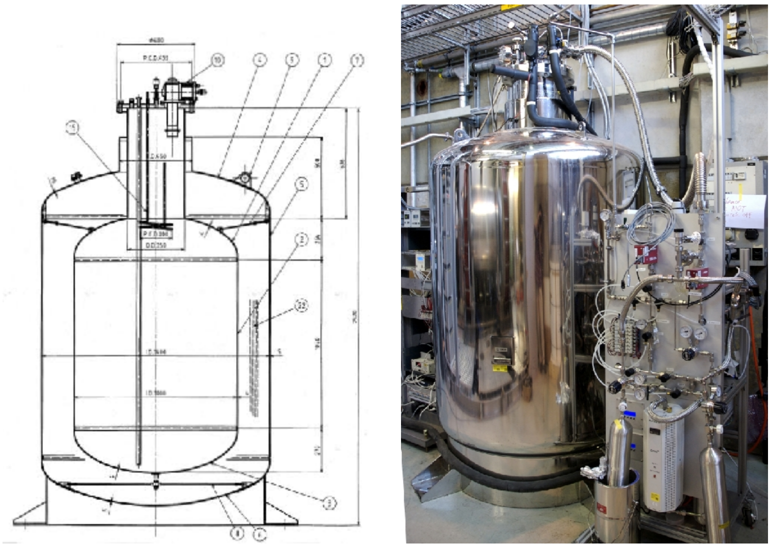

Figure 3.15: (a) Schematic view and picture of the LXe storage tank. (b) A photograph of LXe storage and gas purification system.

Dimension	$\phi1400 \times 2570\text{mm}^2$
Volume	1110 L (Max storage 1000L)
Design pressure (DP)	0.6013 MPa
Hydrostatic test pressure	0.91 MPa (1.5 x DP)
Air test pressure	0.67 MPa (1.1 x DP)
Design temperature	-196 $\sim$ 40 °C
operation temperature	165 K
Material	SUS304
Designed heat income	$<$ 20 W
Inner surface treatment	electrochemical polishing

Table 3.5: specification of LXe storage tank

GXe storage tanks where about 1.5 kg of GXe remain in the GXe storage tanks. The LXe storage tank is connected to the detector by vacuum-insulated pipes to transfer the xenon in the liquid state by making use of a pressure difference. It makes the transfer much faster than that in gaseous state. The speed of transferring xenon in gaseous state is limited by the cooling power for liquefaction of xenon. Xenon will be kept in either the detector or the LXe storage tank while MEG experiment is running. However during long-term shutdown of the experiment such as a detector upgrade, xenon will be stored in the GXe storage tanks because no control systems or electric power are needed. In order to recover xenon to the GXe storage tanks, GXe storage tank is cooled by LN_2 filled in Dewar in which tanks are located, and the LXe storage tank is pressurized up to 0.18 MPa by using heaters installed at the bottom. Then,evaporated xenon is transferred to GXe storage tank, and solidified continuously. After recovering all xenon from the LXe storage tank, and valves of the GXe storage tanks are closed, the cooling of the GXe storage tanks is not necessary any longer. Suppose that the temperature of the xenon inside the GXe storage tanks reaches low enough (less than 100K), xenon remained in the LXe storage tank can be expected to be negligible.

A heated purification getter[45] is equipped in the purification system. The purifier removes H_2O, O_2, CO, CO_2, H_2, N_2 and hydro carbon molecules from GXe down to 1.0 ppb. Gas purification test with 100 liters of xenon by using a similar purifier is described in ref.[46][47]. It was confirmed that the impurities, mainly water, were successfully reduced, and an adequate performance for the MEG photon detector could be achieved. However, purification in gas phase is relatively slow, hence it is not suitable for the final gamma ray detector, which utilizes much more xenon. Therefore a purification system with circulation of xenon in liquid phase was developed[48]. A similar system was firstly tested by using the large prototype detector. And it was found that the system reduces amount of impurities from 250 ppb to less than 40 ppb in 5 hours operation for 100 litters of xenon. Figure 3.16 is a picture of the liquid phase purifier equipped to the final detector. In the purifier vessel, centrifugal pump and purifier (molecular sieves) are installed. The system is connected with the detector by vacuum insulated pipes to circulate xenon through the purifier in liquid phase. The pump has a capability to flow xenon up to 71 liters per hour. The speed is much faster than gas purification (60 c.c. liquid per hour).

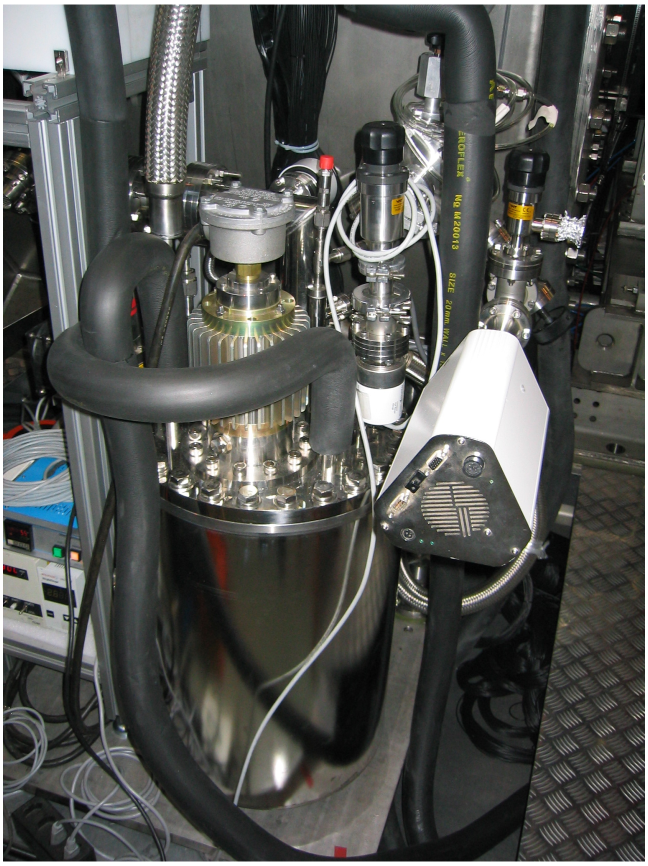

Figure 3.16: Liquid phase purification system

3.2.4 PMT test

About 1000 PMTs were tested before installed into the gamma ray detector. The half of them were tested at PISA test facility[49] and the others were tested at PSI with using the large prototype detector. In the test, gain at 800 V of H.V., Q.E. and dark current was measured. Bad PMTs (problem of base circuit, low gain or low Q.E.) were repaired or eliminated from the list of usable PMTs. In addition, shape of glass tube was measured in a precision of a few ten μm, because a PMT may not fit to the PMT holder of the inner face if the shape is too much different from the typical one. PMT holders of the inner face have more fine structure than other faces.

Since PMTs in the inner face is important, we have chosen suitable PMTs for the part. In figure 3.17, measured gain and Q.E. of currently installed PMTs are shown. To make response of the detector as uniform as possible, center part of Q.E. distribution was chosen for inner-face. For low gain PMT, H.V. will be higher when gain is adjusted to be a certain value. In general, higher H.V. gives better linearity and smaller transit time spread (TTS). By this reason, low gain PMTs were chosen for inner face.

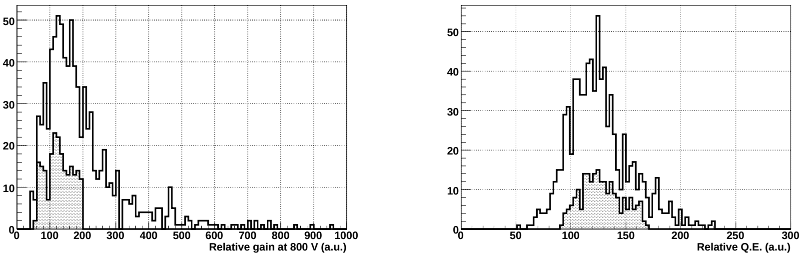

Figure 3.17: Measured gain and Q.E. in PMT test. Hatched part is PMTs used in inner face.

3.2.5 Alignment

Before installing PMTs. In the cryostat, targets to measure positions are attached to rails for PMT holders. The position was measured by using laser. Correct position was marked on the platform for locating the detector after installing PMTs. It was done with accuracy better than 1 mm and the error is negligible compared to position resolution of the detector. Figure 3.18 is photographs during the alignment.

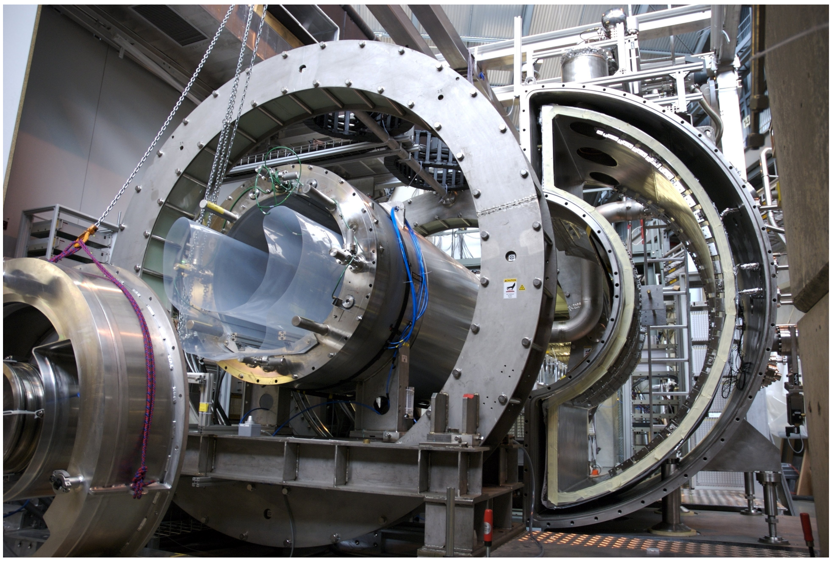

Figure 3.18: Photographs during alignment of the gamma ray detector. A target for the alignment is attached to the rail on the inner face.

3.2.6 Installation of PMT

PMT holders consist of several slabs, as shown in fig.3.20, so that the assembly of slabs can be done separately. In inner and outer faces, 9 PMTs are in a slab. In lateral faces, 6 PMTs are in a slab. Top and bottom faces are each one big plate containing 54 PMTs. Holders except for the inner face are made of aluminum. PMTs and holders are electrically isolated by Teflon parts to make the ground level of PMT independent of cryostat's level. The holder of the inner face is made of PEEK to decrease material between the active volume and the target. The design of the inner PMT holder is carefully done not to make rooms where liquid xenon can enter. Spaces behind PMTs were filled Delrin parts and small grass beads to avoid base circuits are destroyed by deformations of materials in a low temperature. Cables are embedded in STYCAST as shown in fig.3.19 to fit the shape of holder. If there is a void in STYCAST used to form a cable structure, air inside the void can leak during experiment, and it can contaminate liquid xenon. To void it, STYCAST is put in vacuum before it is hardened to eliminate air contained in it. The cable structure was made carefully not to make voids. Assembled slabs are mounted as shown in fig.3.20. Gaps between inner surface of cryostat and holders smaller than 0.75 mm were filled by using Teflon sheets of 250 μm thickness.

Figure 3.19: Installation of PMTs in inner a face holder.

After the slabs were mounted, cables were connected to inside-patch-panels, then to feedthroughs. All the electrical connections were checked, and PMT signals were checked by using an oscilloscope. Other components for monitoring and calibrations such as alpha sources, LEDs, temperature sensors, level meters were installed. As shown in fig.3.21, after installing all the parts, aluminum blocks were put to reduce empty spaces so that necessary amount of xenon was decreased.

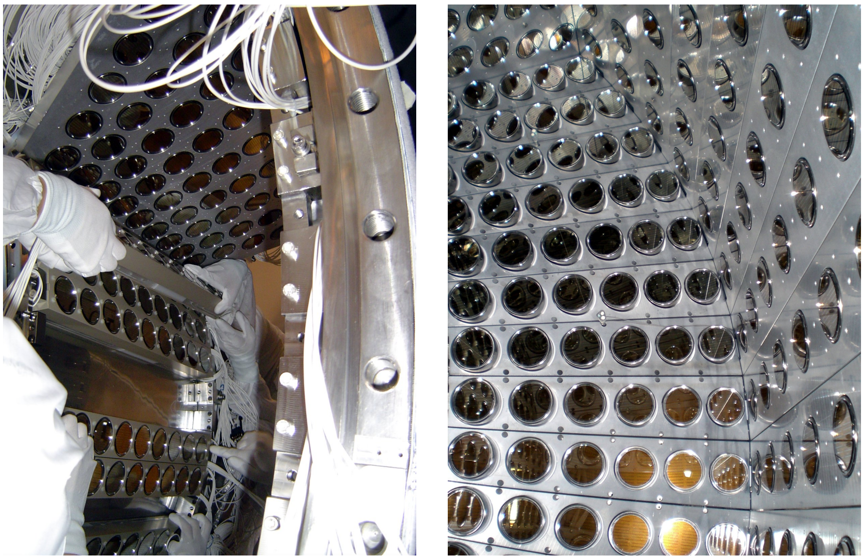

(a) (b)

Figure 3.20: Installation of PMT holders. (a) Inner face. (b) Lateral and outer face.

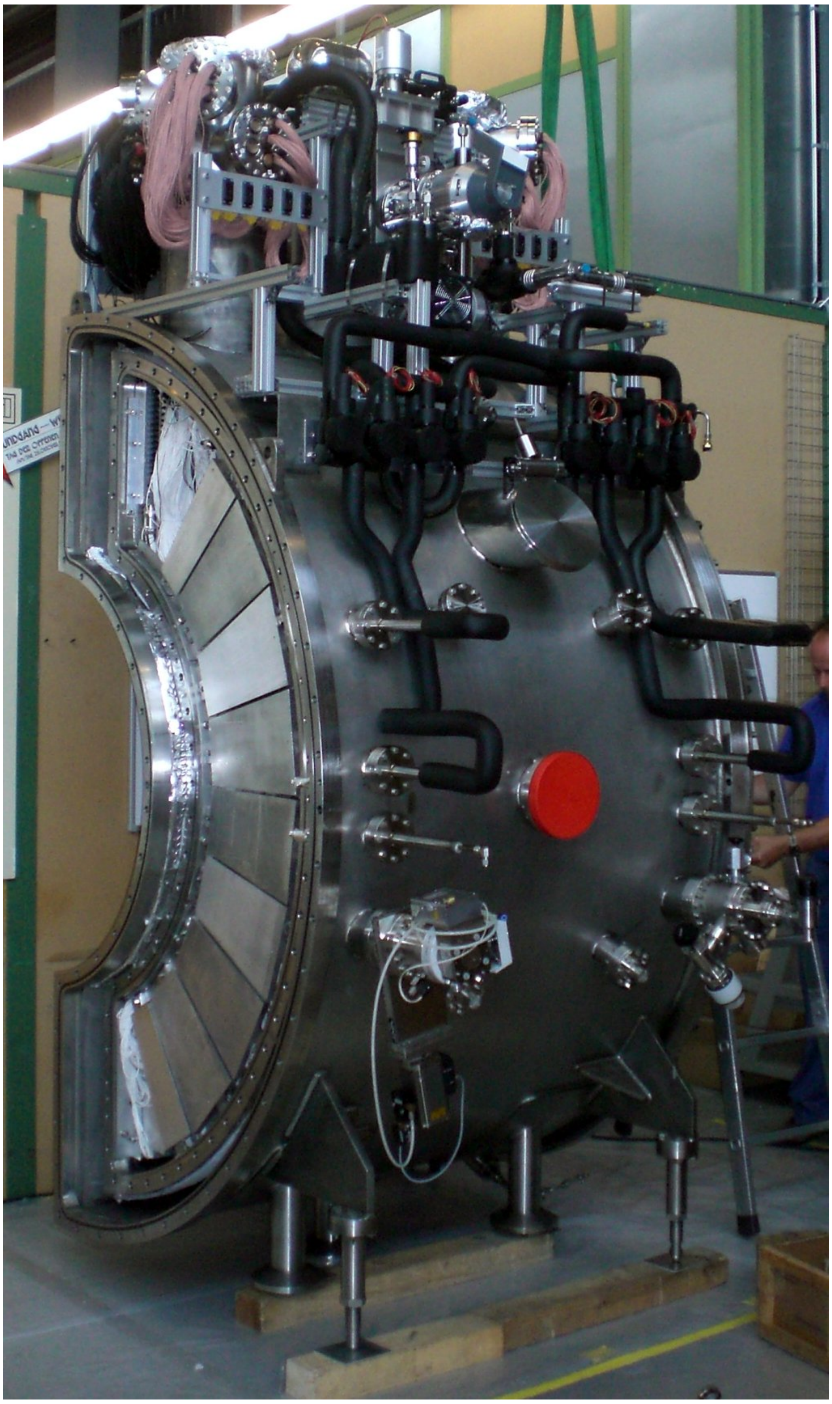

Figure 3.21: A picture after installing every part to the cryostat.

3.2.7 Slow control of the system

The slow control system in MEG is controlled by electronics using the MSCB[50] system developed in PSI. Each control node connected to MSCB bus has a micro-controller. A picture of two SCS-2000 nodes is shown in fig.3.22. Up to eight daughter cards can be inserted in a module. Several daughter cards are available such as ADC, DAC, capacitance meter, current source and relays. One node has up to 64 I/O channels.

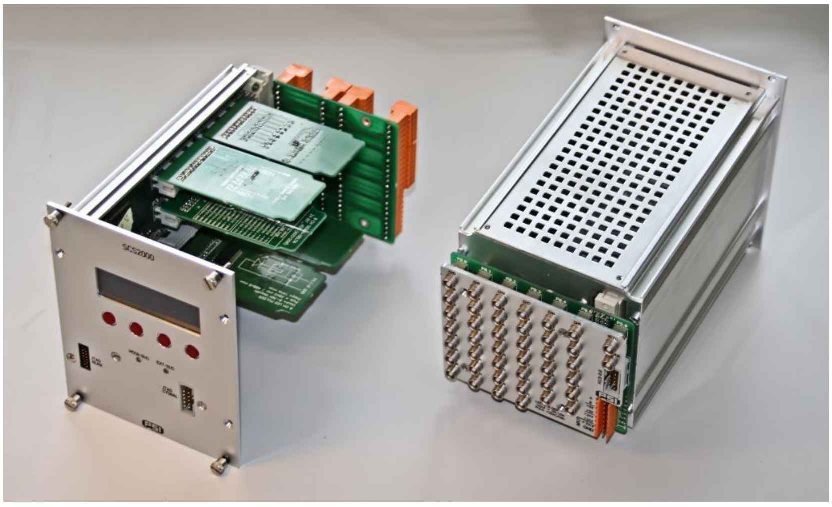

Figure 3.22: A picture of a SCS-2000 node. The right one is used as a LED pulser and has LEMO connectors instead of normal back-plane.

They control the xenon system by making use of proportional-integral-derivative (PID) control algorithm which is a generic control loop feedback mechanism widely used in industrial systems. The control nodes handle valves (open/close), equipments such as pumps, and acquires the system status (temperatures, pressures and so on). Firmwares were developed specially for the xenon system. Variables in the processor can be overwritten either through front panel of each node, or through MSCB bus without interrupting the operation. MSCB bus can be connected to computers with USB or Ethernet adaptor.

Status of the system is monitored by using LabVIEW[51] panels running on a remote computer. The panels are prepared to show the status graphically, to change control parameters, and to use alarm system. Control nodes have a connection to the computer over Ethernet by using MSCB bus adapters. The system is not affected even if the computer on which LabVIEW program is running has some problems, because algorithms and all the variables are on the memories of micro controllers in the control nodes. A part of the LabVIEW panel is shown in fig.3.23. An alarm system is implemented in the LabVIEW panels so that emails are sent to mobile phones when the pressure of LXe storage tank or the temperature of LXe becomes out of a certain range or the connection between the computer and the control nodes is lost. The status of almost all valves can be changed through the panel so that the storage system can be fully controlled remotely even when the beam area is closed.

Control of xenon system consists of four sub-systems. Namely, the detector, the LXe storage, the GXe storage and GXe purification system as shown in fig.3.24. The LXe purifier is included in the detector's part. All the necessary values for controlling each sub-systems are read in the node so that each sub-system works independently.

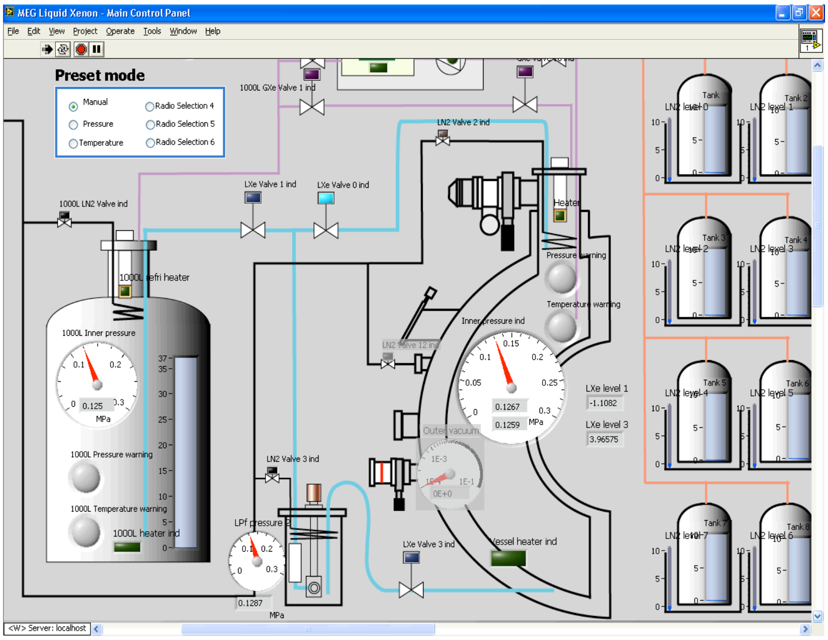

Preset mode

● Manual ○ Radio Selection 4
○ Pressure ○ Radio Selection 5
○ Temperature ○ Radio Selection 6

Figure 3.23: A part of LabView control panel. All the valves drawn here can be controlled from the panel. Pressures and status of heaters are shown in this part.

Relation between pressure and temperature of xenon is shown in fig.3.25. During the experiment, pressure is controlled to be stable around 0.13 MPa.

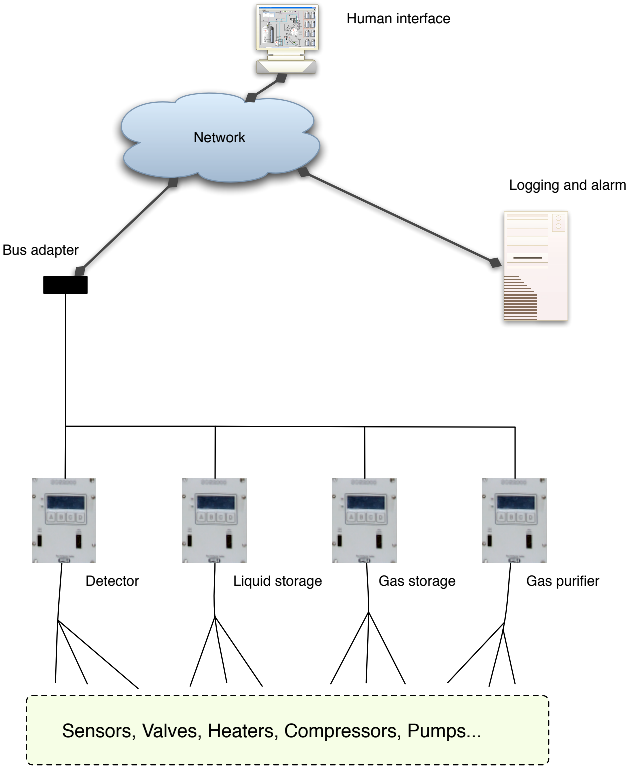

Figure 3.24: Slow control system of the gamma ray detector. Four SCS-2000 control nodes read sensors and handle valves, heaters and so on. Variables in the nodes can be monitored or changed from computers over network by using several interfaces.

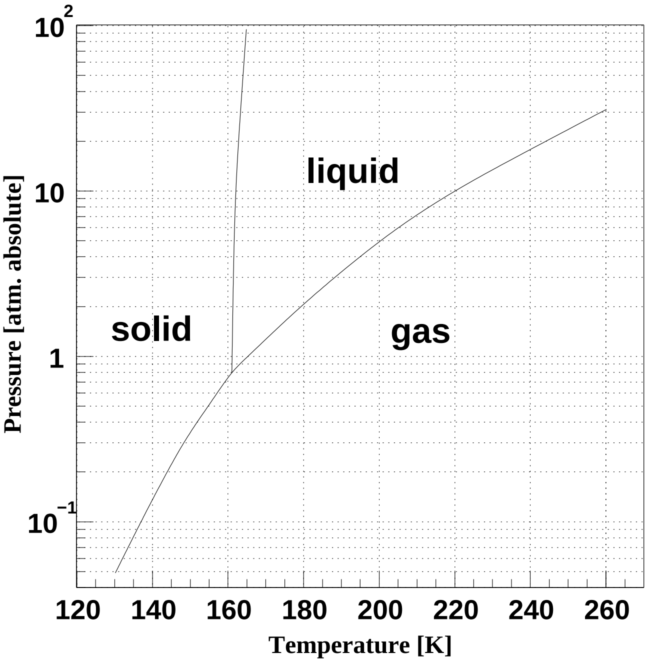

Figure 3.25: Phase diagram of xenon

3.2.8 Electronics

Figure 3.26 is a schematic view of the connection from PMTs to DRS, trigger system and H.V.. Coaxial cables from PMTs are connected to a patch panel located in the cryostat. Here, lines for signals and high voltages are separated and go to each feedthrough. Signal cables are connected with active splitters through a patch panel. After the splitters, signals are sent to trigger and DRS boards. DRS and trigger boards are described in section 2.4. High voltage cables are connected with voltage dividers through patch panels. Pictures of outside a patch panel and a feed through is shown in fig.3.27.

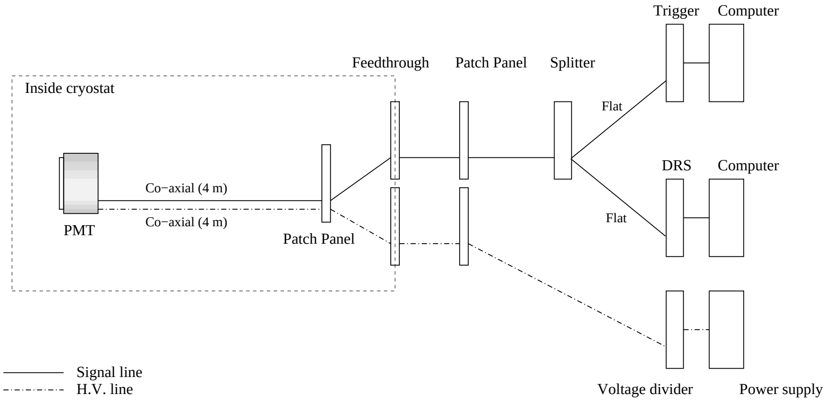

Figure 3.26: Connection from PMT to electronics

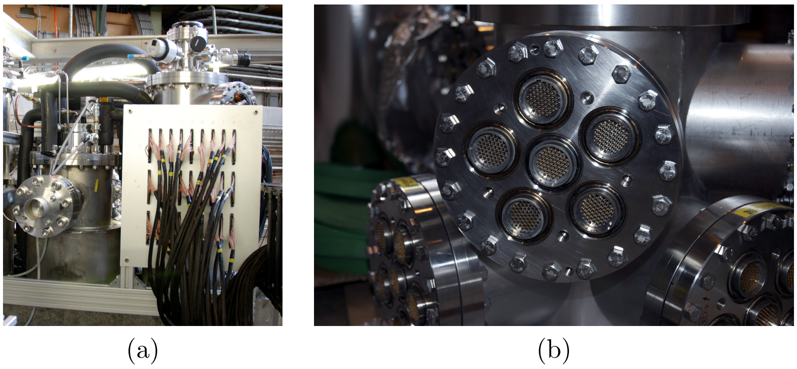
(a) (b)

Figure 3.27: Picture of (a) outside patch panel and (b) feedthrough.

Chapter 4

Simulation

Simulation of MEG experiment is done by two programs. The one is based on Geant3, and it includes event generation starting from a muon decay on the target or a muon beam, particles tracking and sub-detector responses simulation. The other was written from the scratch in MEG collaboration with using ROOT package. This program reads several output files from the detector simulator, merges several events to simulate accidental pileups, and makes waveforms by simulating electronics devices. Digitization of waveforms are also simulated, and the result is written in the same format with experimental data.

4.1 Scintillation photon tracking in the gamma ray detector

At each energy deposit position in the active volume of the gamma ray detector, scintillation photons are generated isotropically according to the energy deposits and assumed scintillation efficiency. Scintillation efficiency is different depending on particles. During the tracking, several optical processes such as Rayleigh scattering, absorption by impurities, reflection on walls or PMT windows, transmittance of PMT window and efficiency of photoelectric effect on cathodes are simulated. Arrival time of photons at each PMTs are recorded in output files.

4.2 Gamma Ray Detector waveform simulation

Waveform simulation includes multiplication in PMT, attenuation of pulses in cables, reflection by impedance mismatching, clipping and smearing in electronics and digitization on read out chips. It is done by using photon arrival time information from the detector simulator.

Two ways were prepared for the simulation. In one method, each processes are parametrized and simulated separately. Namely, transit time spread of PMT is simulated by a Gaussian distribution, attenuation is done by software filtering with assumed frequency cut off and so on. In the second method, simulation is done by convolution of photon arrival time with a known impulse response. The impulse response is obtained from real waveform and distribution of PMT hit

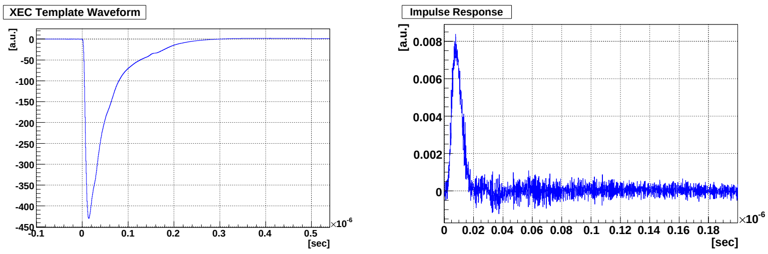

(a) (b)

Figure 4.1: (a) Template waveform created from real data. (b) Impulse response.

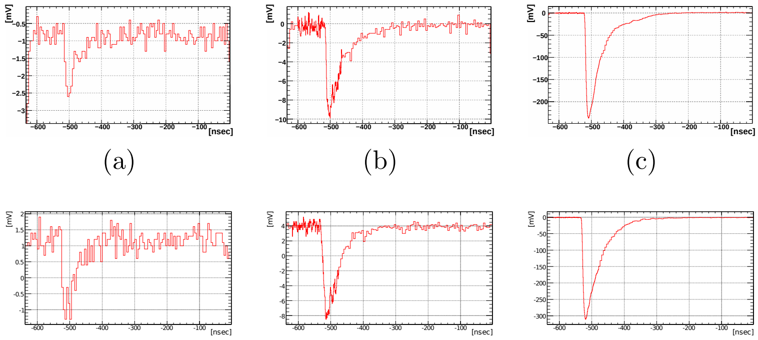

(a) (b) (c)

(d) (e) (f)

Figure 4.2: Waveform of real data(a)(b)(c) and simulation(d)(e)(f). Rebinning except around the peak is done for large pulses for data reduction.

time in MC simulation assuming scintillation decay time of 45 nsec. Deconvolution was done by Fourier-transform. Once we obtain the impulse response from data, the second method reproduces the data well. Template waveform created from real data, and impulse response created from the template is shown in fig.4.1 Gaussian noise can be simulated. Also for noise simulation, frequency dependent attenuation is taken into account. Figure 4.2 shows waveforms of real data and simulation for different pulse heights.

4.3 Response of the gamma ray detector

Figure. 4.3 shows the energy deposit in the active volume for signal gamma rays generated in the detector acceptance. The lower tail is due to gamma ray interaction before the active volume, and escape of gamma rays from the active volume. The probability of escape is larger in the shallow and very deep part. The detection efficiency calculated from the simulation of signal events is shown in fig. 4.4. About 40 % of gamma rays from muon decays impinge to the active volume without interacting with COBRA magnet or materials before the active volume. However due to escape, the efficiency depends on the energy threshold.

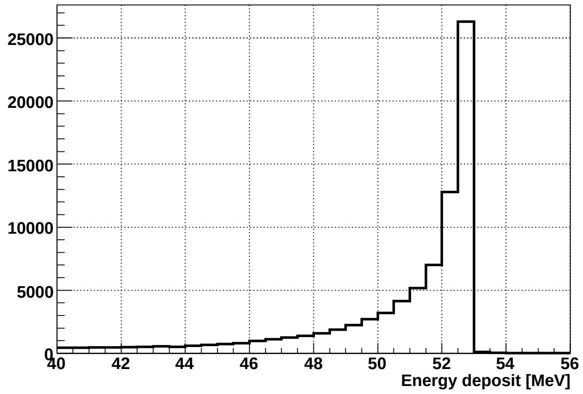

Figure 4.3: Energy deposit of simulated signal events in the acceptance.

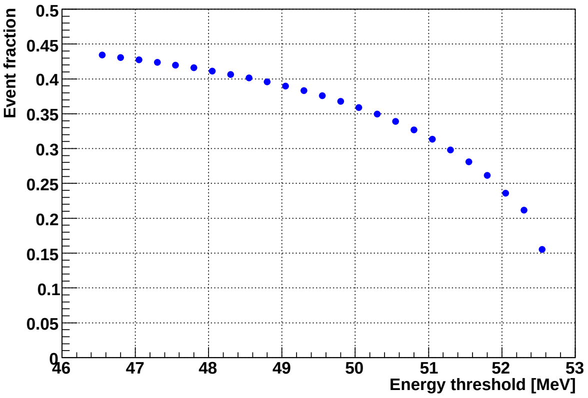

Figure 4.4: Efficiency of the gamma ray detector as a function of energy threshold.

Chapter 5

Prototypes

Before constructing the final gamma ray detector, a small prototype with 2.3 litters of fiducial volume and a large prototype with 68.6 litters of that were constructed. It was confirmed by the small prototype that the newly developed PMTs work with expected performance, and the detector has a good performance of gamma ray measurement for low energy gamma rays up to 4.4 MeV. The large prototype was build to check the performance for gamma rays of similar energy to the $\mu^+ \rightarrow \mathrm{e}^+\gamma$ signal. Figure 5.1 shows the comparison of the size of the final detector and the large prototype. The area of acceptance of the large prototype is much smaller than that of the final detector, however, the length along the direction of impinging gamma rays is almost same as the final one so that it has a similar performance to the final detector within the acceptance. During the large prototype experiment, techniques to handle and to purify a large amount of xenon were developed. Two kinds of beam tests were carried out, and it was confirmed that the performance of the prototype satisfies requirements of the experiment.

5.1 Small prototype

From 1998 to 1999, a performance test of the same type of detector was done with using a small prototype for low energy photons. The prototype consists of 32 PMTs surrounding 2.3 litters of active volume. Old type of PMTs(R6041Q) were used in this prototype. Figure 5.2 shows the schematic view of PMTs and the holder. The performance was estimated by using several radio active sources with various energies up to 4.4 MeV. Results are described in ref.[52] and [53]. Resolutions for various energies are shown in fig.5.3.

5.2 Large prototype

From 2000 to 2004, the large prototype was build and several beam tests were conducted in order to gain experience of the detector operation and to investigate its performance. Figure 5.4 shows cross-sectional views of the prototype. The cryostat consists of inner and outer vessels. The volume between the two vessels is evacuated for thermal insulation. Super insulation layers are installed between the two vessels to suppress heat income caused by radiation. Xenon is

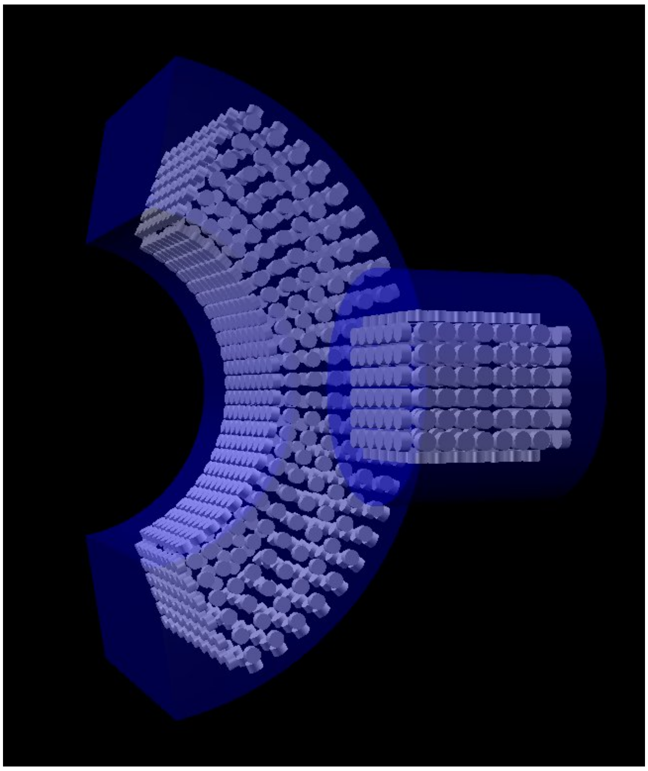

Figure 5.1: Comparison of the final detector and the large prototype

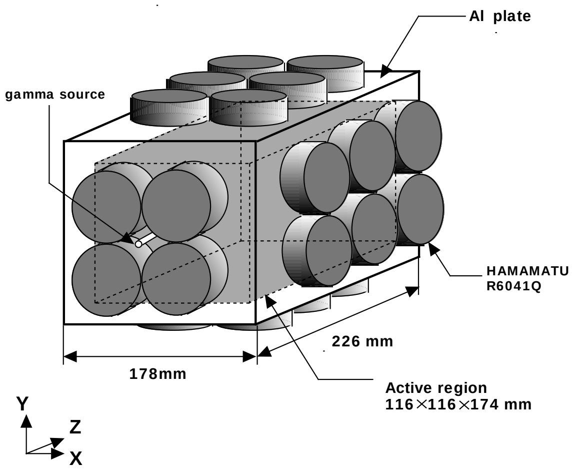

Figure 5.2: Schematic view of the small prototype

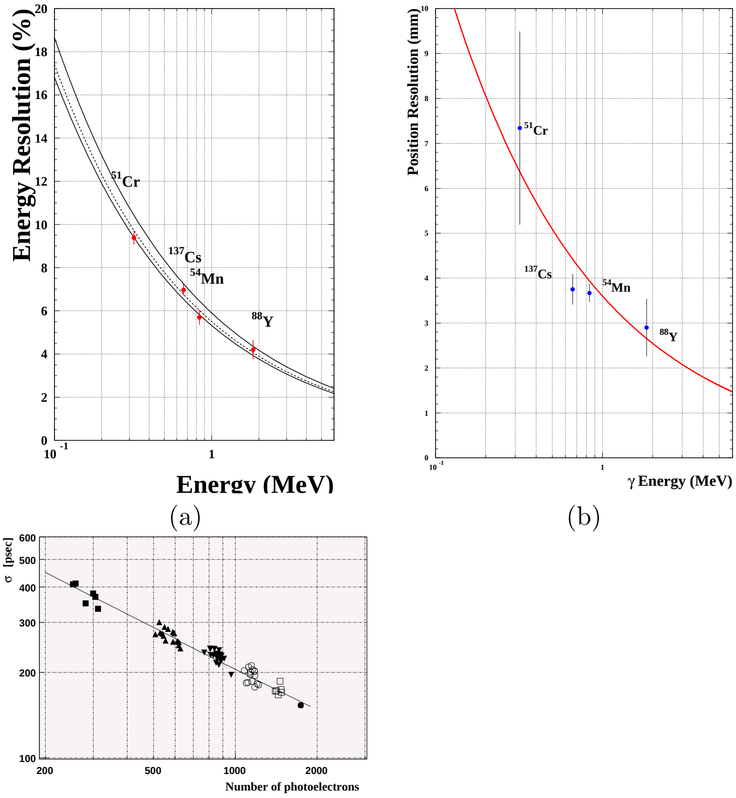

(a) (b)

(c)

Figure 5.3: Resolutions of the small prototype. (a) Energy resolution. (b) Position resolution. (c) Time resolution

liquefied by a pulse-tube refrigerator (Iwatani Co. Ltd) and a liquid nitrogen cooling pipe equipped at the top of the cryostat. After the liquefaction, the liquid xenon is kept in a stable condition by the refrigerator.

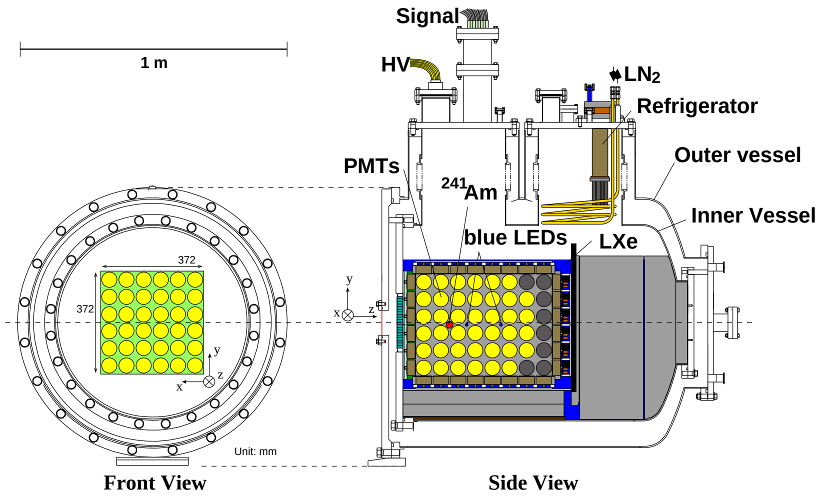

Figure 5.4: Liquid xenon gamma ray detector prototype. PMTs are installed on six faces of a rectangular solid holder. PMTs were not installed in grey circles in this figure.

The entrance window consists of a 0.1 mm thick aluminum plate and a 20 mm thick stainless steel honeycomb. The holder for the front-side PMT is made of G10 and Acrylic plates. The gap around the PMT base circuit is filled with glass beads and epoxy resin to avoid liquid xenon from entering there. This makes it possible to keep the gamma ray detection efficiency flat, independently of the incident location. The total thickness in front of the fiducial volume corresponds to 0.24 radiation length.

Two kinds of complementary beam tests were performed to study the response of the prototype to gamma rays in a wide energy range. One was done by using gamma rays from Laser-Compton Scattering (LCS) and the other was done by using those from pion charge exchange (CEX).

The LCS beam test was carried out at National Institute of Advanced Industrial Science and Technology (AIST) in Japan. Gamma rays with Compton-edge energy of 40 MeV are generated via backward scattering of Nd:YAG pulsed laser photons of 266 nm by 800 MeV electrons stored in a synchrotron. Gamma rays with Compton-edge energy of 20 MeV and 10 MeV are also available by using 532 nm and 1064 nm laser photons respectively. The high intensity gamma beam allows to investigate the position resolution with collimation by using lead bricks with a 2 mm ϕ hole. The details of the beam test are described in a thesis[54].

The CEX beam test was conducted at PSI by using a negative pion beam and a liquid hydrogen target. A negative pion beam stopped in the target interacts with protons and produces neutral pions and neutrons. A neutral pion produced in the target has a momentum of 28 MeV/c in the laboratory frame and decays into two gamma rays. Since this process is a two-body decay, energy and opening angle of the two gamma rays have a correlation. By tagging back-to-back decays in the laboratory frame with collimation, almost monochromatic gamma rays at energy of 54.9 MeV and 83.0 MeV can be obtained.

5.2.1 Optical properties of xenon

Optical properties of liquid xenon used in the gamma ray detector can be extracted from the data. For this purpose, scintillation signal from an alpha source is useful because it can be considered as a point-like source, and the position is known. For example, absorption length, scattering length, refractive index, group velocity of scintillation light could be extracted. Absorption length is strongly depends on impurities.

Rayleigh scattering length

Rayleigh scattering length can be estimated by comparing data observed for alpha source wires. Figure 5.5 shows number of photoelectrons observed by a PMT for alpha events. The PMT is located at $z = 0, y = 3.1$. Reconstructed positions make rings as shown in the figure. This is due to a shadow effect of wires as shown in fig.7.8. A PMT observes more light for events where an alpha particle is emitted to the direction of the PMT than events where the particle is emitted behind the wire. These two cases make two peaks in the distribution of number of photoelectrons. The ratio of the two peaks is sensitive to scattering length. The ratio was compared with simulated data by changing scattering length in the simulation. In the simulation scintillation spectrum with a peak at 175 nm and FWHM of 13 nm was used. Rayleigh scattering length varies inversely with fourth power of the wavelength in the simulation. The best assumption of scattering length in simulation to reproduce an experimental data is 55 cm at 175 nm.

Absorption length

Absorption length of scintillation light in liquid xenon has been estimated by comparing output of each PMTs for alpha source events with MC simulation as a function of the distance between the PMTs and alpha sources. Scintillation light can approach to PMT indirectly because of Rayleigh scattering. Therefore, the actual path length of light is not exactly same as the distance between the source and PMT. The effective distance was estimated for each PMT and alpha source pairs from MC simulation by taking into account Rayleigh scattering. Figure 5.6 shows dependencies of observed charge in typical PMTs on the absorption length. If we do not include Rayleigh scattering effect in the simulation, those dependencies can be expressed as $e^{-d/\lambda_{abs}}$ where d is the distance between the PMT and source. On the other hand in a realistic case with a finite Rayleigh scattering length, such dependence differs from the above function and thus the effective distance needs to be estimated by fitting with an exponential function with d as a free parameter. Using the effective distance estimated in this way as a distance between the PMTs and alpha sources, the absorption length was estimated in MC simulation for various cases and compared with the input values to the simulation as shown in fig.5.7. It can be seen that the input values are well reproduced in the analysis.

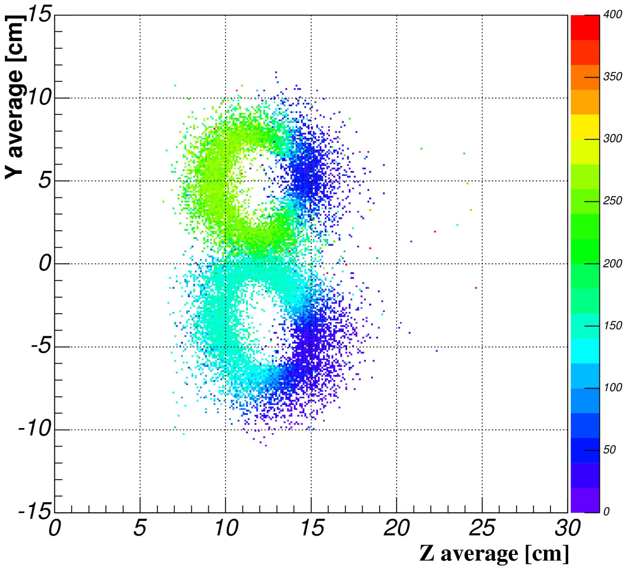

Figure 5.5: Number of photo electrons of a PMT and reconstructed position of alpha wire source. The PMT is located at $z = 0, y = 3.1$. Rings of two wires are shown.

Before applying the method to the real data, PMT output was corrected with Q.E. estimated with alpha data in cold gas xenon. Figure 5.8 shows the ratio of PMT output to MC simulation with infinite absorption length as a function of the effective distance between the source and PMTs. By fitting the distribution with an exponential function, it is found that the absorption length was 233^{+193}_{-72} cm during the measurement in 2003. The absorption corresponds to about 80 ppb of water contamination. In this analysis, scintillation efficiency of xenon (the "W value") was assumed as 17.9 eV[32] and 49.6 eV[55] in liquid and gas respectively, and the scattering length was assumed as 45 cm against 175 nm ultraviolet light.

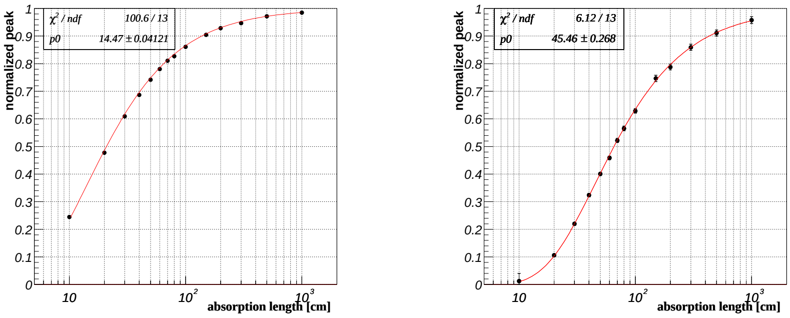

(a) (b)

Figure 5.6: Expected outputs of PMTs as a function of absorption length for alpha source events located on the bottom face of the large prototype. Two PMTs, (a) and (b), are located at different distances from the source. The effective distance was estimated by fitting the shape with exponential functions. True and effective distances are 14.2 cm and 14.5 cm for (a), 40.8 cm and 45.5 cm for (b). respectively.

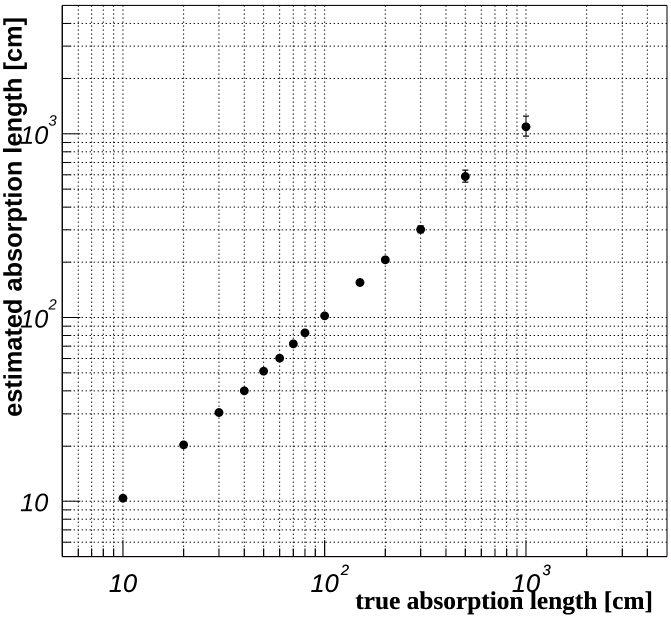

Figure 5.7: True absorption length (input value to MC) and estimated one in MC simulation.

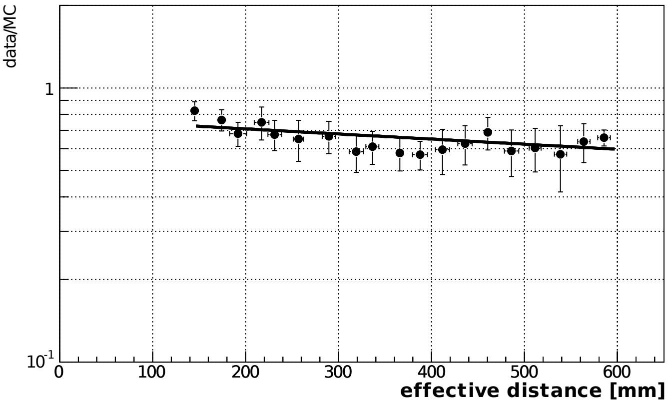

Figure 5.8: Ratio of PMT output in real data to MC simulation with an infinite absorption length as a function of the effective distance.

5.2.2 Purification

Gas phase purification

Figure 5.9 shows the xenon transfer lines of the prototype. When xenon is liquefied into the cryostat of the detector, gas xenon is transferred from a tank via a purifier. Hence, liquid xenon in the detector must be purified. However, the xenon may not be completely pure due to out-gas from materials inside the cryostat or cryostat itself. In the cryostat, some materials, such as G10 or Acrylic plates, which can absorb water vapor and slowly release it later, are used. In many other applications, out-gas attached on materials can be removed by heating up them during evacuation. On the other hand, the large prototype detector has PMTs inside and it is not possible to bake it with high temperature. As a result, a strong light attenuation due to impurities was observed when the first beam test was conducted.

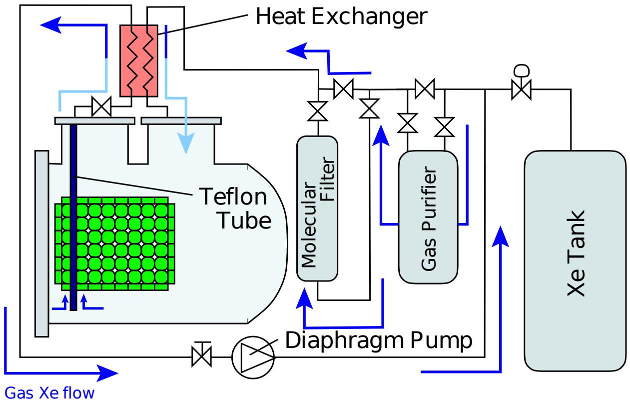

Figure 5.9: Liquid xenon line.

In order to make xenon transparent, it is necessary not only to purify xenon, but also to clean materials inside the cryostat. After the cryostat is filled with liquid xenon, a part of it is extracted by a diaphragm pump, and the xenon is purified, then liquefied into the cryostat. In this process, impurities came out from materials in the cryostat can be removed by a purifier continuously. Figure 5.10 shows variations of observed amount of light during purification[46]. It is clearly seen that the amount of light was increased by the purification, and increase of light observed by far PMTs from a light source is larger than near PMTs, that implies the increase is due to a improvement of transparency. A flat period from 700 to 900 hours is because purification was not done. A change after 1000 hours is due to a instability of electronics. After repeating liquefaction and circulation several times, absorption length stayed long even when purification is stopped because impurities on materials were almost removed.

Liquid phase purification

Another type of purifier was tested by using the prototype[48] in order to make purification faster. Limitations of purification speed was conductance of xenon

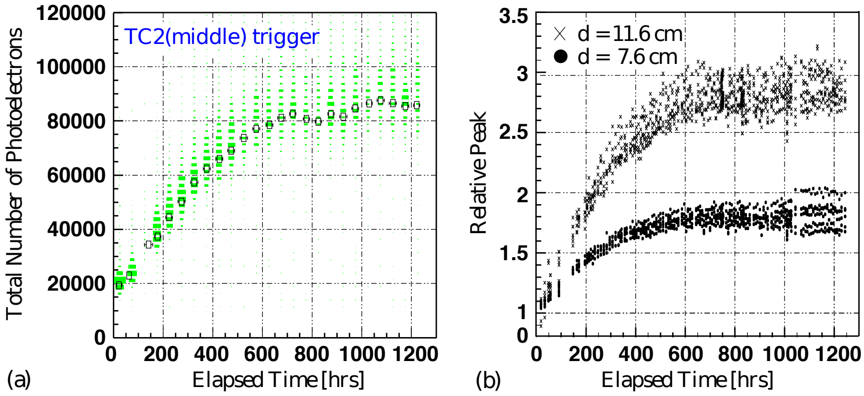

Figure 5.10: Variations of amount of light during purification. (a) Landau peak of sum of all the PMTs in cosmic ray events triggered by plastic scintillation counters locate above and below the detector. (b) Relative output of each PMTs in alpha source events. Different markers are used for different distance between a PMT and a alpha source.

transfer line and cooling power to re-condensate xenon. To decrease these effects, the new method adopts circulating xenon in liquid phase. In this way, mass flow in the transfer line becomes faster, and evaporation and re-condensation of xenon are not needed. A centrifugal pump was adopted to circulate xenon. The pump can make a flow of 100 l/h with differential pressure of 0.2 MPa. A motor is put outside of the cryostat and the pump does work for cold liquid without contaminating it. Since it was found that the main contribution of absorption is water, molecular sieves (MS13A) was chosen as the filter. The cartridge used for the test with the prototype can absorb more than 24 g of water. It can be regenerated by heating it with evacuating the cryostat. Figure 5.11 shows the slope of corresponding lines to fig.5.8 during the test of liquid phase purification. For the test, a small amount of water was put in the xenon. Hatched part in this plot shows periods when the purification was operated. The staring point corresponds to 250 ppb of water contamination. It was decreased down to 40 ppb in 5 hours operation.

In the case of the final detector, the purification system was put in a smaller separated cryostat, and it was connected with the detector by vacuum insulated pipes. The operation was successful also for the final detector.

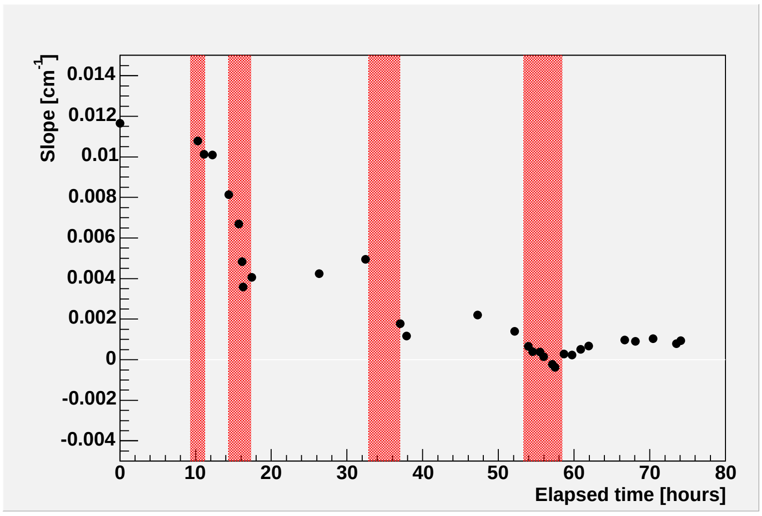

Figure 5.11: Slope of data v.s. MC of alpha events as a function of time during liquid phase purification.

5.2.3 CEX beam test

CEX beam tests were done twice at PSI in 2003 and 2004. In 2003, old type PMTs(R6041Q) were used. In 2004, front half of PMTs were replaced by new type of PMTs(R9288) which have three times higher Q.E. than the old type.

Setup

Pion beam momentum of 110 MeV/c was adopted to get a maximum TOF separation of about 8 nsec between electrons and π^-s, and μ^-s and π^-s, that is, so called "magic momentum". For reducing electron contamination in the beam further, we employed a carbon degrader of 4 mm thickness placed, resulting in a π^- beam momentum of 107 MeV/c. Beam line elements were tuned so that those π^-s can be transported to the exit of the beam line where a 190 μm Mylar window ends the beam line vacuum. A plastic scintillator(S1) is located just after the Mylar window to define the beam and determine the start timing for electronics. Taking the time difference between the S1 and the RF timing of the cyclotron accelerator, π^- could be clearly separated from electrons and μ^-s. Although electron contamination in the beam even at this level did not cause any serious background, we could further reduce it by requiring larger pulse on the S1 counter than certain threshold. π^-s were degraded by carbon plates after leaving the S1 counter so that they could be stopped effectively at the center of the hydrogen target. Thickness and location of the degrader was optimized to be 26 mm in order to maximize the π^- stopping. Schematic views of the liquid-hydrogen target chamber and its cell are shown in fig.5.12. The dimension of the target cell is approximately 40 mm in diameter and 100 mm in length, whose window is made of thin aluminum. The cell is supported by a cylindrical shell attached to the cold head. Hydrogen is liquefied and maintained in a stable state with a GM-type cryo-cooler, by heat conduction through the shell, equipped at the end of the target chamber, and a heater whose power is controlled continuously by monitoring the cell temperature. During data acquisition, the target stayed quite stable even without paying any special attention.

The beam profiles were obtained by using a plastic-scintillation counter mounted on a beam profile scanner placed at the position of the target cell. Beam spread is estimated to be 12 mm in sigma both in vertical and horizontal directions, which means that more than 80 % of beam could enter the cell. By integrating the profiles in two dimensionally we estimated the maximum beam intensity to be 2.6 MHz with 1.8 mA primary proton current. Low intensity π^- beam data was used to minimize the effect of neutron background, which can reduce Q.E. of PMTs by too high PMT current. Lead collimators were located both in front of the xenon and NaI detectors to select back-to-back gamma rays with less ambiguity coming from position reconstruction.

As introduced in the previous section, we employed an NaI array for tagging gamma rays from π^0 decays opposite the xenon detector large prototype. Details of the modular detector are described in ref.[56]. Signals from the detector was utilized for triggering π^0 events and in the offline analysis they were applied for event selections. Performance of the detector will be described in the later section. For the purpose of estimating the timing resolution of the xenon detector, two different types of detectors were used in 2003 and 2004. In

2003, we prepared a scintillation counter, which consists of two sets of timing counters, each of which consists of a plastic scintillator ($5\times5\times1$ cm^3) viewed by two PMTs (Hamamatsu R5505) at both ends through light guides. Lead plates in total 6 mm thick were placed in front of the timing counters for converting gamma rays. These two counters were set before the NaI detector only when studying the timing resolution in order not to deteriorate the energy resolution of the NaI detector. In 2004, an LYSO($\mathrm{Lu}_{(2-x)}\mathrm{Y_xSiO_5}$:Ce) crystal with two PMTs attached at the both ends was used.

Purification of liquid xenon was performed in prior to the beam test to obtain longer absorption length.

Timing information was taken from all PMTs by discriminators and TDCs. One FASTBUS TDC (LeCroy 1875A), four CAMAC TDCs (Phillips 7186H) and four VME TDCs (CAEN V775) were implemented for this purpose. For splitting the PMT signal MACRO fan-out splitters that had been used in series of studies were prepared for all channels. For measuring pulse amplitude of the PMTs, FASTBUS ADCs (CERN CIA) [57] were used. A new function of the ADC module was invoked from this test to measure small signals more precisely. Analog-to-digital conversion is done for raw input and in addition for 8-times amplified input simultaneously in the module, thus enabling us to measure the amplitude with a 15-bit resolution. Furthermore for central 16PMTs on the front face, the signal amplitudes were also measured with 10-20 dB attenuation by utilizing another output from the splitters. This is for treating large amplitude signals that could be observed when gamma ray interaction occurred near the front-face PMTs.

Gain of the PMTs in xenon detector was adjusted to be 5×10^6 in 2003. In 2004, two gain settings, "normal gain" (5×10^5 for R9288 and 1×10^6 for R6041Q) and "high gain" (1×10^6 for R9288 and 2×10^7 for R6041Q), were used for comparison. Lower gain was used in 2004 because it was expected the gain would be optimum for the final setup of MEG electronics by using DRS. Eventually, we decided to set gain to be 2×10^6 in the MEG experiment, therefore "high" gain mode in the beam test is closer to the setting of the final experiment.

NaI detector

The NaI detector is an 8×8 array of optically isolated NaI(Tl) scintillator bars encased in an air-tight container. The dimension of each bar is $63.5 \times 63.5 \times 406$ mm^3. The lateral and rear walls of this box are 19 mm thick aluminum plates. The front wall is made of a 0.5 mm thick steel sheet, a thermal isolation of 20 mm of Styrofoam glued to a 2 mm aluminum foil. In the back plate, 64 PMTs (Philips PM2202) are connected to NaI through 64 Pyrex windows with Plexiglas light guides (60 mm). In order to avoid thermal drift due to the heating inside the shielding, the last four dynodes are individually powered by a common active voltage divider, located outside the shielding. The anode pulses are sent to the "signal processor" through tri-axial cables. These signals are shortened to less than 600 nsec, and the active stabilizer maintains the output base line close to zero. Three outputs are obtained from the signal processor. One is the output through 360 nsec delay and an attenuator for ADC, second one is a 50 nsec FWHM fast pulse for TDC, and the last one is a signal to the trigger device. To avoid triggering on low energy multi-particle events, the trigger device selects the events whose energy sum in each of the 49 groups of quad NaIs are above threshold, “quad trigger”. To get back-to-back gamma events from π^0 decay around the detector center, additional trigger signal was prepared, which is an energy sum of center four NaIs, “center trigger”. Signals for the ADC and trigger were sent from the signal processor in the area to the electronics hat through 64 nsec delay cables. High voltage value for each PMT was adjusted by using cosmic ray spectra. Pedestal subtraction and gain correction were done in the offline analysis. As described in the previous section, an excellent energy resolution is not required for the tagging side counter, NaI detector, but only a reasonable position resolution to define the opening angle which directly corresponds to the energy resolution for gamma rays from π^0 decays.

High voltage values of 64 PMTs were adjusted by using the MIP peak by cosmic rays. Eventually, the gain variation over all NaIs was reduced down to about 3.5 %, with high voltage settings ranging from -1300 to -1700 V. Figure 5.14 shows the energy spectrum of tagging side during CEX beam test. Energy measured by NaI and LYSO detector are summed in the analysis. The tagging detector has a good enough resolution as shown in fig.5.15.

Prototype detector analysis

In this section, analysis of xenon detector is discussed by using mainly 2004 CEX test data. The comparison of 2003 and 2004 data will be done later.

Position Reconstruction In this section the position reconstruction algorithm is described and its performance is presented by using MC simulation data. This is because, contrary to the LCS beam test, the counting rate of gamma ray injection to the detector was not enough to study the position resolution by placing a collimator with a diameter much smaller than the resolution. Incident position of gamma rays to the xenon detector was reconstructed with a local-weighted method. In this method the following procedure was taken:

1. Make a 2-dimensional histogram with 6×6 bins. Each bin corresponds to a PMT on the front face.
2. Fill the histograms with output of PMTs. Define the starting point $(x_{\rm rec}, y_{\rm rec})$ for the following iteration procedure as the mean of the distribution.
3. Re-bin the histogram so that the center of each axis becomes $(x_{\rm rec}, y_{\rm rec})$ without changing the bin width.
4. Define the next point with taking average in a limited range. The range is determined as $|x - x_{\rm rec}| < f/s_x$ and $|y - y_{\rm rec}| < f/s_y$, where s_x and s_y mean the standard deviations of the histogram along x and y directions. The selection of the range is done to decrease effects from energy deposits other than the first interaction. The factor f should be optimized as a function of the incident position. But in this analysis, a constant value (40) was used just for simplicity.
5. Iterate the 3 and 4 processes till $(x_{\rm rec}, y_{\rm rec})$ converges.

Figure 5.16 shows a 2-dimensional distribution of differences between true and reconstructed positions for MC simulation data. The data was generated under the conditions of (i) $E_\gamma \sim 54.9$ MeV, (ii) first conversion in the fiducial volume. The position reconstruction resolution is estimated to be about 6 mm in σ by fitting the distribution with a Gaussian function including only one parameter, $r \equiv \sqrt{(x-x_0)^2+(y-y_0)^2}$. In fig.5.17 a comparison between (a) local-weighted method and (b) simple-average method is shown. It is clear that the local-weighted method is superior to the simple average method in particular for deep events. In the simple-average method the reconstructed position is tend to be pulled to the centers of PMTs while in the local-weighted method not. Thus we can conclude that the reconstruction of incident gamma ray positions can be done in a less biased way by employing the local-weighted method.

depth reconstruction When the first conversion of a gamma ray occurs close to the front face, the distribution of scintillation light detected on the front face is narrow, and it becomes broader as the first conversion point moves deeper. The number of PMTs on the front face which occupy a half of $Q_{\mathrm{f}ront}$ ($N_{\mathrm{f}pmt}(0.5)$)[1] was used as a measure for the first conversion depth. Here PMT output is summed in the order of the distance from the reconstructed incident position until the sum exceeds a half of $Q_{\mathrm{f}ront}$. The relation can be expressed in the following equation:

$$\frac{\sum_{i=0}^{N_{\mathrm{f}pmt}(0.5)} Q_i}{Q_{\mathrm{f}ront}} = 0.5 \tag{5.1}$$

Examples are shown in fig.5.18 for two typical cases, shallow conversion (4.6 cm depth) and deep conversion (13.8 cm depth). The sum of PMT output in the shadowed region is equal to a half of $Q_{\mathrm{f}ront}$. The sum is taken with a weight proportional to the are in the circle, so $N_{\mathrm{f}pmt}(0.5)$ is not an integer necessarily. It can be seen that the area of the shadowed region is smaller in case of shallow events and it becomes larger for deeper events.

In fig.5.20 relations between the $N_{\mathrm{f}pmt}(0.5)$ and actual first conversion depth for MC simulation data are shown for different impinging points of gamma rays whose notations are defined in fig.5.19. By fitting the relation with a second-order polynomial function, for example for the case of (a), the depth can be reconstructed as

$$D_{\mathrm{rec}} = 1.38201 + 0.246552 \times N_{\mathrm{f}pmt}(0.5) + 0.0768057 \times N_{\mathrm{f}pmt}(0.5)^2$$

Figure 5.21 (a) shows a relation between the reconstructed depth in this way and true first conversion depth. From this the depth resolution for MC simulation data is estimated to be 8.2 mm for 54.9 MeV gamma rays in the rage of 4 cm $< D_{\mathrm{rec}} <$ 15 cm as shown in fig.5.21 (b). This relation is employed for estimating the depth in real data.

Energy Resolution Energy resolution was evaluated using simple sum of all PMT outputs ($Qsum$) with correction of the dependence on position. Q.E. and gain correction of PMTs are done before computing $Qsum$. In this discussion

---

[1] $Q_{\mathrm{f}ront}$ means a sum of output of PMTs on the front face.

Q.E. includes also collection efficiency. Estimation of Q.E. and gain is discussed in 7.1.1 and 7.1.2 respectively.

$$Q_{sum} = \sum_{i=0}^{238} Q_i/gain \times \frac{\overline{\mathrm{Q}.E.}}{\mathrm{Q}.E._i} \tag{5.2}$$

Figure 5.22 shows measured number of photons in the xenon and the energy at the tagging detector. Tails below the gamma ray peaks from π^0 decays are due to gamma conversions in the lead collimator or vacuum chamber, and to energy leakage from the front face. When we analyze the data of 54.9 MeV and 83.0 MeV gamma rays, a selection was applied for the measured energy with the tagging detector as 70 MeV$< E_{tag} <$ 105 MeV and 35 MeV$< E_{tag} <$ 70 MeV The distributions of the number of photons observed in the xenon detector are presented in fig.5.23. The black histogram is data without cuts and the blue and red ones are for those after 54.9 MeV and 83.0 MeV selections. Figure 5.24 (a) shows a depth dependence of Q_{sum} when gamma rays impinged at the center of the detector. Q_{sum} slightly increases depending on the depth around the middle, and decreases at the end. This is because PMT coverage density is higher in central part than front or back part, and much less at the back side than the other part because PMTs were not installed in the last column of the prototype detector as shown in fig.5.4. For removing this dependence, in this analysis, events with $N_{\mathrm{f}pmt}(0.5) > 12$ were discarded and a correction was applied for the other events with a linear function. The distribution after the correction is shown in fig.5.24 (b).

To estimate the energy resolution, following function was used as a fit function. Figure 5.25 shows a typical histogram of Q_{sum} overlaid with a fit function.

$$F(x) = \begin{cases} Ae^{\frac{-(x-x_0)^2}{2\sigma^2}} & (x > x_0 + t) \\ Ae^{\frac{t}{\sigma^2}(t/2-(x-x_0))} & (x \leq x_0 + t) \end{cases}$$

Energy resolution was evaluated in two ways, by using FWHM and σ of this function. Discussing the resolution using σ is important for estimating background rejection power against $\mu^+ \to \mathrm{e}^+\gamma$ because gamma rays from accidental and prompt background has less energy than those from $\mu^+ \to \mathrm{e}^+\gamma$. In addition σ must improve statistically as the observed number of photoelectrons increases. On the other hand, FWHM needs to be considered to discuss the detector efficiency. Because there is always a non-negligible effect of “leakage” from the front face of the detector, FWHM does not necessarily improve even when the number of photoelectrons increases. Figure 5.26 shows the energy resolutions, expressed in σ and FWHM, as a function of slices of a depth parameter when gamma rays impinged on IP5. As can be seen in the figure, the FWHM improves for deeper events, and stays constant in 4.5-5.0% for the events with $N_{\mathrm{f}pmt}(0.5) > 4$. This can be simply explained by the fact that the leakage effect is negligible for the deeper events compared to the shallow events. σ is also constant around ~1.3% in case $N_{\mathrm{f}pmt}(0.5) > 4$. For shallow events, resolution becomes worse because depth and position resolution becomes worse, and $Qsum$ with after Q.E. correction ($Nsum$) dependence on position is large. An analysis to solve this problem is discussed in a section for final detector’s analysis.

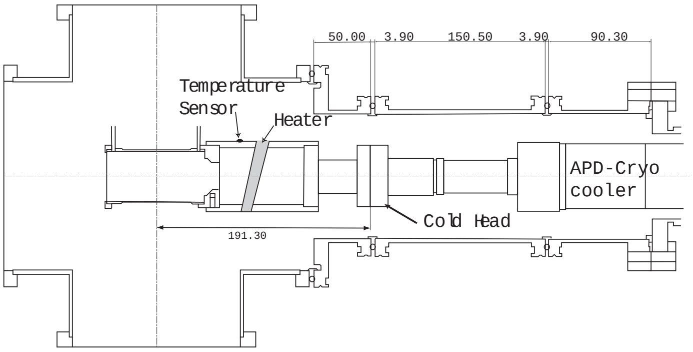

Figure 5.12: A schematic view of the target chamber. The cell sits at the center of three window flanges. A pion beam comes from the left. The liquid xenon and the tagging detectors are locate at the upper and lower direction in the figure respectively.

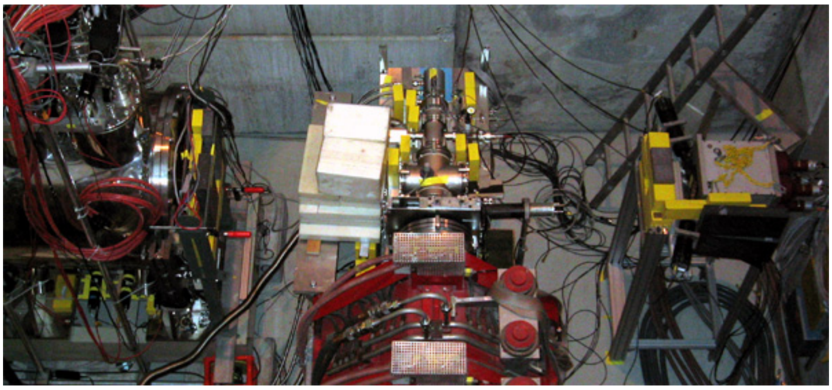

Figure 5.13: Setup in 2004 CEX beam test. The xenon detector, the hydrogen target cell and a tagging detector are seen in the left, center and right in this picture respectively.

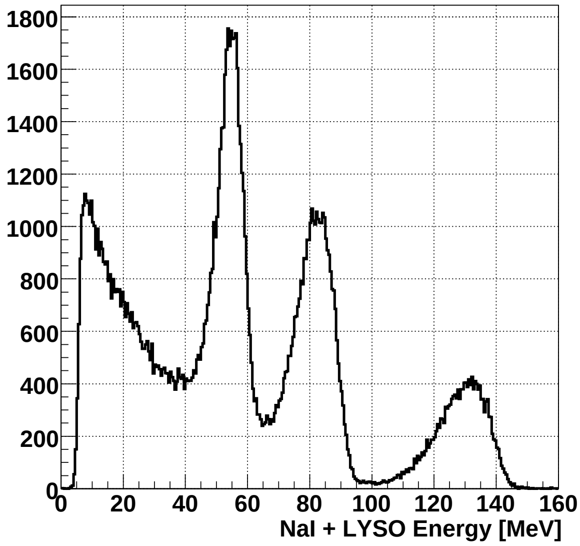

Figure 5.14: Spectrum of gamma rays at tagging side. Two peaks (54.9 and 83.0 MeV) of back-to-back gamma rays from π^0 decays and 129 MeV peak from neutron capture process.

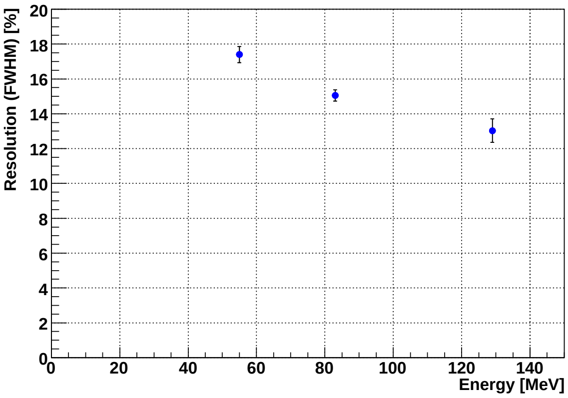

Figure 5.15: Observed energy resolution of NaI and LYSO detector as a function of incident gamma ray energy.

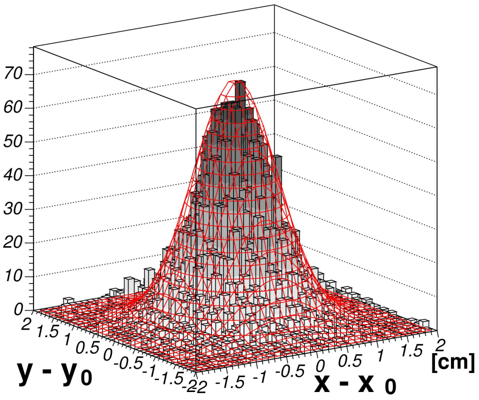

Figure 5.16: Distribution of difference between true and reconstructed positions in simulation.

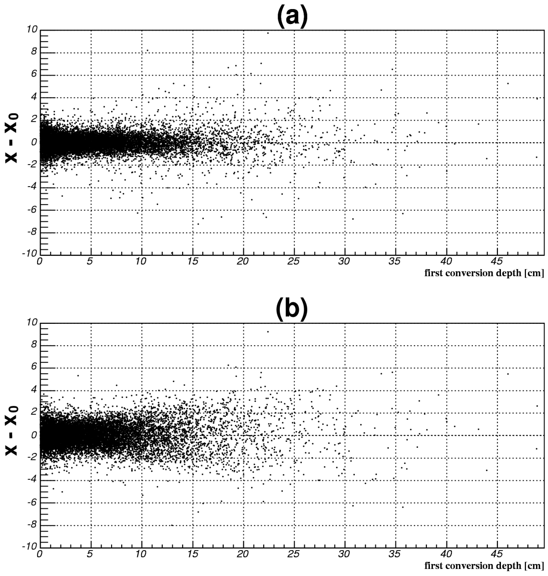

Figure 5.17: Distribution of the residual between reconstructed and true positions as a function of the first conversion depth for MC simulation data. (a) local-weighted method (b) simple-average method. x_0 represents the true incident position.

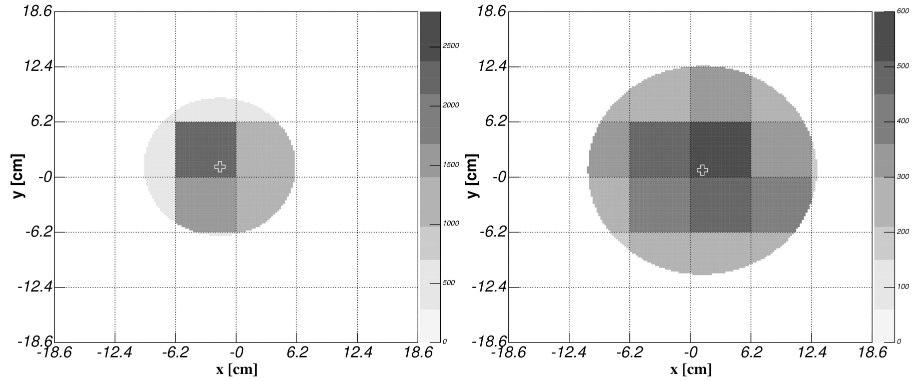

(a) shallow event (4.6 cm)

(b) deep event (13.8 cm)

Figure 5.18: Charge distributions on the front face for shallow and deep events. A sum of PMT outputs in the shadowed region is equal to a half of Q_{front}.

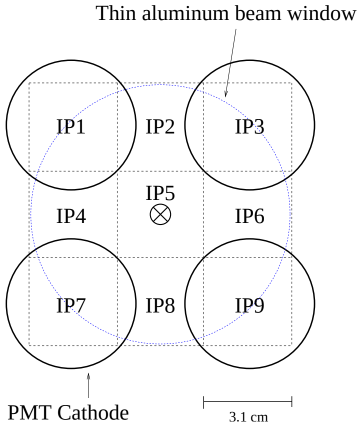

Figure 5.19: Notations of impinging points used in this analysis.

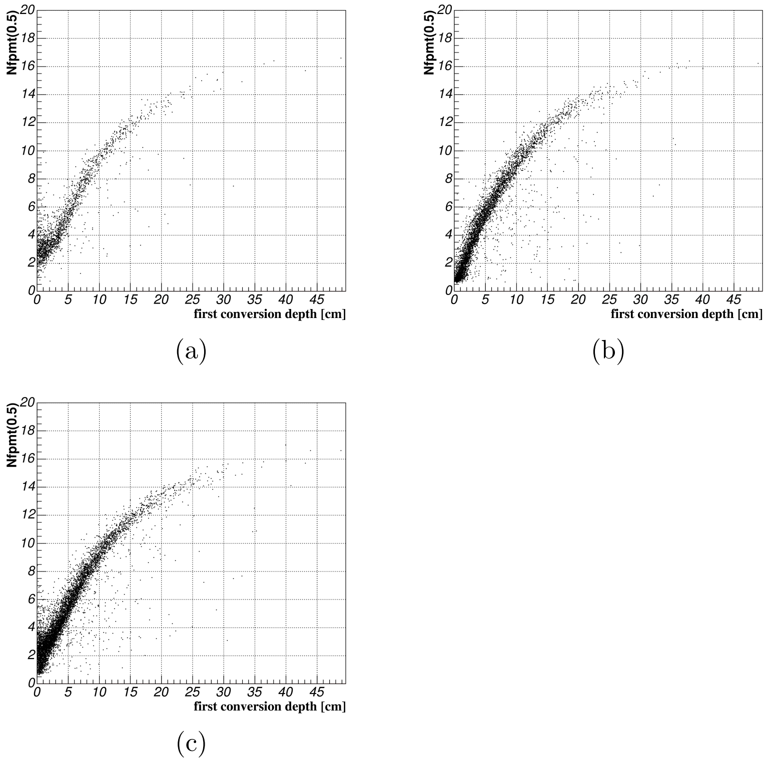

(a)

(b)

(c)

Figure 5.20: Relations between the $N_{\mathrm{f}pmt}(0.5)$ and true conversion point in MC simulation. (a) is for gamma ray impinging at IP5, (b) is for IP 2,4,6, and 8, and (c) is for IP 1,3,7, and 9 as defined in fig.5.19

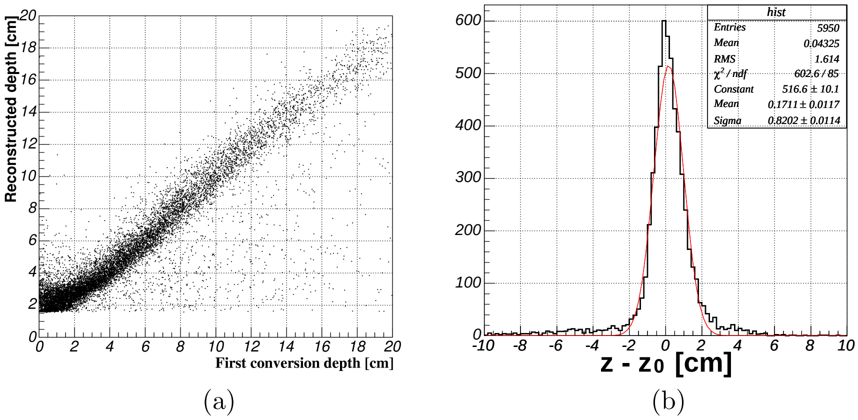

(a)

(b)

Figure 5.21: (a) Scatter plot of reconstructed and true conversion depths. (b) Residual distribution after reconstruction.

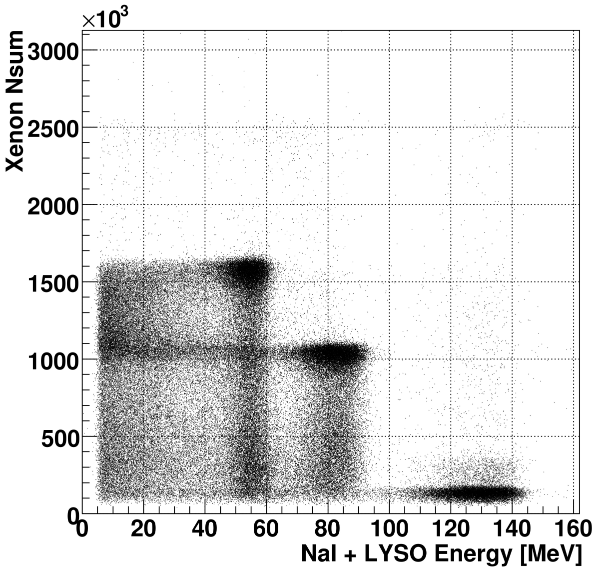

Figure 5.22: Distribution of Q_{sum} vs observed energy with the NaI detector.

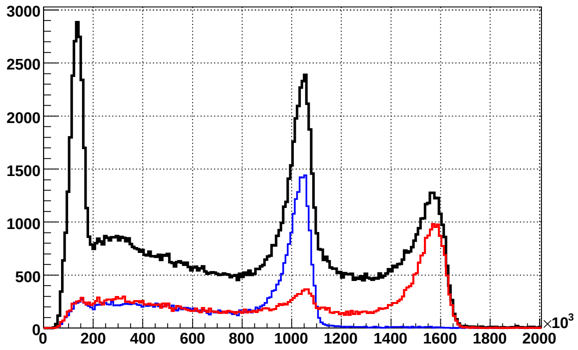

Figure 5.23: Distributions of the number of photoelectrons observed in the xenon detector for three cases. The black histogram is data without cuts and the blue and red ones show the distributions after 54.9 MeV and 83.0 MeV selections on the NaI detector side.

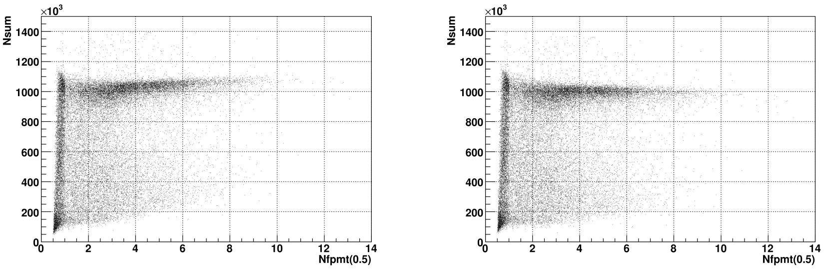

(a) (b)

Figure 5.24: Distributions of Q_{sum} vs depth. (a) before correcting the depth dependence. (b)after correcting the depth dependence with a linear function.

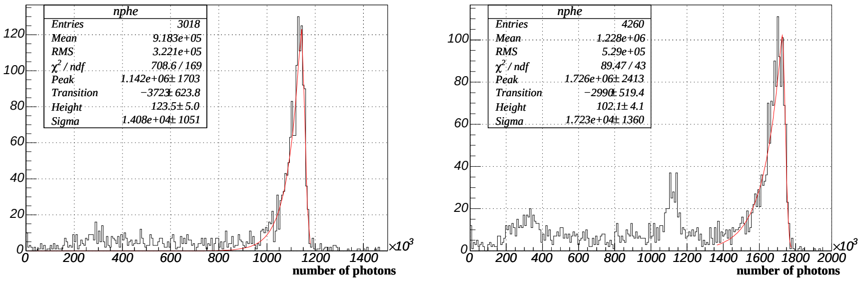

(a) (b)

Figure 5.25: Q_{sum} distribution together with a fit function for (a)54.9 MeV and (b)83.0 MeV gamma ray incident. Sigma of right edge of the peak is 1.2 % and 1.0 % for (a) and (b) respectively.

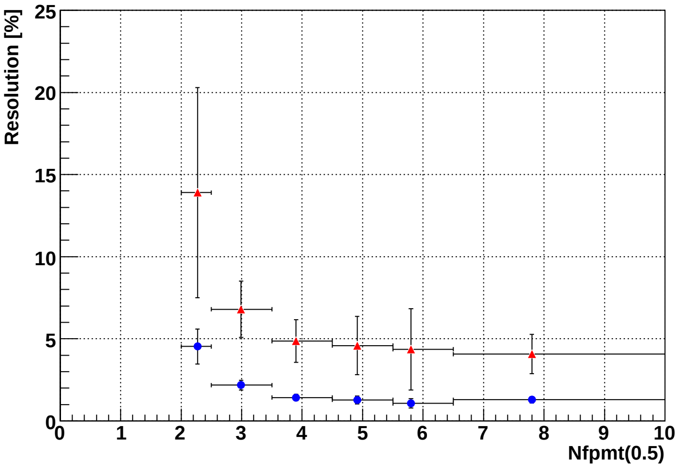

Figure 5.26: Energy resolutions as a function of the depth selection threshold when gamma ray impinged at the center of the detector (IP5).

Timing Resolution

Timing calculation in the large prototype The timing of gamma ray in the large prototype was calculated in a following way.

1. Time walk correction for each PMT.
2. Adjust offsets so that the mean of each PMT timing is set to be 0.
3. Take a weighted average among PMTs those satisfy following requirements.
   - $N_{pe,i} > 50$.
   - $|T_i| < 10$ nsec.

   The weight for each PMT is determined as $\sqrt{Q_i}$ event by event.
4. Correct impinging position and depth dependence.

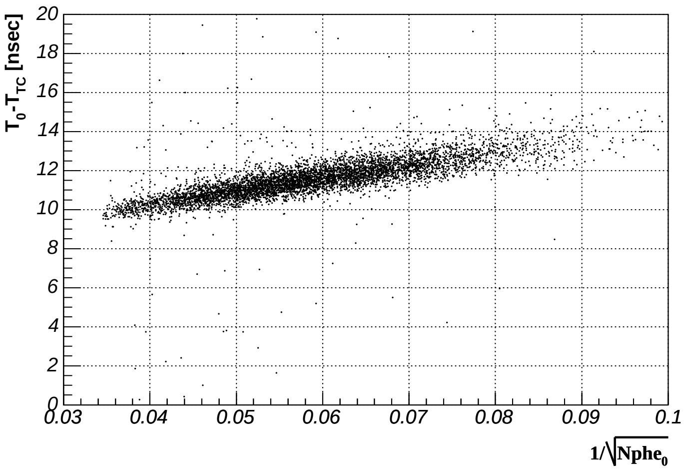

Figure 5.27: An example of time walk correction for a certain PMT. Timing of each PMT was corrected by using a factor proportional to $1/\sqrt{N_{pe,i}}$.

Time walk of each PMT was estimated from a plot like fig.5.27. In the figure time distribution of a PMT relative to the tagging counter is shown as a function of $1/\sqrt{N_{phe}}$, where N_{phe} is number of photoelectrons. Correction factor was obtained by fitting the distribution with a linear function for each PMT.

Timing resolution was estimated for 54.9 MeV and 83.0 MeV gamma rays. The event selection was done by observed energy by the gamma ray detector, and the tagging detector was not used except for a coincidence condition.

Intrinsic timing resolution To estimate the intrinsic timing resolution, "L-R" analysis was performed. In this analysis, PMTs were divided into right and left groups by the center plane of the detector. Timing of both groups were calculated independently. Then the intrinsic timing resolution was estimated from the distribution of $(T_L - T_R)/2$, where T_L and T_R are defined as averaged timing in the left and right groups respectively. Difference of averaged timing between right and left groups is largely dependent on impinging position of gamma rays in x direction. Figure 5.28 shows dependence on reconstructed x. After correcting the dependence on x evaluated by using the simple weighted mean with all PMTs, a depth selection was applied with $N_{\mathrm{f}pmt}(0.5)$. Figure 5.29 shows the time resolution as a function of the depth parameter. The resolution is not affected by depth.

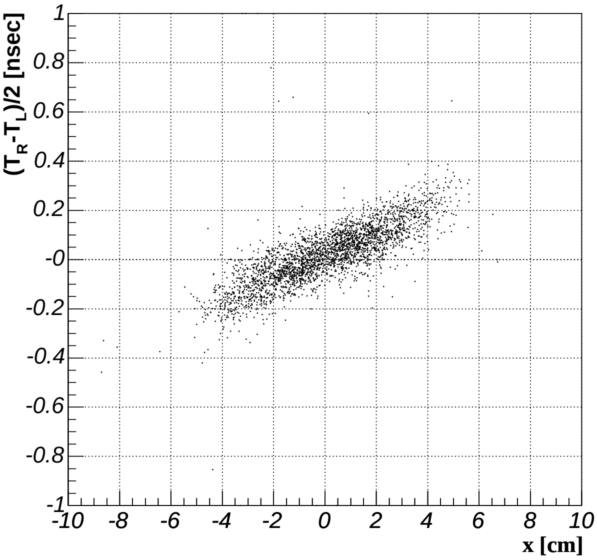

Figure 5.28: x dependence of $(T_L - T_R)/2$.

Practical timing resolution We also performed evaluation of practical timing resolution. In this analysis, time difference between the xenon detector and the tagging detector was used. Note that in this analysis we have to take into account the effect of beam spread, that is the spread of the π^0 production/decay point. The relative timing has dependencies on the first conversion depth, Q_{sum} , and impinging position. The spread includes not only the xenon detector timing resolution but also other fluctuations. Main contributions are from the timing counter resolution and ambiguity of π^0 decay position. The spread of π^0 decay position was estimated by measuring the beam profile on the target. That contribution is calculated to be 58.8 psec in sigma. After subtracting these effects, the timing resolution of the xenon detector was evaluated. The result is summarized in fig.5.30 as a function of the depth selection parameter.

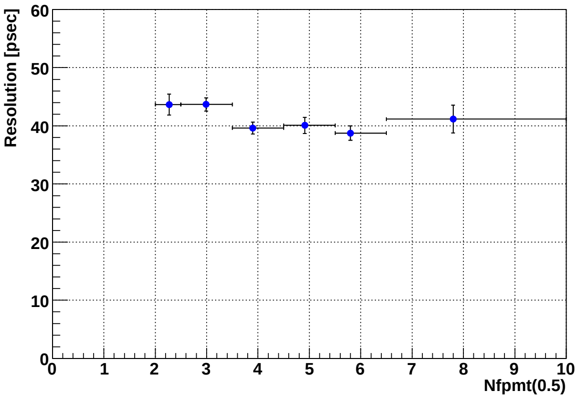

Figure 5.29: Intrinsic time resolution and the depth selection. Resolution without slicing by depth is 43 psec.

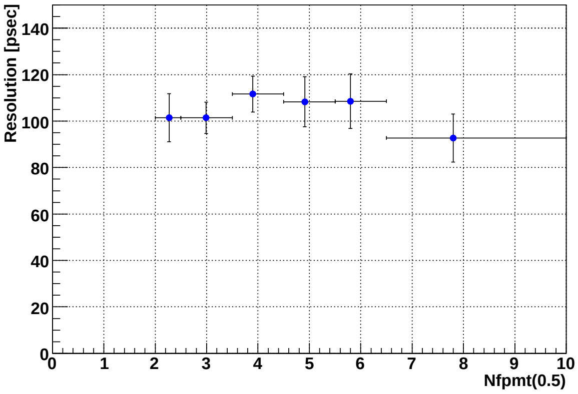

Figure 5.30: Practical time resolution as a function of the depth selection parameter. These numbers include the time resolution of the tagging detector(64 psec) and decay point fluctuation(58.8 psec). Resolution without slicing by depth is 53 psec after contributions of the tagging counter resolution and the decay point fluctuation are subtracted.

Comparison of 2003 and 2004 runs

In this chapter resolutions in 2004 was shown. In this section, comparison of 2003 and 2004 data is discussed. Between 2003 and 2004 beam test, front half of PMTs were replaced to new type PMTs. The structure of two types of PMTs are basically same except for photo-cathode. The old type PMT has a RbCsSb+Mn photo-cathode which was selected for low temperature operation. However, it was found that the sensitivity for ultra violet light was not so high. And control of gain is not easy. Therefore, KCsSb is used for the new type. KCsSb have higher resistance than RbCsSb. To reduce the resistance, aluminum strips are attached on photo-cathode. By the modification, Q.E. and gain control were improved. FWHM of the peaks do not change from 2003 since the lower tail is due to leakage of gamma rays and interaction before the active volume. However, the sigma of right edge of the peak was improved due to larger number of photo-electrons than 2003. Time resolution was much improved in 2004, because number of PMTs with more photo-electrons than a threshold to use for averaging time was increased due to improvement of Q.E..

The comparison is summarized in table 5.1. The difference of energy resolutions due to the difference of Q.E. is reasonable from simulation (1.5 % and 1.0 % with 2003 and 2004 Q.E. settings respectively.)

	2003	2004
Energy resolution (sigma of right edge) for 54.9 MeV peak	1.6 %	1.2 %
Energy resolution (sigma of right edge) for 83.0 MeV peak	1.2 %	1.0 %
Intrinsic time resolution for 54.9 MeV peak	73 psec	43 psec
Intrinsic time resolution for 83.0 MeV peak	59 psec	36 psec
Time resolution for 54.9 MeV peak	102 psec	53 psec

Table 5.1: Comparison of resolutions in 2003 and 2004. Resolutions are written in σ.

5.3 Summary of prototypes

During the prototype tests, we have learned several technical things to operate liquid xenon detector stable. The large prototype was the largest liquid xenon detector ever made at that time. Those experiences help a lot for designing and constructing the final gamma ray detector for MEG. Newly developed refrigerators and PMTs eventually worked fine after modifications. Response of liquid xenon scintillation detector was studied for low energy up to 4.4 MeV by using the small prototype and for energy around $\mu^+ \to \mathrm{e}^+\gamma$ signal or even higher by using the large prototype.

For 54.9 MeV gamma rays, energy and time resolutions were estimated to be 1.2 % and 53 psec respectively by CEX beam test. Energy and position resolutions were measured in LCS beam test to be 1.5 % and 4.3 mm for 40 MeV gamma rays respectively[54]. Figure 5.31 shows energy resolutions as a function of energy of gamma rays.

The resolutions of the large prototype is compared with the requirement of the MEG experiment in table 5.2. The angular resolution is slightly worse than

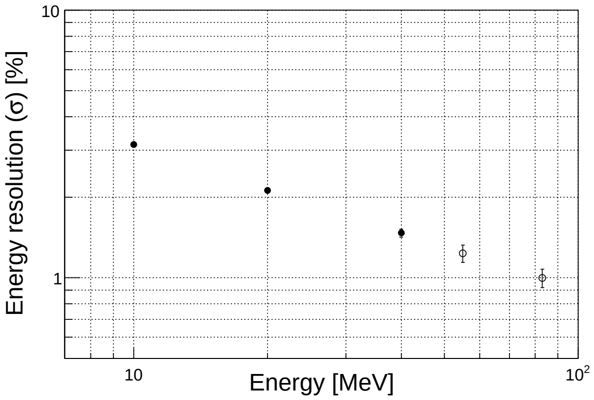

Figure 5.31: Energy resolutions as a function of energies. Black points are result of the LCS beam test and white ones are from the CEX beam test.

the requirement, and the energy and the time resolutions are better. The rate of the accidental background, which is the dominating background, is approximately proportional to $(\Delta E_\gamma)^2 \cdot \Delta E_{e^+} \cdot (\Delta\theta_{\gamma e^+})^2 \cdot \Delta T_{\gamma e^+}$ [58]. By combining three resolutions, the performance of the large prototype satisfies the requirement.

	MEG goal	Large prototype
ΔE_γ [%]	4.5∼5.0	4.4
ΔE_{e^+} [%]	0.8	-
$\Delta\theta_{\gamma e^+}$ [mrad]	12.4∼16.9	18.8(14.9)
$\Delta T_{\gamma e^+}$ [nsec]	0.18	0.16(0.12)
Acceptance × Efficiency [%]	>1.6	-
Muon stopping rate (10^8)	0.3(DC)	-
Running time [weeks]	100	-
Single event sensitivity(10^{-13})	0.5	-
90 % C.L. limit(10^{-13})	1.7	-

Table 5.2: Comparison of MEG goal(table 1.3) and the results of the large prototype. Resolutions are written in FWHM. ΔE_γ of the large prototype is FWHM of fitting function of fig.5.25-a. For $\Delta\theta_{\gamma e^+}$ and $\Delta T_{\gamma e^+}$, requirements for the positron detector (10.5 mrad and 100 psec) are included respectively. For those resolutions, contributions of the gamma ray detector are written in parentheses.

Chapter 6

MEG run 2007

An engineering run was carried out from Autumn to Winter in 2007. It was the first beam test with the final gamma ray detector. The main purposes of the run was investigating the performance of sub-detectors and preparing the trigger for physics runs. Finally, all the sub-detectors worked, and the MEG trigger was prepared. Data for physics analysis was taken for a couple of days. In this chapter, conditions of acquired data in MEG run 2007 are summarized.

6.1 Preparation of gamma ray detector

Before starting liquefaction of xenon, the inner and outer vessels were evacuated independently. The final vacuum level of the inner vessel was 6.9×10^{-3} Pa. Vacuum leaks between the inner vessel and the air was checked by using a helium leak detector, and all leaks were fixed. Leaks between the inner and the outer vessel were checked by using residual gas analysis (RGA) of the outer vessel with filling inner vessel with xenon gas. When we used a recycled gasket as a reference, a clear peak of xenon was seen in the RGA result, which corresponds to 10^{-4} mbar·l/sec. On the other hand, there was not the peak when we used a new gasket. Very small leaks by pin holes of the cryostat were searched by nondestructive inspection with eddy current. Pin holes were fixed by additional welding.

Transfer of liquid xenon from the liquid storage tank to the detector was started on October, 21st and it was finished in three days. In total, 865 litters of liquid xenon was transferred to the detector in a speed of about 10 litters per hour.

H.V. for PMTs were adjusted to set PMT gain to be about 1.5×10^{6}. Typical H.V. was 810 V. Gains were measured in almost every day with a method discussed in 7.1.1. The target gain was determined to be as high as possible for better S/N ratio and time resolution, but not to exceed splitter input voltage limit for typical events. The limitation is the protection clipping of 2.5 V at the input of the splitter. Waveforms were attenuated by factor 3 at the input of DRS so that the pulse height is in the dynamic range of DRS for most of events.

During the physics and calibration data acquisition in 2007, there were 17 dead PMT channels out of 846. Two of them were in the inner face. Those were due to short of the base circuit of PMT through cable bands made of aluminum, or bad soldering of base circuit broken in a low temperature. After the data acquisition in 2007, aluminum cable bands were replaced by cable ties made of Nylon. PMTs with a bad base circuit were replaced with new ones.

Purification of the xenon was done for 205 hours by using the liquid phase purifier described in 3.2.3. The absorption length was monitored by using analysis discussed in 5.2.1. Initial absorption length was 60 cm and it stayed longer than 3 m after the purification. During the purification light yield was increased by 1.6 times, and saturated after 180 hours of purification.

6.2 Cockcroft-Walton

The Cockcroft-Walton (C.W.) accelerator was used mainly with LiF target to monitor the performance of the gamma ray detector by using 17.6 MeV peak. For this purpose, PMTs located around the center of the inner face was used for trigger. Such data was taken typically once per 3 days. Data in the full acceptance was also taken to study the dependence of energy scale on positions. A boron target was also used to know the time difference between the gamma ray detector and the positron timing counters by using a pair of two gamma rays from a nuclear reaction. C.W. data is used in analysis in chapter 7 for energy scale calibration.

6.3 Pion charge exchange

A similar beam test to the large prototype test by using gamma rays from pion charge exchange process was conducted for four days. The purpose was to check the performance of the detector and to demonstrate a calibration which will be done in 2008 and later. In this beam test, events in limited region (2×3 PMT region) were selected by trigger. In 2008, it is planed to scan whole the inner face.

A tagging detector for CEX run consists of nine NaI crystals($62.5 \times 62.5 \times 305$ mm), two plastic counters($60 \times 60 \times 7$ mm) and a lead plate($60 \times 60 \times 6$ mm) to convert gamma rays. The lead converter can be removed when better energy resolution is needed for the tagging side. In fig.6.1-a, the lead converter is not present. When it is used, it is put in front of plastic scintillators.

An requirement of the tagging detector in addition to prototype test is that the detector needs to work in a magnetic field. To fulfill the requirement, avalanche photo-diodes (APD) were used instead of PMTs. To gain enough amount of light, two APDs were attached to each crystal as shown in fig.6.1-b. For the plastic scintillation counters for time measurement, 1 inch fine-mesh PMTs were used.

The tagging detector is mounted on a movable stage which allows to move the detector to r and ϕ direction, and rotate the detector so that the detector can be put at a back-to-back position to a triggering region of the gamma ray detector.

Resolutions of the gamma ray detector are evaluated from CEX data. The analysis is discussed in chapter 7.

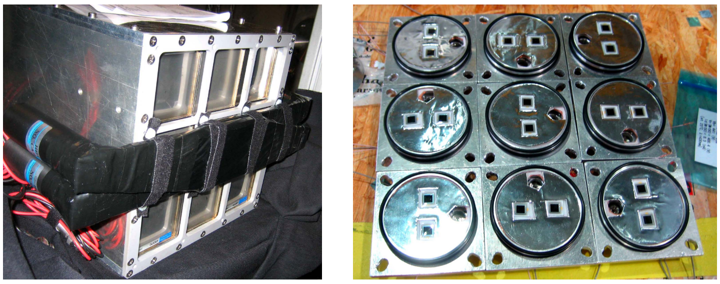

Figure 6.1: Pictures of tagging detector for CEX test. (a) NaI crystals and plastic scintillation counters. (b) APDs to be attached on the back face of NaI crystals.

6.4 Michel decay

Michel decay data was taken by using the positron timing counter or the drift chambers for triggering. This data was used to study the performance of the positron spectrometer and to make probability density functions (p.d.f.) for physics analysis.

6.5 Radiative muon decay

A large amount of radiative muon decay data was taken mainly for developing the MEG trigger. The condition of RD trigger is almost same with the MEG trigger, except that RD trigger does not require any condition of opening angle. The trigger condition was

- $E_\gamma > 40$ MeV
- $|T_{e\gamma}| < 20$ nsec
- At least two timing counter hits

, where E_γ is energy of a gamma ray and $T_{e\gamma}$ is time difference between a gamma ray and a positron.

6.6 MEG trigger data

MEG trigger was prepared by adding a requirement of direction matching of a gamma ray and a positron to the RD trigger. For direction matching, position of the PMT of the gamma ray detector with maximum charge and reconstructed position of a positron hit by using charge asymmetry of *phi*-measuring timing counter were used. Direction matching table was made based on MC simulation. triggers listed in table 6.1 were mixed with proper pre-scaling.

Condition of MEG trigger was,

- $E_\gamma > 40$ MeV
- $|T_{e\gamma}| < 10$ nsec

- At least two timing counter hits
- Direction matching of a gamma ray and a positron.

Name	Pre-scaling	Difference from MEG
MEG	1	
MEG Low Q	2	$E_\gamma > 35$ MeV
MEG Wide Angle	5	Only upstream/downstream correlation
MEG Wide Time	1	$\lvert T_{e\gamma}\rvert < 20$ nsec
RD Narrow Time	15	No check of angle. $\lvert T_{e\gamma}\rvert < 20$ nsec
RD Wide Time	30	No check angle. $\lvert T_{e\gamma}\rvert < 40$ nsec

Table 6.1: Triggers used for 2007 physics data taking

Event rate of MEG trigger was 4 Hz as it had been expected. Live time of DAQ system was 63 % of real time. In year 2007, 73 % of events were triggered by other triggers than MEG, and the higher rate made dead time of the system. In the case of data acquisition in physics runs in 2008 and later, we will use higher pre-scaling factors for trigger types other than MEG, so most of events will be triggered by MEG trigger. Therefore dead time will be smaller than the case of 2007.

In chapter 8, analysis result of 170 k MEG trigger events collected in 23.5 hours is shown.

Chapter 7

Analysis

In this chapter, performance of the gamma ray detector is discussed by using data in 2007. We discuss about calibration of PMTs including gain, Q.E. and time offset measurement. After that, event reconstruction is described and the performance is evaluated by using CEX data. Finally, event type identification to reduce background events is described. The measured resolutions are not as good as requirements mainly due to lower scintillation yield than expected due to contamination of liquid xenon. In following sections, these are discussed quantitatively.

7.1 Calibration of PMT

In the MEG experiment, quantum efficiency of photo cathode(Q.E.) and PMT gain are measured separately. Q.E. is supposed to be stable for long term, therefore it is measured few times. On the other hand, it takes time to stabilize gain when temperature or H.V. is changed. So gain calibration is done frequently during experiment. Time offset between PMTs due to variations of path length from PMT to readout electronics is measured from time difference in LED runs with taking into account distance between a LED and a PMT.

7.1.1 PMT Gain

Gains of PMTs are estimated by using LEDs installed in the detector. Figure 7.1 shows positions of LEDs on the lateral faces. During the measurement, several LEDs are flashed so that all the PMTs are illuminated. As it is shown fig.7.2-a, data is taken by changing the intensity of LEDs. Number of photo-electrons can be calculated from the width of distribution at each step from Poisson statistics. Figure 7.2-b shows a relation between mean and σ^2 of Gaussian distributions. PMT gain is proportional to the slope of the fitting function in this figure. Contribution of noise independent of LED intensity is included in intersection of the fitting, and it does not affect estimation of gains.

However, when a noise depends on intensity of LEDs, it affects estimation. To reduce the effect, a new technique was developed. Principle of the modification is increasing voltage for LED, and attenuate light by covering LEDs by filters. In 2007, LEDs were covered by thin Teflon sheets. When this technique

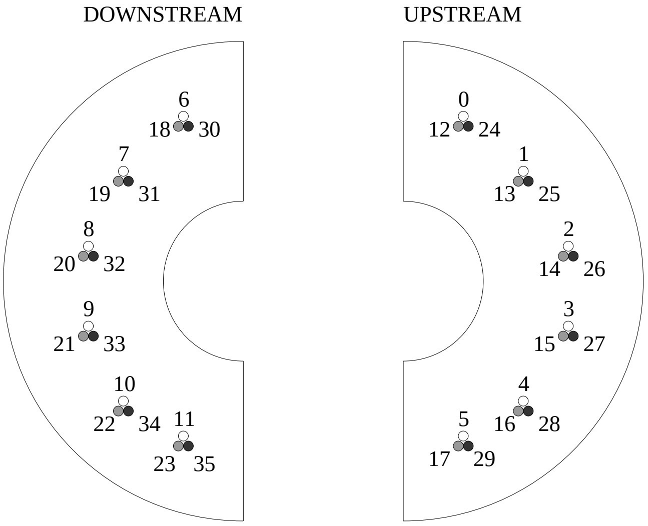

Figure 7.1: LEDs for calibration. Different markers represent different attenuation factors.

is not used, variance of number of photons from a LED can be written as,

$$\sigma^2_{N_{ph}} = N_A + \left(\frac{dN}{dV}\bigg|_{V_0} \Delta V \right)^2 \tag{7.1}$$

where N_A is averaged number of photons, V is applied voltage and ΔV is fluctuation of V.

After the modification, the same quantity is written as,

$$\sigma^2_{N_{ph}} = N_A + \left(\frac{1}{f}\frac{dN}{dV}\bigg|_{V_1} \Delta V \right)^2 \tag{7.2}$$

where f and V_1 are adjusted so that N_A does not change from eq. 7.1.

When f is large enough and the light intensity of the LED increases as a function of applied voltage more slowly than an exponential function, the contribution from the noise will be negligible. Figure 7.3 shows measured intensity of LED as a function of applied voltage. Actually, the increase is much slower than an exponential function.

Geometrical effect(solid angle of PMT viewed from a LED) and quantum efficiency of PMTs have the same effect with the additional attenuation by the filter. In total, attenuation of 1000 is possible and it makes the effect of noise negligible.

7.1.2 Photo-cathode quantum efficiency(Q.E.)

Q.E. is measured by comparing output of PMTs from scintillation by alpha source(^{241}Am) with simulation. In this discussion, Q.E. includes also collection efficiency. To estimate Q.E. of each PMT, peaks of PMT outputs for each source-PMT pair was compared with simulation in which fixed Q.E.(16 %) is used.

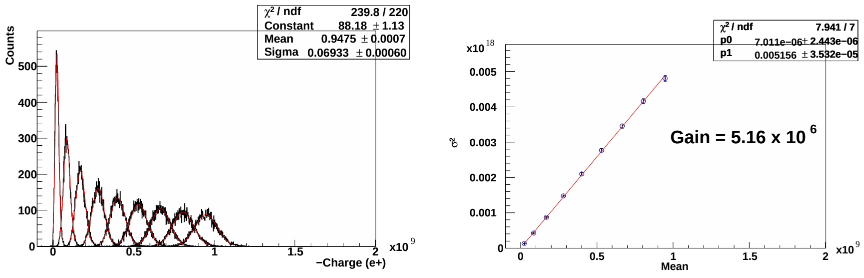

(a) (b)

Figure 7.2: LED gain calibration. (a) Spectrum of charge of a PMT. Intensity of LEDs are changed in 9 steps. (b) Mean and σ^2 of fitted Gaussian functions. Gain can be estimated from the slope of the plot.

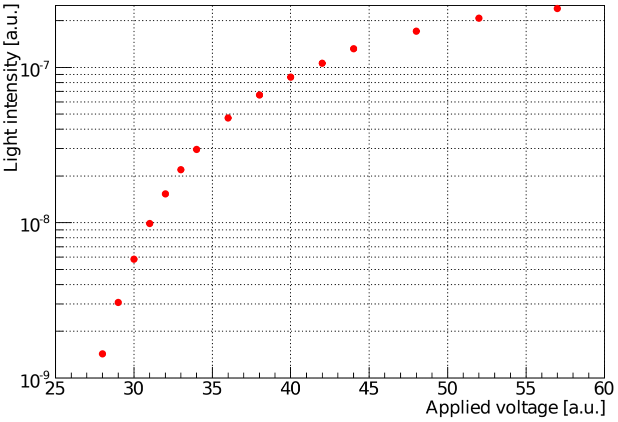

Figure 7.3: LED intensity and applied voltage.

In the simulation, reflection on the PMT window was calculated from Fresnel equation and Snell's law. Alpha sources are suitable for this purpose since the range is short (about 40 μm in liquid xenon), and they can be considered as point-like sources. In the large prototype, alpha sources on plates of one inch diameter were put on PMT holders. For the final detector, alpha sources put on wires were produced. It was also tested by using the large prototype. In the final detector, five alpha sources are put on each wire, and the size of each source is 1 mm. Diameter of a wire is 100 μm. In total 25 alpha sources on five wires were installed as shown in fig.7.5. A picture of an alpha source wire and a LED bundle is shown in fig.7.6.

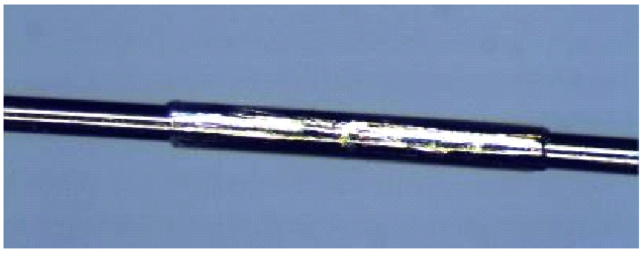

Figure 7.4: Alpha source on a wire. Length of the source is 1 mm, and diameter of the wire is 100 μm.

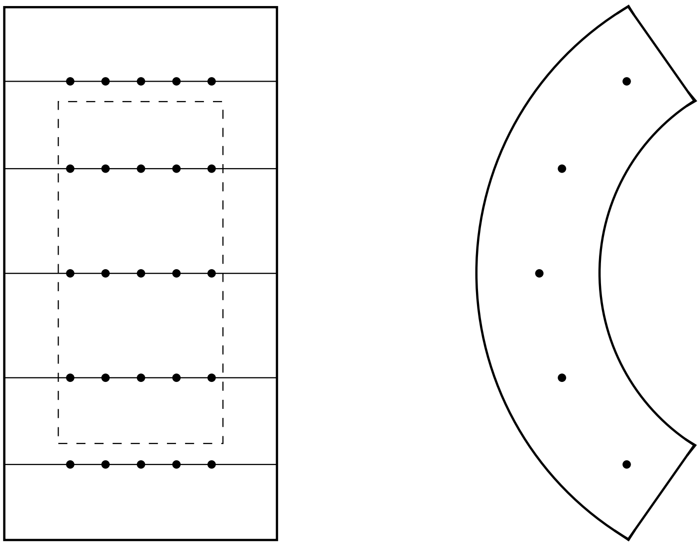

Front view Side view

Figure 7.5: Positions of alpha sources in the detector. Solid and dashed boxes in the left figure are outer and inner faces respectively.

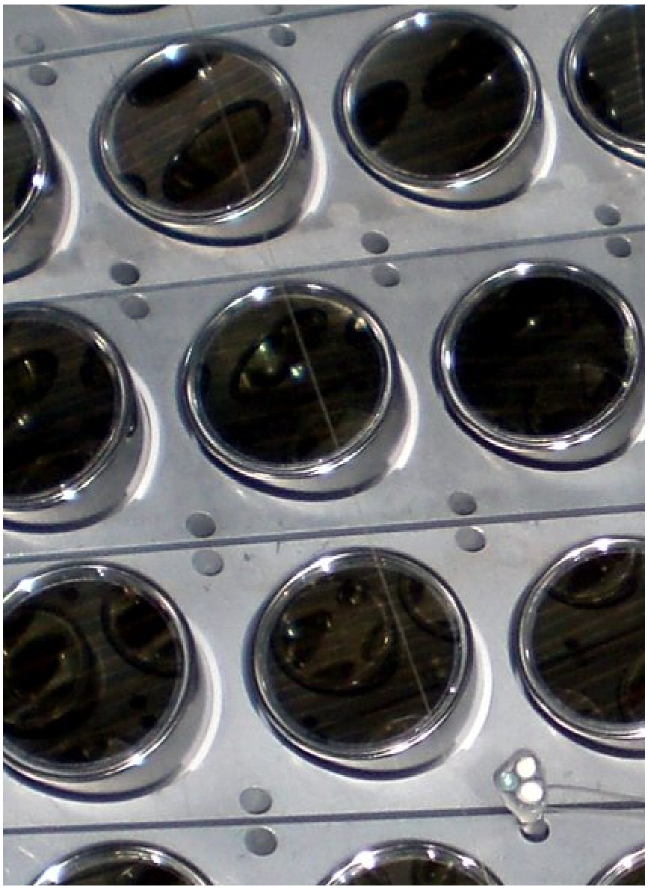

Figure 7.6: Alpha source wire and LED bundle

There are three advantages of wire sources compared to plate sources.

- In the case of plate sources, a half of solid angle viewed from energy release position is covered by the plate, hence practical amount of scintillation light is close to the half of alpha energy. While in case of wire sources, range of alpha particle and the width of wire are comparable, so more scintillation light is observed by PMTs.
- A plate source can be put only on the PMT holders, while a wire source can be put any place in the fiducial volume without making shadows in gamma ray measurements. It makes possible to illuminate all the PMTs with smaller number of alpha sources.
- Since wire sources are located in the fiducial volume, geometrical relation between PMTs and light a source is closer to gamma ray measurement.

Figure 7.7 shows weighted mean of position of PMTs in alpha events. Top three wires are in gas and bottom two are in liquid xenon. In liquid xenon, weighted mean positions make rings shown in this figure. In liquid, range of an alpha particle is comparable to the thickness of the wire, so the wire makes shadow as shown in fig.7.8. An interesting point is that the radius of the ring depends on thickness of the wire and scattering length of xenon. An estimation of Rayleigh scattering length by using the rings is described in section 5.2.1.

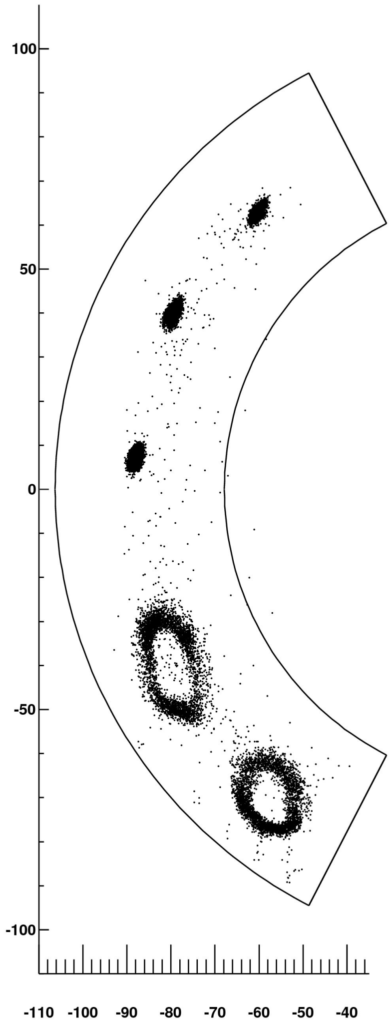

Figure 7.7: Weighted mean position of PMT outputs in alpha events. Bottom two wires are in liquid and other three wires are in gas xenon. Middle wire is reconstructed upper than real position due to reflection on liquid surface.

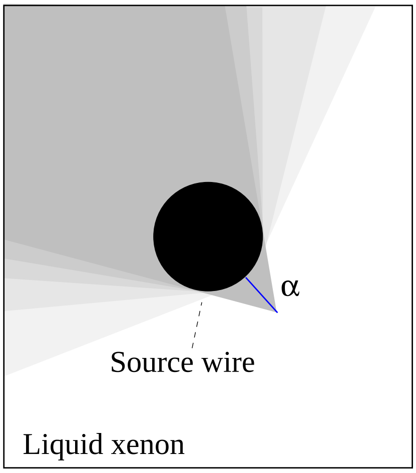

Figure 7.8: Alpha particle and the wire. Diameter of the wire is 100 μm and the range of alpha particle in liquid xenon is about 40 μm.

7.1.3 Time offset

There are systematic time differences in channels due to different path lengths of signals from the PMTs to the readouts, and due to path lengths of trigger stop signal from the trigger system to readouts. To calibrate the offsets, LEDs installed in the gamma ray detector is used. These LEDs are same ones used for gain calibration.

Measured time of a PMT can be written like equation 7.3.

$$T_{\mathrm{measured}} = T_{\mathrm{emit}} + T_{\mathrm{travel}} + T_{\mathrm{statistics}} + T_{\mathrm{transit}} + T_{\mathrm{electronics}} - T_{\mathrm{trigger}} \quad (7.3)$$

where, T_{emit} is the time of photon emission, T_{travel} is the time for a photon to travel in xenon to PMT, T_{transit} is the time of electron multiplication in a PMT, $T_{\mathrm{electronics}}$ is the time delay in electronics including cables, T_{trigger} is the time when trigger stop signal comes to a readout channel. Observed time have a delay when number of photo-electron is small($T_{\mathrm{statistics}}$). The purpose of time offset calibration is to estimate $T_{\mathrm{transit}} + T_{\mathrm{electronics}} - T_{\mathrm{trigger}}$, because this number is independent of light sources.

To investigate time offset, a LED is flashed with rather high intensity during a measurement to make $T_{\mathrm{statistics}}$ negligible. In principle, by subtracting T_{travel} from T_{measured}, time offsets relative to a reference PMT can be obtained. However, there are two points to be considered. The one is that velocity of LED light in liquid xenon is unknown, and the second is that one LED can not illuminate all the PMTs in the gamma ray detector.

In the gamma ray detector, LEDs were located at twelve different positions in year 2007 setup. So several measurements can be done where in each measurement, only one LED is flashed. About 5000 events were recorded in each measurement, and mean of time of each PMT is estimated by fitting the distribution of events with Gaussian function.

Connection of two different measurements can be done by using PMTs which were illuminated in both the measurements. To align two measurements, a scatter plot of $T_i^0 - T_i^1$ v.s. $D_i^0 - D_i^1$ are fit with a linear function, where T_i^j is a time of i-th PMT in j-th measurement relative to a reference PMT and D_i^j is a distance from a LED to i-th PMT in j-th measurement. Reference PMTs are not necessary to be same in all the measurements. Intercept of the linear function is the difference of references in two measurements, and the value is independent of PMT time offsets or speed of light. The slope represents the speed of light in liquid xenon.

Figure 7.9 shows measured time as a function of distance from LEDs. One graph corresponds to a PMT, and a point corresponds to a measurement. White markers are time before correction, and lines are expectation with assuming estimated speed of light of 1.43×10^8 m/sec. The difference between white markers and the line is equivalent to the time offset of the channel. Figure 7.10 shows uncertainty of offset calibration of all the PMTs. Many PMTs were calibrated with uncertainty better than 200 psec.

The method is used to correct large offset like fig.7.9-d. More precise time offset is estimated from CEX data by using time difference distribution of each PMT with respect to a tagging detector with statistical uncertainties better than 10 psec. Offset calibration by using CEX data could be done only about 100 PMTs because the CEX test was done for a part of the inner face in 2007. Practically, these PMTs contribute to the time resolution because the time of a

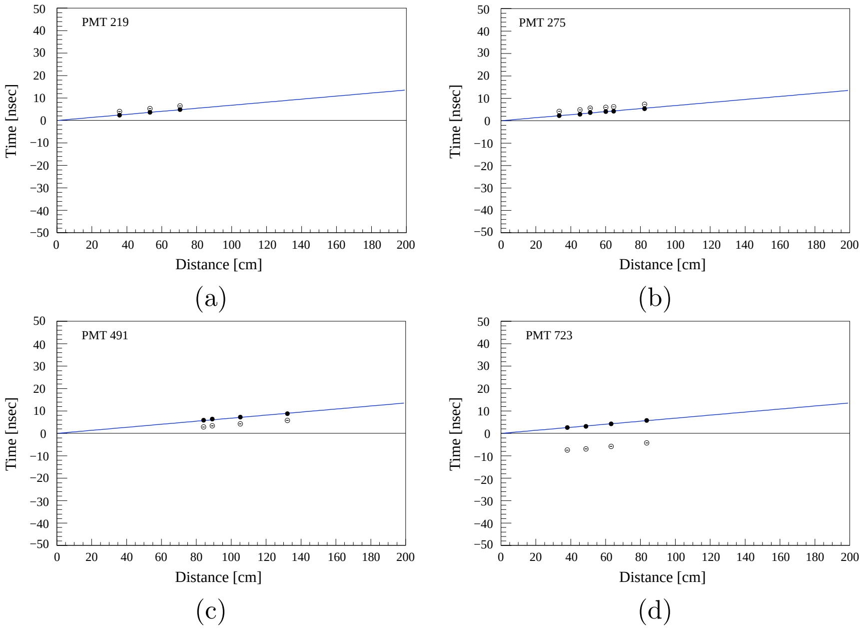

(a) (b)

(c) (d)

Figure 7.9: Time v.s. distance for time offset estimation. The difference between white markers and the line is equivalent to the time offset of the channel, so PMT 723 has a larger offset than other PMTs in this figure.

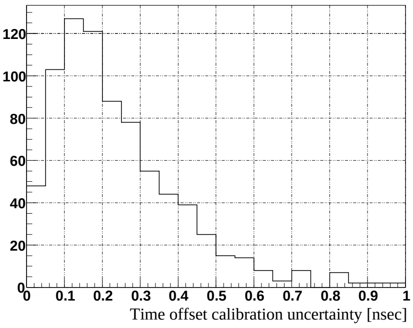

Figure 7.10: Time offset calibration uncertainty. The number is standard deviation of points in fig.7.9 from a line of speed of light.

gamma ray is estimated by a weighted mean, and the weight is proportional to $1/\sqrt{N_{phe}}$, where N_{phe} is number of photoelectrons observed by a PMT.

7.2 Structure of event reconstruction

Reconstruction of the gamma ray detector is done in following steps.

1. Decoding and calibration of raw waveform data.
2. Waveform analysis of each PMT. Here, charge and time of each PMT are extracted.
3. Calibration of each PMT is done for charge and time. All the calibration parameters are read from a database.
   - Attenuation in electronics are corrected.
   - Output charge is converted to number of photo-electrons on photocathode by using gain.
   - Number of photo-electrons are converted to number of photons by using Q.E..
   - Systematic time offset by different path length from PMTs to the readout is corrected.
4. Pile-up identification is done by using spatial and temporal distribution of PMT outputs.
5. Several kinds of algorithms are implemented to reconstruct energy, position and time of impinging gamma rays.

As a result, energy deposit, position and time associated with a gamma ray are filled in a persistent data structure so that they are used for combined analysis with reconstruction of positrons. The gamma ray detector is not sensitive to the direction of gamma rays, thus combined analysis is done by assuming gamma rays are emitted at the reconstructed muon decay point by positron analysis.

7.3 Waveform analysis

In the MEG experiment, all the waveforms of sub-detectors are recorded so that pileup events can be find in offline analysis. So, the first step of the offline analysis chain is waveform analysis. Not to degrade DAQ speed, all the calibrations are not done in DAQ frontend, but some of them are done in offline analysis.

7.3.1 Calibration and noise reduction

Voltage calibration

Voltage calibration of ADCs on DRS can vary depending on the temperature of the chip, and the temperature can be changed by readout event rate. Relation between ADC value and voltage is not linear. The voltage calibration to correct these effects is done in DAQ frontend so that the raw waveform data is already written in volt. The calibration parameter is obtained by using internal DC generator on DRS boards.

A response curve of DRS is shown in fig.7.11. The curve is not linear and the resolution is better for smaller pulse than 500 mV. Typical pulse height of waveforms in the MEG experiment is adjusted to be smaller than 500 mV.

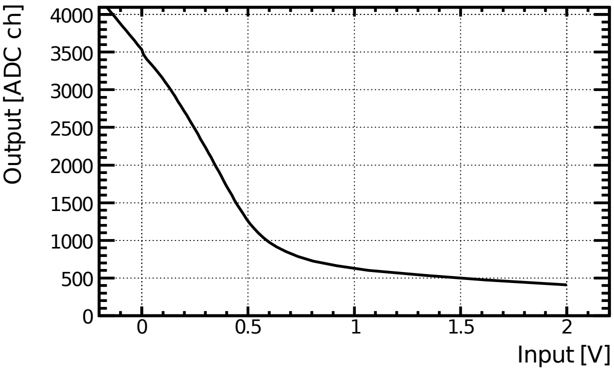

Figure 7.11: Response curve of DRS2.

Time calibration

Time differences between two sampling points depend on delay time of inverters between sampling cells on DRS chips. The calibration parameters to cancel it was obtained from a measurement of sine waves, and they are stored in the database. In this measurement, sine waves with a known frequency(80 MHz) were measured and the time of each cell was determined so that the measured data reproduce the known shape of sine waves.

The phase of the stop signal of an event in the domino ring is roughly determined by using a pulse generated on the DRS board by a trigger stop signal coming through the back plane of a VME crate. The resolution of the rough estimation is not good enough to use for analysis. And the timing can be affected by path length from a trigger board which generates the stop signal and each DRS board. The speed of DRS sampling is regulated, but it is not necessarily constant. For correction of domino wave speed variation and alignment of chips, a common clock signal with steep edges is provided to all the DRS chips with the same length of cables. A typical waveform of the clock signal observed by DRS is shown in fig.7.12. Time calibration of clock analysis is done in offline for each event. The clock waveforms are fitted by template waveform and the time of each edge is estimated. Time of each sampling points of each channel is reassigned so that time of edges become same for all the DRS chips. Standard deviation of the time correction by this analysis (difference of time before and after the correction) around time region of typical pulses is about 0.7 nsec.

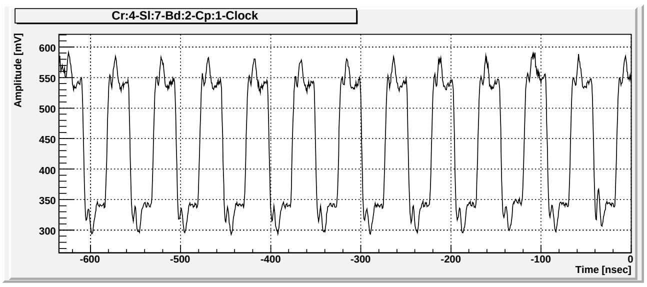

Figure 7.12: Typical waveform of clock signals for time calibration.

Noise reduction

It is known that there is a noise by cross-talk with sharp edges of clock signal. Since the shape of the noise is always same, and the time can be estimated from the clock signal, it is possible to subtract it in analysis. A template waveform was created from random trigger data, and the subtraction of the template waveform is done for each event.

7.3.2 Charge integration

Number of photoelectrons of a PMT is estimated from an integrated charge of waveform in a time window. A common time window is used for all the PMTs in each event, and the time window is determined relative to the time of a peak of sum waveform of PMTs. To cancel an effect of slow component noise, the baseline voltage is determined for each PMT at every event by using a part of waveform before a pulse.

During 2007 run, a slow component noise was observed. The interval of the noise was the same level of the DRS time window, therefore the effect can not be canceled by baseline subtraction completely. To reduce the effect of the noise, high-pass filtering was done in offline analysis. Figure 7.13 show a raw waveform and that after the filtering. Effectively, it is decreasing amount of integrated charge, and it makes the signal to noise ratio (S/N) worse for high frequency noise.

In the case of 2007 run, the filtered waveform improves energy resolution, because the effect of slow frequency noise was larger than high frequency one. Before applying the filter, contribution of noise to 54.9 MeV energy peak was 4.5 % and it is improved to 2.0 % by the filtering. For the analysis in this section, filtered waveforms were used. The filtering was done by subtraction of a waveform after moving average of 89 sampling points. It corresponds to the cut off frequency of 10.7 MHz[59]. Charge integration was done in 45 nsec range.

7.4 Reconstruction

In this section, a local coordinate system for the gamma ray detector is often used. Figure 7.14 shows the local coordinate system (u, v, w) and the global

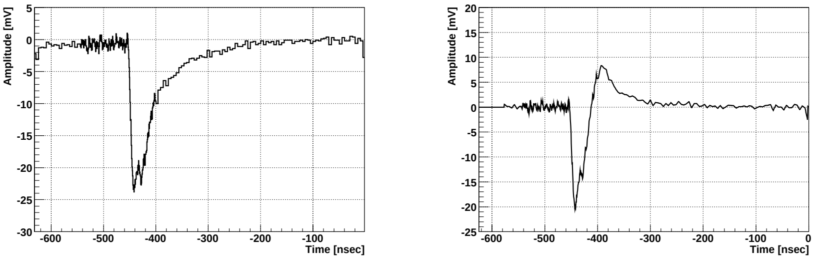

(a) (b)

Figure 7.13: Waveform filtering. (a) Raw waveform. (b) Filtered waveform.

coordinate system (x, y, z). The origin of (x, y, z) is defined from the position of the COBRA magnet, while that of (u, v, w) is the center position of the inner face of the gamma ray detector. In the case of 2007 run, conversion of the two coordinates can be written as,

$$u = z \tag{7.4}$$

$$v = r_0 \cdot \tan^{-1}(-y/x) \tag{7.5}$$

$$w = \sqrt{x^2 + y^2} - r_0 \tag{7.6}$$

where $r_0 = 67.85$ cm is the radius of the inner face. (u, v) is the projected position on the inner face, and w is the depth from the inner face.

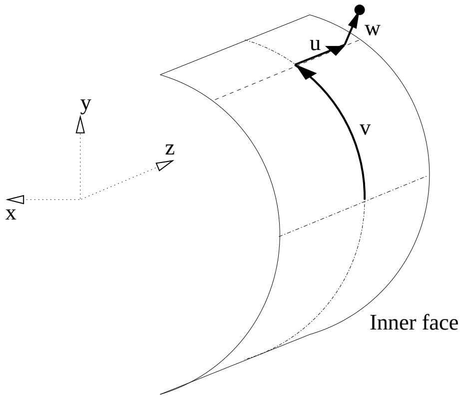

Figure 7.14: Local coordinate system of the gamma ray detector. The target is located around the origin of (x, y, z) coordinate system.

7.4.1 Position reconstruction

The purpose of the reconstruction is estimating the position of the first conversion point in the active volume, instead of center of the shower. For this purpose, position reconstruction is done by fitting PMT charge distribution on the inner face in a limited region around the initial estimated position. (u, v)

can be estimated from the mean of a fitting function, and w can be estimated from the width of the function. The initial estimation is the center position of the PMT with the maximum charge at the event. The estimation is improved at the second step, where the estimation is the weighted mean of the center position of the max PMT and eight surrounding PMTs. At the third step, projection to u and v are fitted by a function independently. The fitting function is

$$f(u,w) = \frac{\tan^{-1}\left(\frac{u-\bar{u}-r_{\mathrm{cath}}}{w}\right) - \tan^{-1}\left(\frac{u-\bar{u}+r_{\mathrm{cath}}}{w}\right)}{\tan^{-1}\left(\frac{-r_{\mathrm{cath}}}{w}\right) - \tan^{-1}\left(\frac{r_{\mathrm{cath}}}{w}\right)} \tag{7.7}$$

$$f(v,w) = \frac{\tan^{-1}\left(\frac{r_0\cdot\sin\left(\frac{v-\bar{v}}{r_0}+\phi_{\mathrm{cath}}\right)}{w+r_0\cdot\left(1-\cos\left(\frac{v-\bar{v}}{r_0}+\phi_{\mathrm{cath}}\right)\right)}\right) - \tan^{-1}\left(\frac{r_0\cdot\sin\left(\frac{v-\bar{v}}{r_0}-\phi_{\mathrm{cath}}\right)}{w+r_0\cdot\left(1-\cos\left(\frac{v-\bar{v}}{r_0}-\phi_{\mathrm{cath}}\right)\right)}\right)}{\tan^{-1}\left(\frac{r_0\cdot\sin\left(\frac{\bar{v}}{r_0}+\phi_{\mathrm{cath}}\right)}{w+r_0\cdot\left(1-\cos\left(\frac{\bar{v}}{r_0}+\phi_{\mathrm{cath}}\right)\right)}\right) - \tan^{-1}\left(\frac{r_0\cdot\sin\left(\frac{\bar{v}}{r_0}-\phi_{\mathrm{cath}}\right)}{w+r_0\cdot\left(1-\cos\left(\frac{\bar{v}}{r_0}-\phi_{\mathrm{cath}}\right)\right)}\right)} \tag{7.8}$$

where r_0, r_{cath} and ϕ_{cath} are the radius of the inner face, the radius of the PMT photo-cathode and ϕ of the PMT photo-cathode respectively. The average of w estimated at two fittings for u and v projections are used as the initial value of the fitting at the next step. For the fitting, 4×4 PMTs around the mean position at the previous step are used to eliminate effect of PMT hits in a distance by Compton scattering and pileups.

At the last step, a three dimensional fitting is done by using all u, v and w as free parameters with a function based on equation 7.7 and 7.8. In this step, light attenuation in the liquid xenon is taken into account.

Figure 7.15 and 7.16 shows fittings to simulated $\mu^+ \to \mathrm{e}^+\gamma$ event in the case of shallow(w=1.44 cm) and deep(w=10.58 cm) conversions. In the plot (a), each box represents amount of light of a PMT. (b) and (c) shows the projection to u and v directions and fittings. It is clearly seen that a deep conversion makes broader light distribution than a shallow one.

Figure 7.17 shows a comparison between the true first interaction depth and the reconstruction. Resolution is improved from a method used for the large prototype, and it does not become worse in the shallow part very much. When energy deposit distribution becomes broader in u or v direction than typical events, reconstruction can be deeper than true depth. By the reason, the distribution of the residual is asymmetric. In fig.7.18, the sigma of residual(reconstructed - MC) for each side of Gaussian is shown as a function of the reconstructed depth.

u and v resolutions for simulated signal events are shown in fig.7.19. Resolution of u looks worth than v, because the coordinate system is a projection to the inner face. For example, 10 mm difference of u at $(u, v, w) = (0, 0, 25)$ cm and $(u, v, w) = (25, 0, 25)$ cm correspond to 7.3 mm and 6.8 mm difference of v at those points respectively. Angular resolutions are shown in fig.7.20 for θ and ϕ. θ and ϕ correspond to u and v directions respectively. In the plot, events outside of acceptance are not used. The acceptance is shown in fig.3.7. Resolutions are almost same for θ and ϕ in the central region of the detector,

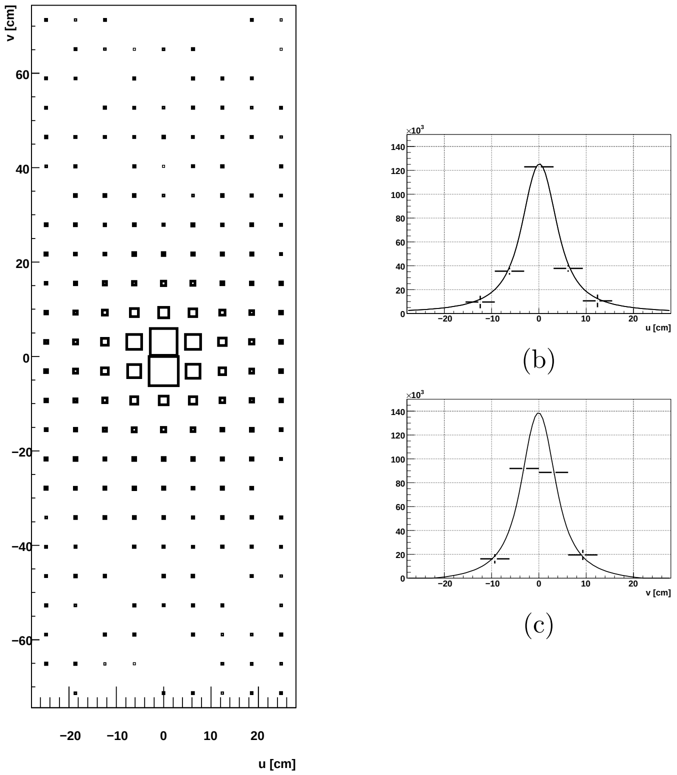

(b)

(c)

(a)

Figure 7.15: Fitting of position for a shallow event for a simulated signal event. (a) 2D histogram of PMT outputs. (b) Fitting of u projection. (c) Fitting of v projection.

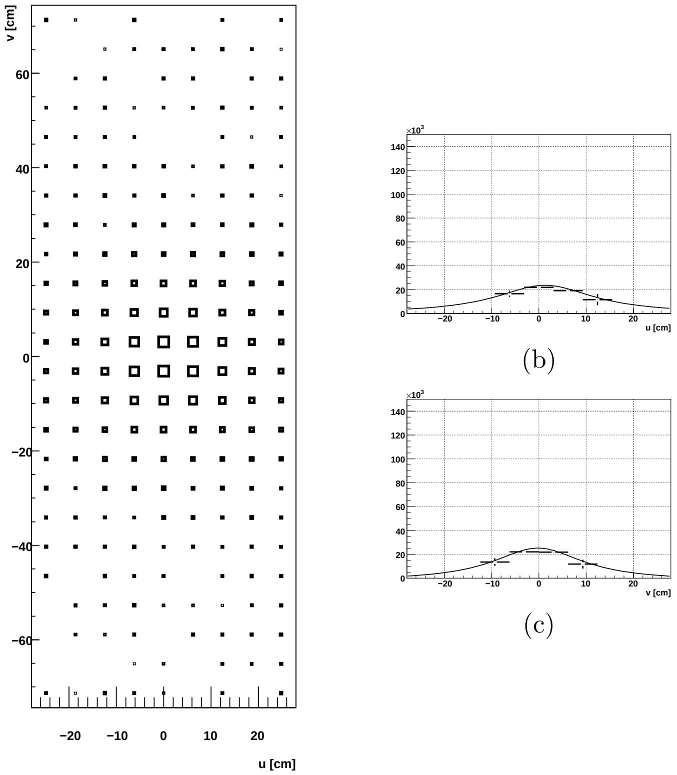

(a) (b) (c)

Figure 7.16: Fitting of position for a deep event for a simulated signal event. (a) 2D histogram of PMT outputs. (b) Fitting of u projection. (c) Fitting of v projection.

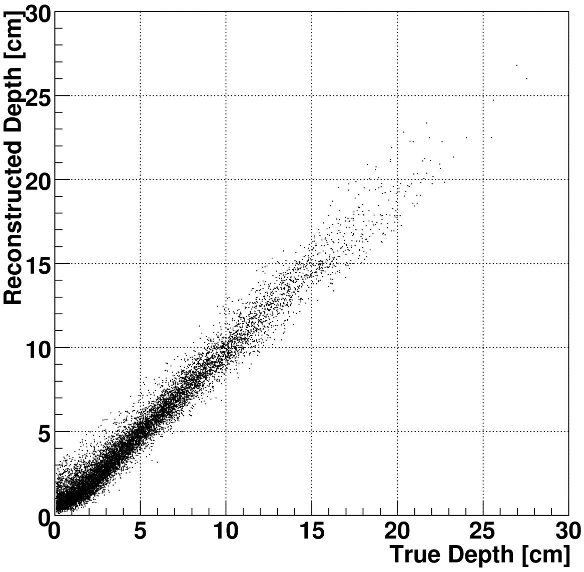

Figure 7.17: True and reconstructed position for $\mu^+ \rightarrow e^+\gamma$ event simulation. Events in the acceptance are shown.

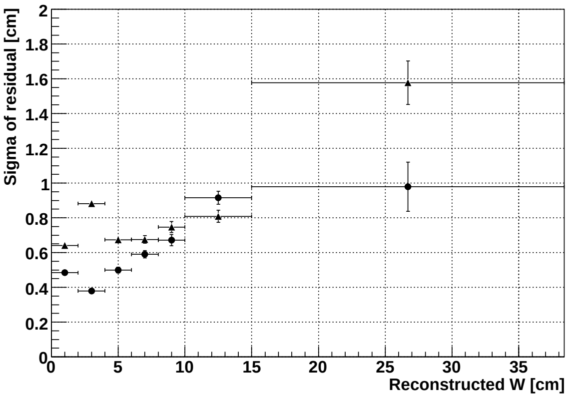

Figure 7.18: Sigma of residual of w for upper (triangle) and lower (circle) sides. Sigma of the upper part is larger due to variation of the shape of shower.

while θ becomes worse at the edge of u. This is because reconstruction is done by PMTs in the inner face, and at the edge the fitting can be done to only a part of the distribution. This is the same for ϕ at the edge of v.

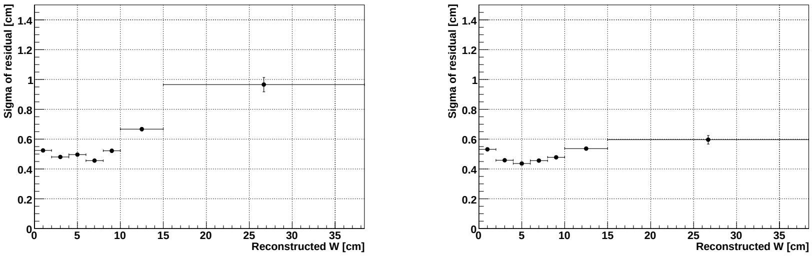

(a) (b)

Figure 7.19: Resolution of (a) u and (b) v as a function of the reconstructed depth.

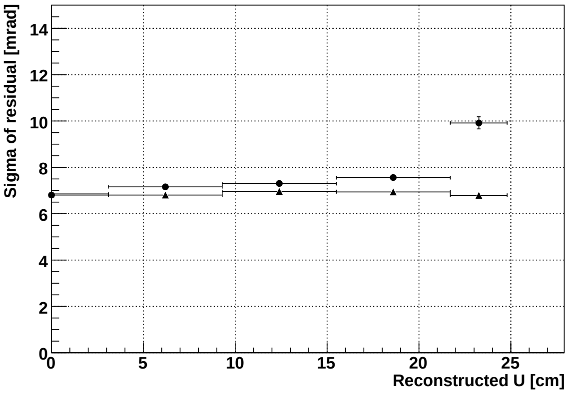

Figure 7.20: Angular resolution for θ direction(circles) and ϕ direction(triangles) as a function of reconstructed u.

Differences of position resolutions depending on the position relative to inner face PMTs were studied. The result is shown in table 7.1.

In order to measure position resolution from experiment data in CEX runs, a lead plate of 1.8 cm thickness was put between the detector and the COBRA magnet. Reconstructed positions are shown in fig.7.22. During the runs, gamma rays in front of 2×3 PMTs were used for the trigger. Position resolution was estimated from the shape of a edge in fig.7.22-a. The edge of the plate lies on the middle of C and D in fig.7.21 horizontally, and the measurement was for ϕ direction. For events deeper than 2 cm, measured resolution is 7.6± 1.2 mm. Resolutions for each depth slice is shown in fig.7.22-b. The best value in depth slices is 5.9 ± 1.4 mm.

	ϕ resolution	θ resolution
Position A	6.44 ± 0.09	6.66 ± 0.08
Position B	6.64 ± 0.08	7.56 ± 0.10
Position C	7.64 ± 0.09	6.73 ± 0.08
Position D	7.52 ± 0.10	7.92 ± 0.10

Table 7.1: Position resolutions at several relative positions [mrad]. The definition of positions are shown in fig.7.21. 7 mrad corresponds to 4.75 mm on the inner face.

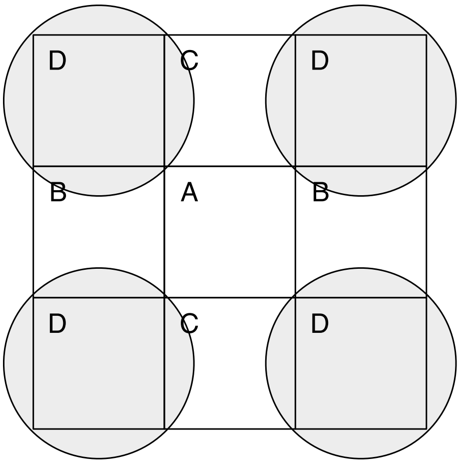

Figure 7.21: Definition of relative position from PMTs.

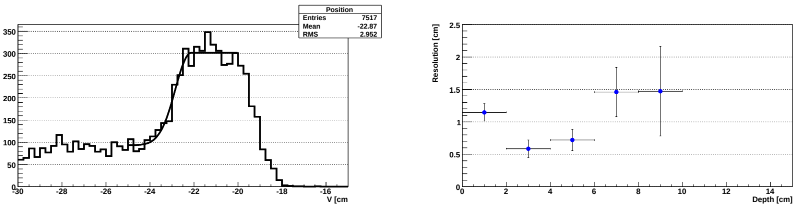

(a) (b)

Figure 7.22: Measured position resolution. In this plot, events around 54.9 MeV and deeper than 2 cm were selected. (a) Fit of collimator edge. The data was taken for $v > -19$ cm by trigger. (b) Resolution and depth.

7.4.2 Energy reconstruction

In the case of the large prototype, photo-cathode area coverage of each PMT were same on all the faces. On the other hand, in the case of the final detector, it depends on position of PMTs as shown in fig.7.23. For example, the coverage on the outer face is 2.6 times less than that of inner face. Therefore, a simple sum of PMT charge depends on the position and the depth of the first conversion point. In order to cancel the effect, $Qsum2$ was introduced for energy reconstruction.

$$Qsum2 = \sum c_i \cdot Q_i \tag{7.9}$$

where, c_i is a correction factor which is proportional to the inverse of photo-cathode coverage of a PMT. Q_i is PMT charge.

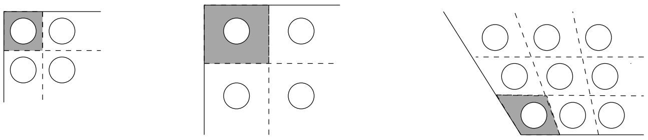

Figure 7.23: Photo-cathode coverage on different faces. The picture shows inner, outer and top faces. The circles are area of PMT photo-cathodes.

Even after the correction, $Qsum2$ is not completely flat in the fiducial volume due to geometrical effect (difference of overall PMT coverage depending on position), and that of dead channels. In fig.7.24, $Nsum2$ (weighted sum of outputs of all the PMTs after Q.E. correction) dependencies on reconstructed positions are shown for simulation data. In order to correct such effects, further correction was done by using measured data. To obtain calibration constants, gamma rays which satisfy following conditions are needed.

- It must come from the target position.
- It must have a monochromatic energy.
- It must impinge whole the acceptance of the gamma ray detector, with high enough rate.

Furthermore, if the energy is known, it can be used for calibration of absolute scale of conversion from $Qsum2$ to energy. There are two candidates which satisfy this condition, namely gamma rays from CEX and those from nuclear reaction which can be produced by the C.W. accelerator.

For the calibration of future physics runs, pion charge exchange could be used. But in 2007, full scan in the acceptance was not done with pion beam due to a limited beam time. Hence, in this thesis, C.W. data is used for the energy scale calibration.

When a gamma ray converts in the shallow part of the detector, $Qsum2$ depends on the position very strongly because solid angle of the nearest PMT affects very much. To reduce the effect, a special treatment is done for shallow events. In this analysis, when the conversion depth is less than 2 cm, $Qsum2 - Q_{\max}$ was used, where $Q_{\max}$ is the charge of the PMT with maximum output in the event. Scaling factors from number of photons to energy were extracted from

17.6 MeV peak in C.W. runs for events in $w < 2$ cm and those for $w >= 2$ cm separately. As seen in fig.7.25, connection at $w = 2$ cm is done smoothly, and depth dependence is well corrected.

Fittings to evaluate the resolution were done in the same way with the large prototype. Figure 7.26 and 7.27 show resolution (σ of right edge) dependence on depth and impinging position for simulated signal events.

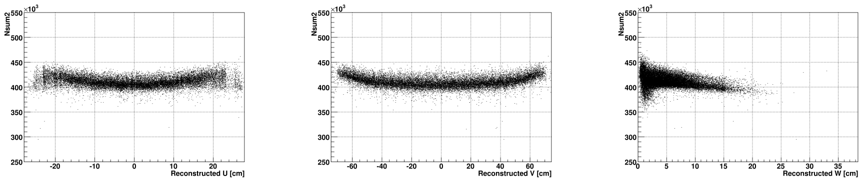

(a) (b) (c)

Figure 7.24: Nsum2 and reconstructed positions for simulated signal events.

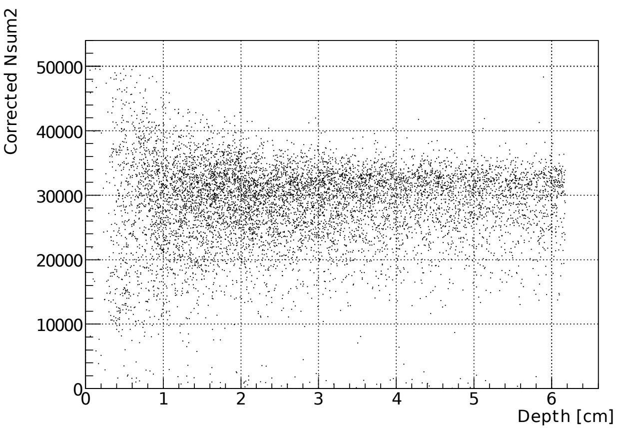

Figure 7.25: Corrected $Nsum2$ and depth for C.W. experiment data with lithium target. The peak of $Nsum2 = 3200$ corresponds to 17.6 MeV. For shallower events than 2 cm, $Qsum2 - Q_{\max}$ is used.

Real energy resolution of the detector was estimated from CEX data for 54.9 MeV and 83.0 MeV for events deeper than 2 cm. σ of right edge is 2.8 ± 0.1 and 2.9 ± 0.1 % for 54.9 and 83.0 MeV respectively. Figure 7.28 shows histograms of energy for both energies. The resolution depends on depth as shown in fig.7.29. The best resolution in slices by depth is 2.1 ± 0.2 %.

Figure 7.30 shows peaks of $Qsum2$ for various gamma ray energies. The numbers are normalized for 54.9 MeV peak. 54.9 and 83.0 MeV peaks are obtained from CEX data. 17.6 and 14.6 MeV peaks are from nuclear reaction of lithium, 6.13 MeV is from that of florin during C.W. beam test with Lithium fluoride target. 4.4 MeV is from a nuclear reaction of boron. Center values of

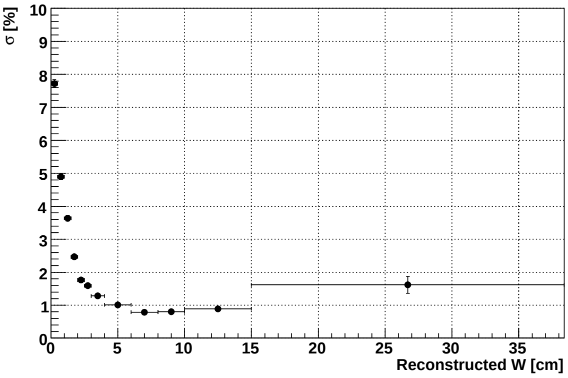

Figure 7.26: Energy resolution and reconstructed depth for simulated signal events.

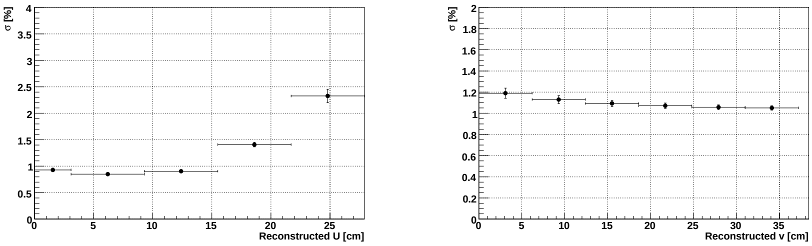

(a) (b)

Figure 7.27: Energy resolution and reconstructed position for simulated signal events.

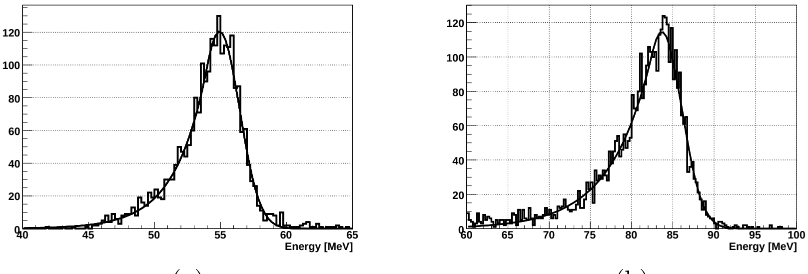

(a) (b)

Figure 7.28: Fitting to estimate energy resolution for 2007 data. In this plot, events than 2 cm were selected. (a) 54.9 MeV peak. (b) 83.0 MeV peak.

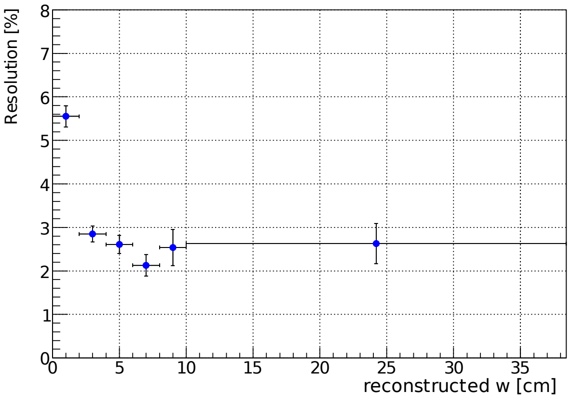

Figure 7.29: Energy resolution and depth for 54.9 MeV peak for 2007 data.

points in this figure except for 14.6 MeV peak are within ±0.8 % from a fitting linear line.

14.6 MeV peak is naturally wide as shown in fig.2.18 and the peak is not very clear compared to other monochromatic peaks.

The response of the detector shows a good linearity in this wide range of energy.

7.4.3 Time reconstruction

Time of each PMT is calculated by constant fraction discrimination in offline analysis so that it does not depend on pulse height very much. Even if the constant fraction algorithm is used, measured time has a delay due to scintillation photon statistics. Time offset of each PMT is firstly measured by using LED which is discussed at 7.1.3. More precise time offset and statistical delay are estimated from CEX data by using time difference distribution of each PMT with respect to a tagging detector with taking into account distance between interaction positions in the gamma ray detector and the PMT.

An estimate of a gamma ray's time by a PMT can be written as

$$T_\gamma = T_{\mathrm{PMT}} - T_{\mathrm{statistics}} - T_{\mathrm{propagate}} - T_{\mathrm{offset}} \tag{7.10}$$

where T_{PMT}, $T_{\mathrm{statistics}}$, $T_{\mathrm{propagate}}$ and T_{offset} are -measured time by a PMT, time delay due to scintillation photon statistics, propagation time from energy deposit point to the PMT and time offset due to cables and electronics.

Timing of a gamma ray is estimated by taking weighted average of each PMT's estimate. The weight is proportional to $\sqrt{N_{phe}}$. PMTs with more than 200 photo-electrons are used for taking the average. The resolution was measured in two ways as it was done by the large prototype. An intrinsic resolution was measured from difference of estimation by the top half and the bottom half of the detector. Figure 7.31 shows a distribution of time difference of the top and the bottom half. For this plot, events deeper than 2 cm and

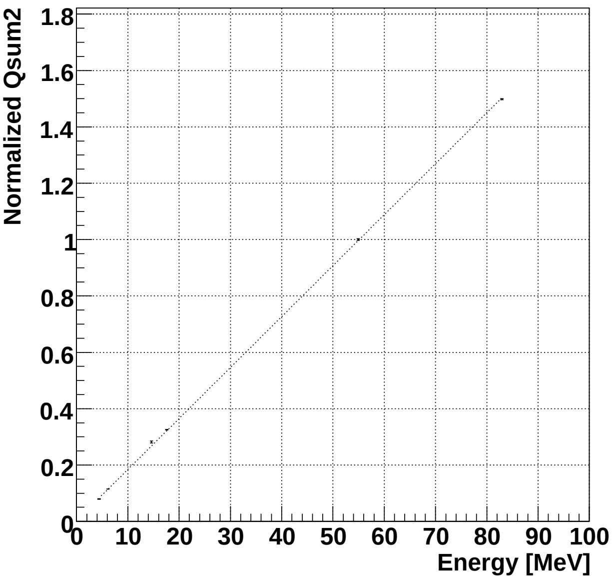

Figure 7.30: $Qsum2$ peaks of various gamma ray energies.

$|v| < 1$ cm were selected so that time resolution of the top and the bottom half are approximately same.

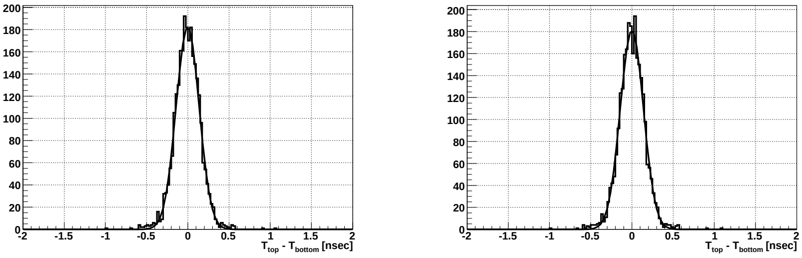

(a)

(b)

Figure 7.31: Time difference of top and bottom half. (a) 54.9 MeV peak (b) 83.0 MeV peak

The distribution widths are 164 ± 2 and 140 ± 2 psec for 54.9 and 83.0 MeV peaks respectively. If we assume the resolution is determined by scintillation photon statistics, the intrinsic resolution($\delta t_{\mathrm{intrinsic}}$) can be written as

$$\delta t_{\mathrm{intrinsic}} = \delta(t_{\mathrm{top}} - t_{\mathrm{bottom}})/2$$

where $\delta(t_{\mathrm{top}} - t_{\mathrm{bottom}})$ is σ of time difference of estimations by top and bottom half of the gamma ray detector.

Figure 7.32 shows the time difference in 54.9 MeV peak for each slice of depth. The best in depth slices is 142 ± 4 psec.

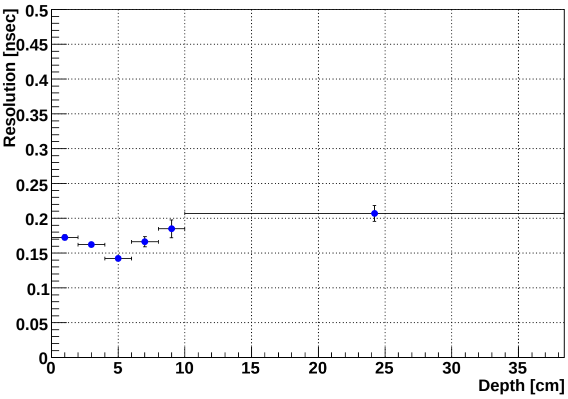

Figure 7.32: Time difference of top and bottom half for each depth slice.

The practical resolution was measured by comparing the time at the gamma ray detector and that at the tagging detector.

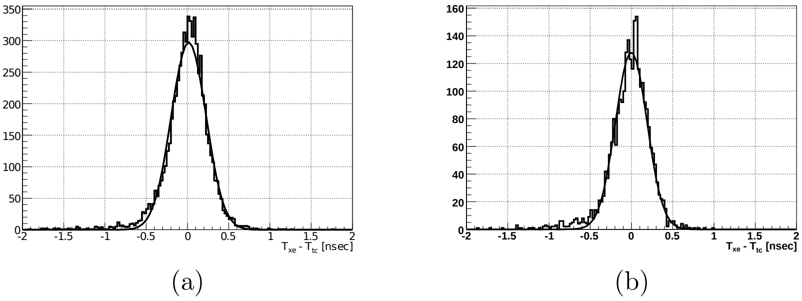

(a) (b)

Figure 7.33: Time difference of the gamma ray detector and the tagging detector. (a) 54.9 MeV peak (b) 83.0 MeV peak

The distribution widths of fitting functions in fig.7.33 are 205 ± 6 and 197 ± 8 psec for 54.9 and 83.0 MeV peaks respectively. These number includes depth resolution(35 $\sim$ 90 psec depending on depth, estimated from simulation), distributions of pion decay position(60 psec), tagging detector's resolution(90 psec) and time alignment of the gamma ray detector and the tagging detector. By subtracting these contributions, the practical time resolution for 54.9 MeV gamma ray for $w > 2$ cm is $\sqrt{(205)^2 - (60)^2 - (90)^2} = 175 \pm 5$ psec. Figure 7.32 shows the time difference in 54.9 MeV peak for each slice of depth. At the best depth, the practical time resolution for 54.9 MeV gamma ray is $\sqrt{(162)^2 - (60)^2 - (90)^2} = 121 \pm 8$ psec. The difference from intrinsic time resolution (72 ± 2 psec) is due to fluctuations of depth reconstruction and time alignment of readouts(80 psec). Effect from depth reconstruction fluctuation is estimated to be 51±12 psec from MC simulation. Taking into account these effects, practical and intrinsic time resolutions are consistent. Note that DRS time alignment uncertainty between the gamma ray detector and the tagging detector is included in 121 psec. The contribution is not subtracted from the resolution because the same contribution is present in physics analysis in time difference of a gamma ray and a positron. Contribution of the gamma ray detector to the resolution is evaluated to be 90.7 ± 8 psec by subtracting that of DRS alignment.

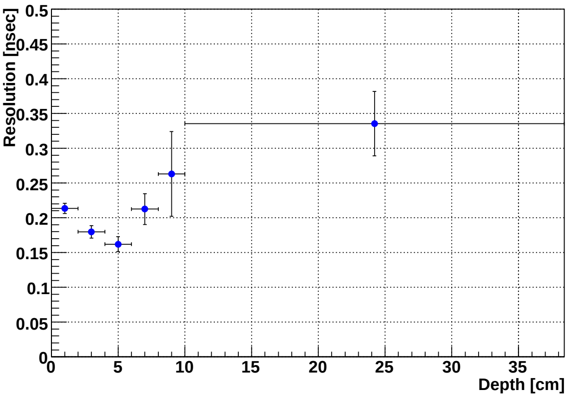

Figure 7.34: Time difference of the gamma ray detector and the tagging detector for each depth slice. These numbers include tagging detector's resolution(90 psec) and decay position distribution(60 psec).

7.5 Event type identification

In this section event type identifications of three possible sources of backgrounds are discussed. Since most of gamma rays from radiative muon decays and AIF have lower energy than those from signals, events reconstructed higher energy than actual gamma ray energy can be backgrounds. One is due to too large output by a PMT, that occurs when there is an energy deposit just in front of a PMT. Another source is a pileup of two gamma rays. Identification of cosmic rays is also discussed.

7.5.1 Higher tail identification

The total solid angle of PMT photo-cathode seen from the fiducial volume is almost uniform, and the sum of number of photoelectrons does not strongly depend on the shape of electro-magnetic shower in the volume. When the first conversion occurs very shallow part, the variance is larger. Therefore such events are analyzed in a special way which was already discussed. However, with a small probability, the detector can observe a larger amount of light than that expected from the position of the first conversion position. The typical event display is shown in fig.7.35. In this event, the first interaction occurs in the fiducial volume, then a low energy gamma ray travels and deposits energy just in front of an outer face PMT. Even with a small energy deposit, the PMT observes a large amount of light when the deposit point is in front of the photo cathode. This kind of events can be identified by searching a too sharp peak in spatial distribution of PMT outputs. Too sharp peak was searched from charge ratio of a PMT and an average of surrounding eight PMTs. Threshold was adjusted by using MC to be 15 for the outer face and 5 for top, bottom and lateral faces. Figure 7.36 shows the distribution of $Nsum2$ of simulated signal events with and without cut by too sharp peaks. Miss rejection(inefficiency of signal) by this selection is 2 % where ratio of reconstructed energy and true deposit energy is around one.

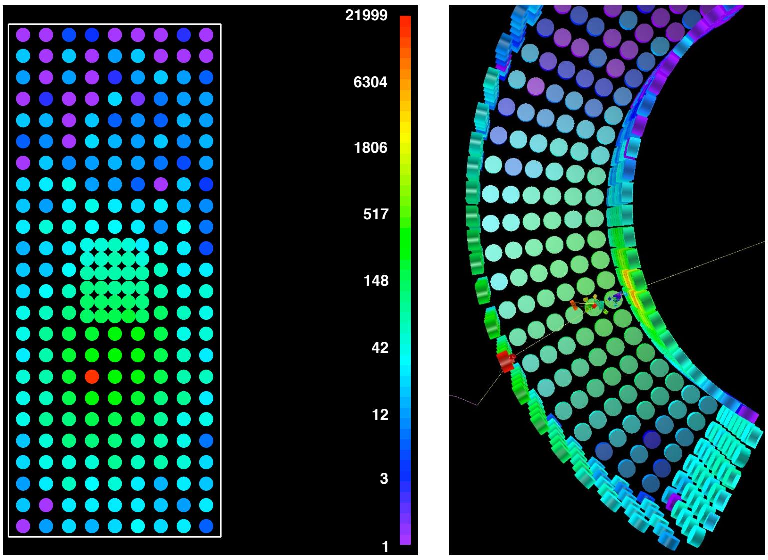

(a) (b)

Figure 7.35: Event display of a higher tail event in simulation. In this event, a part of energy was deposit in front of an outer face PMT by a low energy gamma ray. (a) shows a 2D map of PMT charge on the outer face. (b) is a 3D view of the event. Color code of energy deposits(small square boxes) represent time of deposits.

7.5.2 Pile-up identification

Identification of pile-up events where two gamma rays enter the detector will be important to improve limit of $\mu^+ \to e^+\gamma$.

In a simulation assuming a high muon stopping rate (1×10^8) 28 % of events have pileups during the decay time of scintillation, where definition of pile up is when area of overlap of waveforms corresponds to more than 0.5 MeV. In the case of a muon rate of 3×10^7, the probability should be around 8.4 %.

To identifying pile-up events, two complementary types of algorithms were developed. The most case of pile-ups is an accidental coincidence of two gamma rays from radiative muon decay, annihilation in flight of positrons, bremsstrahlung

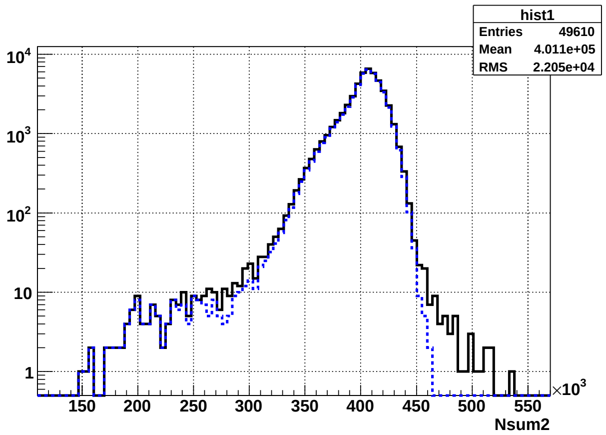

Figure 7.36: Nsum2 distribution of simulation before and after higher tail event cut.

of positrons and so on. The detection of this type of pile-ups can be done by time separation. Time separation is done by using time difference of the earliest PMT hit and the latest PMT hit in an event. When there are not pile-ups, it must be less than 4 nsec, while in the case of pile-ups, it can be larger than that. This method is sensitive when time difference of two gamma rays are larger than the threshold, while it can not find a pile-up when two gamma rays impinge almost at the same time, for example a gamma ray from a radiative muon decay and a that from AIF from the same muon decay. Another type of identification is done by using spacial hit pattern of PMTs. Figure 7.37 shows a hit pattern and 3D event display when two gamma rays enter the gamma ray detector. Triangles in the right figure show detected two peaks in the distribution. Identification power and miss-identification probability was studied by using MC simulation. Identification power and miss-identification probability depend on thresholds in the analysis and those must be adjusted according to noise level of the gamma ray detector in the experiment. When one uses the lower thresholds, identification power and miss-identification probability become larger. In a simulation study, when low thresholds were used to detect low energy pileups, identification power of time and space separations were 76 and 80 % respectively. By combining them, 95 % of pileups could be identified. Miss-identification probability of them were 2 and 10 % respectively.

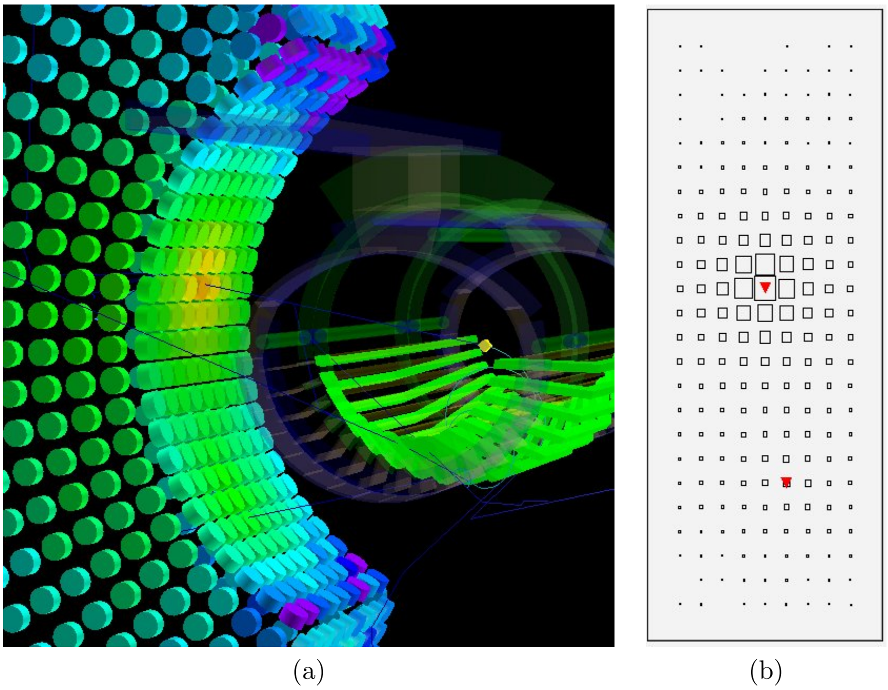
(a) (b)

Figure 7.37: Event display of pileup events in simulation and pileup identification.

7.5.3 Cosmic ray event rejection

Figure 7.38-a shows a spectrum of the gamma ray detector measured at the nominal position with beam off and the COBRA magnet on. The data was taken by the self-trigger of the detector. Since beam was off, most of these events must be from cosmic rays or secondary particles of a cosmic ray hitting on a structure in the experimental hall. For comparison, expected gamma ray spectrum from radiative muon decay(RD) and annihilation in flight(AIF) with assuming 3×10^7 muon stopping rate is shown in fig.7.38-b.

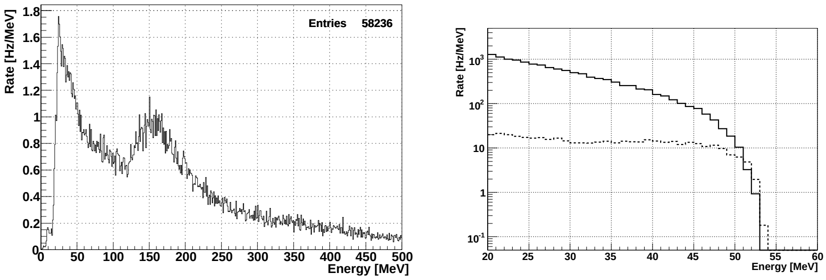

(a) (b)

Figure 7.38: (a) Measured cosmic ray spectrum. (b) Simulated spectrum of energy deposit in the gamma ray detector, from RD(solid line) and AIF(dashed line), with assuming 3×10^7 Hz muon stopping rate.

The rate of low energy backgrounds from cosmic rays is much lower than that from radiative muon decays or AIF. So, the probability of an accidental pileup of a gamma ray and a cosmic ray background must be much lower than pileup of two gamma rays. However, since the rate of cosmic rays is almost constant around the energy of $\mu^+ \to e^+\gamma$ signal, a probability that a cosmic mimics a signal is relatively high in a narrow energy window around the signal. Event rate of cosmic rays observed by the gamma ray detector is comparable with RD or AIF around the signal region, if we don't adopt any rejection of cosmic ray events.

Most of cosmic-ray event can be clearly distinguished from gamma ray events from the hit pattern of PMTs. Cosmic rays observed by the gamma ray detector can be classified like followings.

1. It enters from the inner/outer face and exits to outer/inner face.
2. It enters or exists from one of top, bottom, upstream or downstream face.
3. It enters from one of top, bottom, upstream, downstream or outer face, and it stops in the active volume.
4. It enters from the inner face, and it stops in the active volume.

In the case of (1), the minimum energy deposit is around 160 MeV which corresponds to 38.4 cm of path length (distance of two faces), and 4 MeV/cm energy deposit, which is reasonable for liquid xenon(z=54). So it does not look like a signal gamma ray because the deposit energy is too high. In the case of (2), when the energy deposit is close to the signal region, the position must be reconstructed outside of the fiducial volume. Most of all events of (1), (2) or (3) can be rejected with a selection of $Q_{inner2}/Q_{outer2} > 0.4$, even when energy and position are reconstructed in the signal box. Q_{inner2} and Q_{outer2} are weighted charge sum of PMTs on the inner and outer face respectively with the same factor of $Qsum2$.

Figure 7.39 shows Q_{inner2}/Q_{outer2} distribution during muon beam on and off. When muon beam is on, there are two peaks corresponding to cosmic ray events and gamma ray events. When muon beam if off, in most of events it is less than 0.4. By a cut of $Q_{inner2}/Q_{outer2} > 0.4$, 80 % of cosmic ray events can be rejected. Most of remaining events are (4). Figure 7.40 shows the same variable in simulated signal events and its depth reconstruction. The fraction of events cut by the selection is 3.7 %, and those events are mostly deep events for which resolutions are not as good as those for normal depth events.

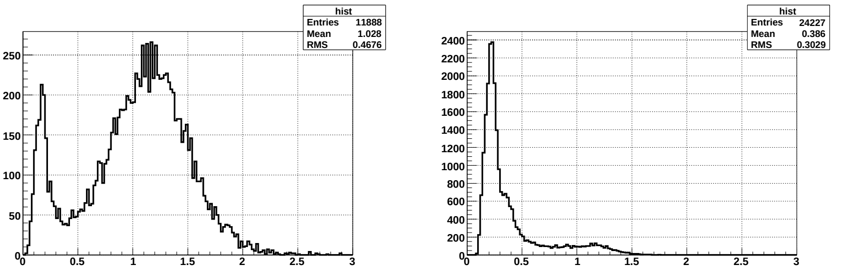

(a) (b)

Figure 7.39: Q_{inner2}/Q_{outer2} distribution during (a) muon beam on, and (b) muon beam off.

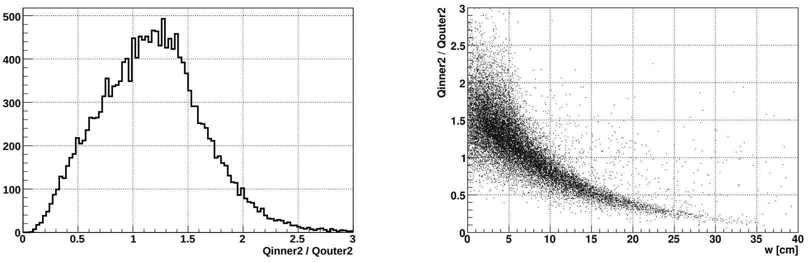

(a) (b)

Figure 7.40: (a) Q_{inner2}/Q_{outer2} distribution of simulated signal events. (b) Depth dependence of the variable.

Integrated rates of cosmic rays and gamma rays in fig.7.38 from 51 to 55 MeV, are 5 and 20 Hz respectively before the rejection of cosmic ray events. After the rejection, the rate of cosmic rays is 1/20 of that of gamma rays.

7.6 Summary and discussion on the gamma ray detector

In this chapter, reconstructions and calibrations of the gamma ray detector are described. The performance of the detector and the analysis was evaluated by using CEX data in 2007. The best resolutions in depth slices are summarised in table 7.2. With comparing to table 1.3 and table 5.1, all the resolutions are not as good as the requirements and worse than the prototype. The spacial resolution(5.9 mm in σ) corresponds to a contribution of 20 mrad. The time resolution (121 psec in σ) includes DRS time alignment resolution between the gamma ray detector and the tagging detector. Comparable number to the result of the large prototype is 0.21 nsec in FWHM with subtracting contribution of the alignment uncertainty. On the other hand, the uncertainty remains in time difference between a gamma ray and a positron in MEG physics run, and we have to compare 121 psec in σ(0.284 nsec in FWHM) with the goal. The rate of the accidental background, which is the dominating background, is approximately proportional to $(\Delta E_\gamma)^2 \cdot \Delta E_{e^+} \cdot (\Delta\theta_{\gamma e^+})^2 \cdot \Delta T_{\gamma e^+}$[58]. With assuming goal resolutions of the positron detector, the background event rate with these measured gamma ray resolutions is 4.4 times larger than the goal. The contributions of three resolutions are almost same (1.44, 1.67 and 1.82 by energy, time and position respectively).

	MEG goal	2007 (best)
ΔE_γ [%]	4.5~5.0	6.0
ΔE_{e^+} [%]	0.8	-
$\Delta\theta_{\gamma e^+}$ [mrad]	12.4~16.9	23.2(20.4)
$\Delta T_{\gamma e^+}$ [nsec]	0.18	0.301(0.284)
Acceptance × Efficiency [%]	>1.6	-
Muon stopping rate (10^8)	0.3(DC)	-
Running time [weeks]	100	-
Single event sensitivity(10^{-13})	0.5	-
90 % C.L. limit(10^{-13})	1.7	-

Table 7.2: The best resolutions in depth slices, measured in 2007 (FWHM). ΔE_γ is FWHM of fitting function of 54.9 MeV peak. σ of right edge of the function is 2.1 %. For $\Delta\theta_{\gamma e^+}$ and $\Delta T_{\gamma e^+}$, requirements for the positron detector (10.5 mrad and 100 psec) are included. For those resolutions, contributions of the gamma ray detector are written in parentheses. 20.4 mrad and 0.284 nsec in FWHM correspond to 5.9 mm and 121 psec in σ respectively.

There are two major sources which make the resolution worse. Observed amount of light in the final detector is much lower than expectation from the large prototype and MC simulation of the final detector. In 2007, amount of light was 1/3 of the expectation. According to the result of the large prototype(fig.5.31), when energy of gamma rays is 1/3 of 54.9 MeV, energy resolution can be worse than 2 %. Another factor which makes resolution worse is noise or instability of electronics. The effect can be evaluated approximately from the distribution of estimated energy for random trigger events. The distribution width corresponded to 2 % of 54.9 MeV in run 2007. Time resolution is affected by the low scintillation yield and alignment of time measurements of several DRS chips. The correction of event by event time jitter is done by using a common clock signal as described in section 7.3.1. As it can be seen in fig.7.12, the waveform is not very clean, and event-by-event variation of the waveform makes alignment uncertainty of 80 psec. The problem is a way to read the waveform on DRS chip, instead of the original waveform. Position resolution can be improved by better gain and Q.E. estimation of PMTs. To improve gain estimation, LEDs with higher attenuation factor were installed during a maintenance period after 2007 run. Q.E. estimation can be improved by optimizing parameters in MC simulation to reproduce alpha source events in the final detector well.

A prospect to improve scintillation yield and the DRS time alignment are discussed in section 9.2.

Three kinds of event type identification (higher tail event, cosmic ray and pile up) are described. In a study of MC simulation, higher tail events are successfully identified as shown in fig.7.35.

From rejection factor of cosmic ray events, which is estimated from measured cosmic ray spectrum, and an expected rate of single gamma rays from MC simulation, single event rate of cosmic ray event is 1/20 of that of gamma rays around the signal energy after a rejection. So background rate by cosmic rays will be negligible.

Event rate of pileup events was estimated from MC simulation with assuming the highest possible muon stopping rate (1×10^8) of the MEG. In an energy deposit region from 51 to 55 MeV, which is 2σ region of 2.1 % resolution, 90 % of events are pileup events. After the rejection, the rate becomes a half of single gamma events. Since the accidental rate is proportional to the square of the beam intensity, the fraction with the nominal beam rate(3×10^7) is nine times less than that. So if the performance is realized for experiment data, the rate of pileup events must be much lower than that of single gamma events in 2007 and 2008. The beam rate will be optimized for 2009 run based on the accidental event rate in 2008 result.

Figure 7.41 shows single spectrum of the gamma ray detector during physics run in 2007. Histograms for each event types are stacked on each other. Events included in the top most histogram is used for physics analysis in chapter 8. Note that the figure is single spectrum of the gamma ray detector, and event selection by using time and opening angle correlation with a positron is not done except for trigger requirement. So, absolute number of background event is much lower than the figure. A discussion after the event selection is done in the following chapter. Tail of the top most histogram is broader than an expectation based on the measured energy resolution. The broadness is equivalent to an energy resolution of 7.2 %. Possible reasons are remaining pileup events, or remaining non-uniformity of energy scale in the inner face. To understand the origin of those events, further studies are needed. How the spectrum affects the sensitivity is estimated in the following chapter by estimating number of backgrounds with assumed statistics in 2008 with using measured gamma ray spectrum after these event type identifications.

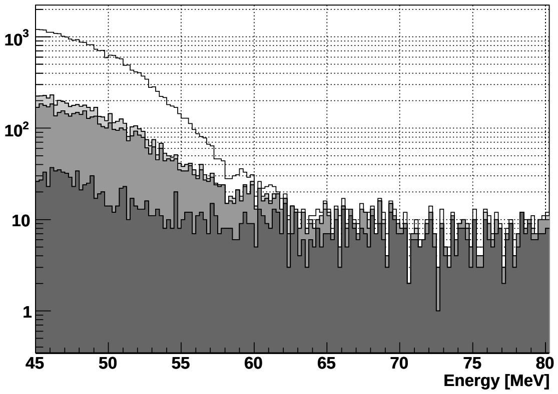

Figure 7.41: Spectrum of gamma ray of $\mu^+ \rightarrow e^+\gamma$ trigger data. Four spectra are shown for different event types identified by analysis. From the bottom, CR, pileup of two or more gamma rays, higher tail events. White one is after rejection of these events. Each histogram is stacked.

Chapter 8

The MEG Sensitivity

In the past $\mu^+ \rightarrow \mathrm{e}^+\gamma$ search experiments(MEGA and Crystal box), upper limit of branching ratio was calculated by maximum likelihood analysis. Likelihood analysis allows to take into account the shape of the signal and backgrounds, including correlation between variables. In this chapter, the upper limit of branching ratio from 2007 data is evaluated by using maximum likelihood analysis. In order to check performance of the detector for the sensitivity with more statistics, the sensitivity with assumed statistics in 2008 is evaluated by using Feldoman-Cousins approach[60].

8.1 Likelihood analysis with MEG 2007 data

In this section, we tried to estimate the upper limit of branching ratio by using data taken in 2007 engineering run, while it is clear that the statistics is not enough to improve the current experimental limit. So the purpose of this section is to demonstrate the physics analysis and understanding the current capability of the experiment, rather than estimating the upper limit. In this study, some simplification was utilized, because the statistics is much lower and the likelihood analysis is still under development.

- Only accidental background was considered. Rate of prompt background should be one order of magnitude less than accidental one from a calculation.
- Events with shallower gamma ray conversion than 2 cm were not used in the study. The resolutions are worse than normal events, so they should be less significant to sensitivity. In the real physics analysis in 2008 or later, they can be included with taking into account resolutions.
- It was assumed that pileup, cosmic ray, higher tail event identification works perfectly for signal events when the probability function is created. The effect of failure of identification must be taken into account in a real physics analysis in 2008 by using simulation.

In this analysis, resolutions written in table 8.1 were used for signal probability function(p.d.f.). For energy and opening angle, measured resolutions in

2007 were used. Since, in this analysis, common probability density functions are used all over the depth region of the gamma ray detector, resolution functions are broader than those with the best resolutions shown in table 7.2. When the development of the likelihood fit software is completed, the functions for each depth slice will be prepared. Since statistics in this analysis is very small, the fitting result must not be changed even if functions are prepared for each depth. Time coincidence resolution was measured in 2008 by using $\pi^0 \rightarrow \gamma e^+ e^-$ decay. In this analysis, a preliminary result of the measurement is used. The measured time coincidence resolution is worse than an expectation, which is $\sqrt{(0.175)^2 + (0.0587)^2} \times 2.35 = 0.43$ nsec in FWHM, from measured time resolutions of gamma ray detector for $w > 2$ cm, and an expected resolution of positron detector described in section 2.3.1. This can be due to errors of calibration to correct position dependence of time on the timing counter and/or the gamma ray detector. The investigation is still being done. To be conservative, the measured time resolution is used in this analysis.

For the data modeling and fitting, RooFit Toolkit[61] was used.

	MEG goal	MEG 2007
ΔE_γ [%]	4.5~5.0	6.4
ΔE_{e^+} [%]	0.8	2.2
$\Delta \theta_{\gamma e^+}$ [mrad]	12.4~16.9	30.2
$\Delta T_{\gamma e^+}$ [nsec]	0.18	0.82

Table 8.1: Resolutions of detector used in likelihood analysis, written in FWHM. Resolutions for positrons are measured in 2007[21]. Those for gamma rays are measured average resolutions for events deeper than 2 cm, which is described in section 7. ΔE_γ is FWHM of fitting function of 54.9 MeV peak in CEX test. The function is shown in fig.8.2-a. Time coincidence resolution is a preliminary result from a measurement of $\pi^0 \rightarrow \gamma e^+ e^-$ decay during CEX test in 2008.

The analysis was done for 21 events in analysis box. Event selection was done by following conditions.

- $46 \leq E_\gamma \leq 60$ MeV
- $50 \leq E_e \leq 56$ MeV
- $\cos\theta_{e\gamma} \leq -0.99145$
- $|\Delta T_{e\gamma}| \leq 1.75$ nsec
- Acceptance cut for positrons. $|\cos\theta_e| \leq 0.35$ and $|\phi_e| \leq 60°$, where (θ_e, ϕ_e) is a direction of a positron at the muon decay point.
- Acceptance cut for gamma rays. $|u| \leq 24.8$ cm, $|v| \leq 71.1$ cm and $w \geq 2$ cm, where (u,v,w) is a hit position in the gamma ray detector.
- Pileup, cosmic ray and higher tail event rejection described in section 7.

Selections by gamma ray energy(E_γ), positron energy(E_e) and time difference($T_{e\gamma}$) correspond to 5σ region of each variable. A selection by opening angle($\cos\theta_{e\gamma}$)

was done by wider region than 5σ in order to increase number of events for the analysis. The result is independent of the size of analysis box. Figure 8.1 shows a distribution of the selected events for four variables.

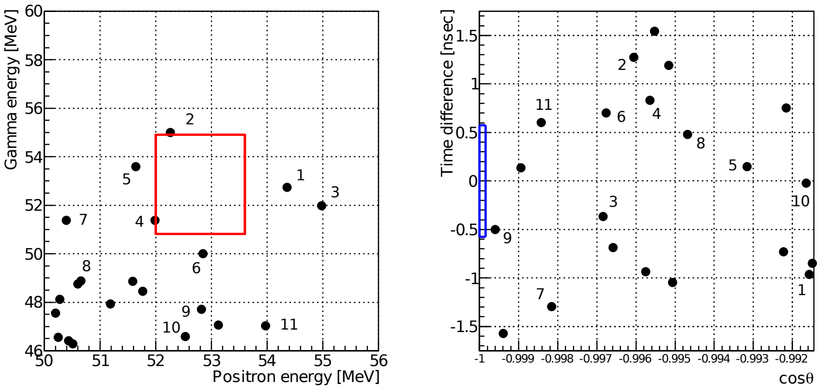

Figure 8.1: Distribution of selected 21 events for gamma and positron energy (left) and time difference and opening angle(right). For some events, event number is assigned to show correspondence in two plots. Boxes in the plots show 1.64σ region.

8.1.1 Building likelihood function

The partial probability to measure i-th observed event with parameters $\boldsymbol{x}_i$ can be defined to be

$$P(\boldsymbol{x}_i) = N_{\mathrm{sig}}S(\boldsymbol{x}_i) + N_{\mathrm{RD}}S'(\boldsymbol{x}_i) + N_{\mathrm{BG}}B(\boldsymbol{x}_i) \tag{8.1}$$

$$N = N_{\mathrm{sig}} + N_{\mathrm{RD}} + N_{\mathrm{BG}} \tag{8.2}$$

where N_{sig}, N_{RD}, N_{BG} are number of events of signals, prompt backgrounds and accidental pileups respectively.

The extended maximum likelihood method is used in this analysis to estimate absolute number of signals, instead of fraction of it. The extended likelihood function can be written as

$$\mathcal{L}(N_{\mathrm{sig}}, N_{\mathrm{RD}}, N_{\mathrm{BG}}) = Q(N; N_{\mathrm{exp}}) \prod P(\boldsymbol{x}_i) \tag{8.3}$$

$$Q(N; N_{\mathrm{exp}}) = N_{\mathrm{exp}}^{N} e^{-N_{\mathrm{exp}}}/N! \tag{8.4}$$

where N_{exp} is a fitting parameter to estimate the absolute normalization. In this analysis following observables were used to build the likelihood function.

E_γ	Energy of a gamma ray
E_e	Energy of a positron
$T_{e\gamma}$	Time difference of a gamma ray and a positron
(u, v, w)	First interaction position of a gamma ray written in a local coordinate system of the gamma ray detector
(x, y, z)	Muon decay vertex position
$(\cos\theta_e, \phi_e)$	Initial direction of a positron

8.1.2 Probability density functions

p.d.f. of signals

S was defined to be

$$
\begin{aligned}
S(E_\gamma, E_e, u, v, w, x, y, z, \cos\theta_e, \phi_e, T_{e\gamma}) &= S_1(E_\gamma | E_e, u, v, w, x, y, z, \cos\theta_e, \phi_e, T_{e\gamma}) \cdot \\
&\quad S_2(E_e | u, v, w, x, y, z, \cos\theta_e, \phi_e, T_{e\gamma}) \cdot \\
&\quad S_3(T_{e\gamma} | u, v, w, x, y, z, \cos\theta_e, \phi_e) \cdot \\
&\quad S_4(u, v, \cos\theta_e, \phi_e | w, x, y, z) \cdot \\
&\quad S_5(w | x, y, z) \cdot \\
&\quad S_6(x, y, z) \qquad (8.5)
\end{aligned}
$$

where S_6 is muon stopping distribution, and S_5 is depth distribution of the first interaction position of gamma rays in the gamma ray detector. Each function from S_1 to S_6 is normalized. S_6 is created from measured beam profile and target geometry. S_5 is created from measured depth distribution in the gamma ray detector. S_1, S_2, S_3 and S_4 are identical to the response functions of the detector in this study because the kinematics is monochromatic for E_γ, E_e, $T_{e\gamma}$ and $\theta_{e\gamma}$. S_2, S_3 and S_4 are approximated by Gaussian functions with a variance of the detector resolutions. S_1 is not a Gaussian, but a function written in paragraph 5.2.3. Response functions for gamma rays and positrons were created independently. For positrons, response functions were created by using Michel decay data. For gamma rays, response functions were created from 54.9 MeV peak of pion charge exchange data. Figure 8.2 shows S_1, S_2 and S_3.

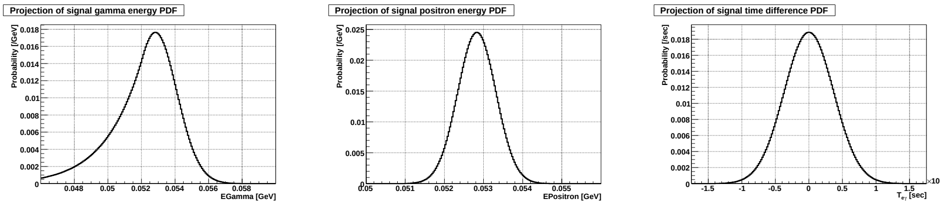

(a) (d) (c)

Figure 8.2: Probability density functions of (a)gamma energy, (b)positron energy and (c)time difference for signals. These were created from measured detector responses.

p.d.f. of accidental backgrounds

B was defined to be

$$
\begin{aligned}
B(E_\gamma, E_e, u, v, w, x, y, z, \cos\theta_e, \phi_e, T_{e\gamma}) &= B_1(E_\gamma | E_e, u, v, w, x, y, z, \cos\theta_e, \phi_e, T_{e\gamma}) \cdot \\
&\quad B_2(E_e | u, v, w, x, y, z, \cos\theta_e, \phi_e, T_{e\gamma}) \cdot \\
&\quad B_3(T_{e\gamma} | u, v, w, x, y, z, \cos\theta_e, \phi_e) \cdot \\
&\quad B_4(u, v, \cos\theta_e, \phi_e | w, x, y, z) \cdot \\
&\quad B_5(w | x, y, z) \cdot \\
&\quad B_6(x, y, z) \qquad (8.6)
\end{aligned}
$$

For accidental pileup backgrounds, distributions of gamma rays and positrons must be independent by definition. Hence, p.d.f. can be created separately.

B_1 and B_5 were created by using off-center events in time from RD trigger data. B_2 and B_6 were created from Michel trigger data. B_4 was created from random combinations of an off timing gamma ray and a positron. B_3 must be 1 by definition. B_6 is same with S_6.

Figure 8.3 shows gamma ray spectrum during $\mu^+ \rightarrow \mathrm{e}^+\gamma$ data taking. Events in the acceptance and deeper than 2 cm are included in histograms. A histogram in 8.3-b is used as B_1.

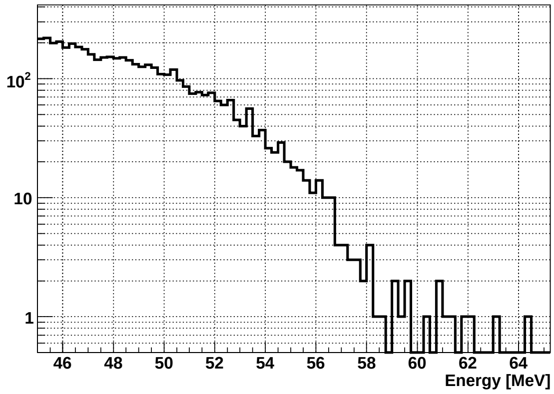

Figure 8.3: Background spectrum of gamma rays. Cosmic ray, pileup and higher tail event rejections are done. $e^+\gamma$ coincident events are excluded by requiring $T_{e\gamma} > 2$ nsec to obtain spectrum of accidental pileup events.

8.1.3 Upper limit from 2007 physics run

The mean value of the maximum likelihood fitting of N_{signal} is 1.02×10^{-7}. The 90 % confidence limit is the value of N_{signal} where 90 % of the likelihood distribution is covered. The limit was obtained from integration of a curve in fig.8.4-c. This value is 2.7 events. Figure 8.5 shows distribution of four variables together with fitting result.

If we use numbers listed in table 8.2, 90 % C.L. upper limits of the branching ratio of $\mu^+ \rightarrow \mathrm{e}^+\gamma$ can be calculated to be 1.2×10^{-10}.

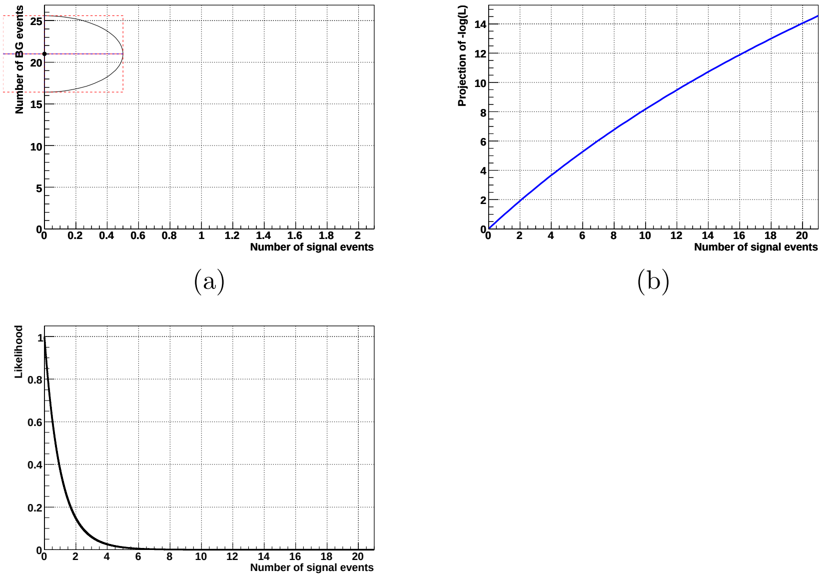

(a)

(b)

(c)

Figure 8.4: Result of likelihood fitting. (a) Center value and one sigma region of number of signal and background events. Sigma is statistical error of likelihood fitting by MINUIT. (b) Projection of $-\log(\text{likelihood})$ as a function of number of signal events. (c) Projection of likelihood function as a function of number of signal events.

Running time [weeks]	0.13
Number of stopped muons	1.89×10^{12}
Acceptance(%)	9
Gamma detection efficiency(%)	30.7
Positron detection efficiency(%)	43.8

Table 8.2: Numbers used for normalization to translate number of signals into the branching ratio in this work. Gamma detection efficiency is lower than a normal value, because in this study shallower events than 2 cm was not used.

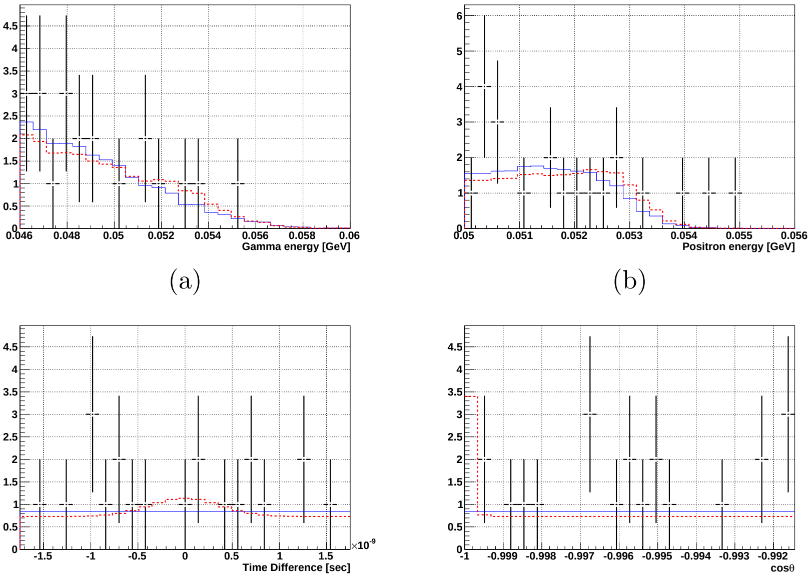

(a) (b)

(c) (d)

Figure 8.5: Projected distributions of 21 events for (a)gamma energy, (b)positron energy, (c)time difference and (d)opening angle. Solid lines show best fit curves and dashed line show 90 % C.L. upper limit of number of signals.

8.2 Sensitivity estimation for run 2008

In this section, expected sensitivity of MEG run 2008 is estimated by Feldoman-Cousins approach[60]. It is assumed that bad channels of the drift chambers would be solved and run with full expected efficiency. For gamma ray detector, an increase of amount of light by purification is taken into account. Numbers in table 8.3 were used for the estimation. In the estimation, signal region is defined as a region of 90 % cut determined by the detector resolutions for each variable. As it is discussed in section 8.1, a preliminary time resolution measured in 2008 is worse than an expectation. To be conservative, the measured resolution is used also in this analysis.

	MEG goal	MEG 2008 expectation
ΔE_γ [%]	4.5∼5.0	6.0
ΔE_{e^+} [%]	0.8	1.5
$\Delta\theta_{\gamma e^+}$ [mrad]	12.4∼16.9	21.0
$\Delta T_{\gamma e^+}$ [nsec]	0.18	0.82
Acceptance × Efficiency [%]	>1.6	1.7
Muon stopping rate (10^8)	0.3(DC)	0.3(DC)
Running time [weeks]	100	11
Single event sensitivity(10^{-13})	0.5	-
90 % C.L. limit(10^{-13})	1.7	-

Table 8.3: Expected conservative performance in MEG 2008. Numbers are written in FWHM. γ efficiency includes cut by $w > 2$ cm. Resolutions of the gamma ray detector are preliminary performance measured in 2008. Resolutions of the positron detector is expectation from MC in full condition[21].

8.2.1 Prompt background

Background event rate of single radiative decay can be calculated using the formula given in [62][63][64][65] with taking into account resolutions of the detector. With using expected resolutions in 2008, the contribution of prompt background can be found to be much smaller than that of accidental background.

8.2.2 Accidental background

Number of accidental background can be written as

$$N_{acc} = \left(n_\mu \cdot f_e^0 \cdot \frac{\Omega}{4\pi} \cdot \epsilon_e\right) \cdot \left(n_\mu \cdot f_\gamma^0 \cdot \frac{\Omega}{4\pi} \cdot \epsilon_\gamma\right) \times \left(\frac{\delta\omega}{\Omega}\right) \cdot (2\delta t) \cdot T \cdot f_{P_\mu} \quad (8.7)$$

where n_μ is muon stopping rate, δt is a timing coincidence resolution, Ω is acceptance of the detector, $\delta\omega$ is opening angle resolution and T is DAQ livetime, ϵ_e and ϵ_γ are detection efficiency for positrons and gamma rays respectively. f_e^0 and f_γ^0 are the fractions of the spectrum within the signal box of the positrons in the Michel muon decay and photons in the radiative muon decay respectively. They include their branching ratios. f_{P_μ} is a background suppression factor when a muon is polarized. In this discussion $f_{P_\mu} = 1$ is considered. The effective branching ratio can be obtained by

$$B_{acc} = \frac{N_{acc}}{n_\mu \cdot T \cdot \left(\frac{\Omega}{4\pi}\right) \cdot \epsilon_e \cdot \epsilon_\gamma} = n_\mu \cdot f_e^0 \cdot f_\gamma^0 \cdot \left(\frac{\delta\omega}{4\pi}\right) \cdot (2\delta t)\,. \tag{8.8}$$

f_e^0 is obtained by integrating Michel muon spectrum in the signal region. It is approximately $2 \times \delta x$, where x is positron energy divided by 52.8 MeV and $deltax$ is resolution of x. $n_\mu \cdot f_\gamma^0$ is obtained from p.d.f. of background gamma rays. Normalization can be obtained from single counting rate of the gamma ray detector with taking into account selection in analysis. By incorporating above, effective branching ratio is estimated to be 1.2×10^{-13}. In order to estimate sensitivity in 2008, we assume 5×10^6 of DAQ time for physics runs from September to December. During this period calibration runs are also taken. DAQ live time would be about 85 % of it. The total livetime corresponds to about 11 weeks with the same normalization in table 1.3.

Single event sensitivity can be simply calculated from these numbers and efficiencies to be 4.4×10^{-13}. 90 % C.L. upper limit of null experiment can be estimated by using Feldoman-Cousins approach described in ref.[60]. Number of backgrounds expected from parameters in this section is 0.27. Using the expected number of backgrounds, the 90 % C.L. upper limit of null experiment is calculated to be 9.4×10^{-13}.

Chapter 9

Summary and prospects

9.1 Summary

A new type of gamma ray detector where many PMTs surround a single active volume was developed. The development was done in three steps, the small prototype, the large prototype and the final detector. During the prototype test, fundamental techniques for operation of large xenon detector, purification, measurement of scintillation photons and analysis were developed. By using the large prototype, resolutions of energy and time for 54.9 MeV and position resolution for 40 MeV gamma ray were measured to be 1.2 %, 43 psec and 4.3 mm respectively. Construction of the final detector was started from testing and measuring properties of all the PMTs individually. The cryostat with thin and wide entrance window was built and it was passed all the hardware tests.

In 2007, the first operation of the gamma ray detector was done starting from purification of xenon. After finishing purification, the first engineering run of MEG with all the sub-detector was conducted. CEX data was taken to evaluate performance of the gamma ray detector in limited region of the acceptance. The best resolutions of energy, time and position in depth slices were estimated to be 2.1 ± 0.2 %, 5.9 ± 1.4 mm and 121 ± 8 psec respectively. A small amount of physics data was taken in the engineering run. A simplified likelihood analysis was done to demonstrate that to be done with much more statistics in 2008. The 90 % CL upper limit of BR($\mu^+ \to e^+\gamma$) from 2007 data is 1.2×10^{-10}. By using measured resolutions and background spectrum, it was confirmed that the gamma ray detector has a good enough performance to carry out $\mu^+ \to e^+\gamma$ search experiment with a better sensitivity than 1×10^{-12} in 2008.

9.2 Prospects

The resolutions of the final gamma ray detector are worse than the result of the large prototype, mainly due to low amount of light and noise of electronics. Observed amount of light in the final detector in 2007 was 1/3 of expectation, while absorption of scintillation does not seem so much. In 2008, it was found that amount of light has a correlation with operation of liquid nitrogen for cooling. So it is most likely that there is a small leak of nitrogen from the cooling pipe only when the part is cooled. Nitrogen contamination can decrease amount of scintillation as discussed in section 3.1.1. In 2007, purification was done by molecular sieves which mainly eliminate water. In addition to that, in 2008, a purifier by using copper beads was introduced to eliminate also oxygen, which may exist in liquid xenon due to outgas. After finding the possible leak, we stopped using the cooling pipe and started using alternative one. After a purification, amount of light was increase by factor 1.8 with respect to that in 2007. Even after the factor 1.8 improvement, it is still increasing by operating purification. If the amount of light is three times larger, all the resolutions are expected to be improved significantly.

In 2008, a search of noise sources was done and burst noise from power supply of VME crates and noise correlated with VME signals were found. It was found that noise is picked up by flat cables running near VME crates. To fix the problem, flat cables were shielded and the noise was reduced. Noise correlated with VME signals were reduced by increasing interval of polling to check status of VME modules.

Time resolution is degraded by alignment of time measurements of several DRS chips. A new version of DRS (version 4) is expected to be introduced from 2009 to improve many aspects of readouts, including an improvement of clock waveform readout. DRS2 has some other problems, noise induced by clock, large cross talks, unstable baseline offsets, temperature dependent response, fake signals due to calibration variation and remaining charge by large pulse in the previous loop. The collaboration is trying to decrease effect of these problems both in the operation and analysis, however there are remaining effects to resolutions. DRS4 is expected to solve some of these problems.

In 2007, because of limited beam time, the study of performance of gamma ray was done in limited positions in the acceptance. In 2008, the full scan of all the acceptance is done. Detailed study for non-uniformity and long term stability will be done. Detection efficiency of the gamma ray detector will be measured in 2008 by counting number of hits of the gamma ray detector in single trigger data by the tagging detector in CEX test.

In 2007, about 25 % of cells of the drift chambers had some problems mainly due to disconnection of loose connectors or H.V. discharges. Many of them are fixed in 2008. Further study to fix discharges are being done. z measuring timing counter was not in operation due to problems of readout electronics. When it is in operation determination of z hit position on timing counter will be improved. Then reconstruction of muon decay time from positron spectrometer will be improved.

Calculation of expected sensitivity in 2008 was done with assuming a full efficiency of the positron spectrometer, and it was calculated to be 9.4×10^{-13}. The number is one order of magnitude improvement from the current experimental upper limit (1.2×10^{-11}). MEG will make a new limit in 2008 and will continue improvements of apparatus and analysis, and will continue to collect more statistics after 2008 for even higher sensitivity.

Bibliography

[1] Y. Kuno and Y. Okada, Rev. Mod. Phys. **73**, 151 (2001).

[2] G. W. Bennett *et al.*, Phys. Rev. Lett. **89**, 101804 (2002).

[3] G. W. Bennett *et al.*, Phys. Rev. Lett. **89**, 129903 (2002).

[4] G. W. Bennett *et al.*, Phys. Rev. Lett. **92**, 161802 (2004).

[5] G. W. Bennett *et al.*, Phys. Rev. D **73** (2006).

[6] W.-M. Yao *et al.*, Journal of Physics G **33**, 1+ (2006).

[7] J. Hisano and K. Tobe, Physics Letters B **510**, 197 (2001).

[8] M. L. Brooks *et al.*, Phys. Rev. Lett. **83**, 1521 (1999).

[9] R. D. Bolton *et al.*, Phys. Rev. D **38**, 2077 (1988).

[10] U. Bellgardt *et al.*, Nuclear Physics B **299**, 1 (1988).

[11] C. Dohmen *et al.*, Physics Letters B **317**, 631 (1993).

[12] W. Honecker *et al.*, Phys. Rev. Lett. **76**, 200 (1996).

[13] W. Bertl *et al.*, The European Physical Journal C **47**, 337 (2006).

[14] P. Depommier *et al.*, Phys. Rev. Lett. **39**, 1113 (1977).

[15] A. van der Schaaf *et al.*, Nuclear Physics A **340**, 249 (1980).

[16] W. W. Kinnison *et al.*, Phys. Rev. D **25**, 2846 (1982).

[17] D. Anderson, H. Arvela, A. Breskin, and G. Charpak, Nucl. Instr. and Meth. **224**, 315 (1984).

[18] D. Green, H. Haggerty, S. Hansen, and M. Takasaki, Nucl. Instr. and Meth. A **256**, 305 (1987).

[19] J. Allison *et al.*, Nucl. Instr. and Meth. A **310**, 527 (1991).

[20] Y. Ajima *et al.*, Nucl. Instr. and Meth. A **443**, 71 (2000).

[21] H. Nishiguchi, *An Innovative Positron Spectrometer to Search for the Lepton Flavour Violating Muon Decay with a Sensitivity of* 10^{-13}, PhD thesis, University of Tokyo, 2008.

[22] S. Ritt, Nucl. Instr. and Meth. A **518**, 470 (2004).

[23] D. Zahnow, C. Rolfs, S. Schmidt, and H. P. Trautvetter, Z. Phys. **359**, 211 (1997).

[24] F. E. Cecil *et al.*, Nucl. Phys. A **539**, 75 (1992).

[25] T. Doke, Portugal Phys. **12**, 9 (1981).

[26] D. R. Lide, *CRC Handbook of Chemistry and Physics 2004-2005* (CRC Press, Boca Raton, FL, 2004).

[27] J. Jortner, L. Meyer, S. A. Rice, and G. E. Wilson, J. Chem. Phys. **42**, 4250 (1965).

[28] N. Schwenter, E.-E. Koch, and J. Jortner, *Electronic Excitations in Condensed Rare Gases* (Springer-Verlag, Berlin, 1985).

[29] L. M. Barkov, A. A. Grebenuk, N. M. Ryskulov, P. Y. Stepanov, and S. G. Zverev, Nucl. Instr. and Meth. A **379**, 482 (1996).

[30] V. N. Solovov *et al.*, Nucl. Instr. and Meth. A **516**, 462 (2004).

[31] G. M. Seidel, R. E. Lanou, and W. Yao, Nucl. Instr. and Meth. A **489**, 189 (2002).

[32] T. Doke *et al.*, Jpn. J. Appl. Phys. **41**, 1538 (2002).

[33] A. Braem *et al.*, Nucl. Instr. and Meth. A **320**, 228 (1992).

[34] V. Y. Chepel, M. I. Lopes, R. Ferreira Marques, and A. J. P. L. Policarpo, Nucl. Instr. and Meth. A **349**, 500 (1994).

[35] N. Ishida *et al.*, Nucl. Instr. and Meth. A **384**, 380 (1997).

[36] T. Doke and K. Masuda, Nucl. Instr. and Meth. A **420**, 62 (1999).

[37] L. Landau and E. Lifshitz, *Electrodynamics of Continuous Media, 2nd edition* (Pergamon Press, Oxford, 1984).

[38] V. A. Rabinovich, A. A. Vasserman, V. I. Nedostup, and L. S. Veksler, National Standard Reference Data Service of the USSR. Translation. **10**, 622 (1988).

[39] K. WATANABE and M. ZELIKOFF, J. Opt. Soc. Am. **43**, 753 (1953).

[40] K. Watanabe, E. C. Y. Inn, and M. Zelikoff, The Journal of Chemical Physics **21**, 1026 (1953).

[41] K. Yoshino, J. R. Esmond, W. H. Parkinson, K. Ito, and T. Matsui, Chemical Physics **211**, 387 (1996).

[42] K. Yoshino, J. R. Esmond, W. H. Parkinson, K. Ito, and T. Matsui, Chemical Physics **215**, 429 (1997).

[43] R. Acciarri *et al.*, Effects of nitrogen contamination in liquid argon, 2008, nucl-ex/0804.1217.

[44] R. Acciarri *et al.*, Oxygen contamination in liquid argon: combined effects on ionization electron charge and scintillation light, 2008, nucl-ex/0804.1222.

[45] *Omni NuPure III*, http://www.nupure.com.

[46] A. Baldini *et al.*, Nucl. Instr. and Meth. A **545**, 753 (2005).

[47] S. Mihara *et al.*, Cryogenics **44**, 223 (2004).

[48] S. Mihara *et al.*, Cryogenics **46**, 688 (2006).

[49] A. M. Baldini *et al.*, Nucl. Instr. and Meth. A **566**, 294 (2006).

[50] *MSCB*, http://midas.psi.ch/mscb.

[51] *Labview*, http://www.ni.com.

[52] T. Miyazawa, Development of liquid xenon calorimeter for $\mu \to e\gamma$ experiment, Master's thesis, University of Tokyo, 1999, http://meg.web.psi.ch/docs/theses/miyazawa.pdf (in Japanese).

[53] K. Ozone, Timing resolution of liquid xenon gamma-ray detector for $\mu \to e\gamma$ decay search experiment, Master's thesis, University of Tokyo, 2000, http://meg.web.psi.ch/docs/theses/ozone.pdf (in Japanese).

[54] K. Ozone, *Liquid Xenon Gamma-ray Detector for the New* $\mu \to e\gamma$ *Search Experiment*, PhD thesis, University of Tokyo, 2005, http://meg.web.psi.ch/docs/theses/ozoned.pdf.

[55] M. Miyajima, S. Sasaki, and E. Shibamura, Nucl. Instr. and Meth. B **63**, 297 (1992).

[56] A. Bay *et al.*, Nucl. Instr. and Meth. A **271**, 497 (1988).

[57] F. Bourgeois, A. Corre, J. P. Marcelin, A. Meyrier, and G. Schuler, IEEE TNS **34**, 240 (1987).

[58] M. Toshinori *et al.*, Research Proposal to Paul Scherrer Institut, R-99-05 (1999).

[59] W. Xi, Engineering Fracture Mechanics **52**, 199 (1995).

[60] G. J. Feldman and R. D. Cousins, Phys. Rev. D **57**, 3873 (1998).

[61] W. Verkerke and D. Kirkby, The roofit toolkit for data modeling, 2003, physics/0306116.

[62] Y. Kuno, A. Maki, and Y. Okada, Phys. Rev. D **55**, R2517 (1997).

[63] Y. Kuno and Y. Okada, Phys. Rev. Lett. **77**, 434 (1996).

[64] C. Fronsdal and H. Überall, Phys. Rev. **113**, 654 (1959).

[65] S. G. Eckstein and R. H. Pratt, Ann. Phys. **8**, 297 (1959).

Acknowledgements

The MEG experiment is done by a collaboration of University of Tokyo, KEK, Waseda University, PSI, INFN Pisa, INFN and University of Genova, INFN and University of Pavia, INFN and University of ROME I, INFN and University of Lecce, BINP Novosibirsk, JINR Dubna and University of California Irvine.

The construction of the new liquid xenon gamma ray detector was done on efforts of many persons. To take physics data, a huge amount of effort for all the sub-detectors, beam, DAQ and triggers were needed. It was possible to perform analysis and simulation by gathering implementations by many persons. All these things were done with a decade of works. Here I can not write all the names, however I appreciate all the persons contributed MEG experiment, and persons who supported or educated me.

Prof. Toshinori Mori is one of spokes persons of the MEG experiment. He gave me a chance to work in MEG experiment for the gamma ray detector and responsible positions in the collaboration. He always gave me important suggestions directly or indirectly, and lead me to the correct direction.

I joined the MEG experiment when I belonged to Waseda University. Prof. Tadayoshi Doke, Prof. Jun Kikuchi and Prof. Satoshi Suzuki are very experts of any kinds of xenon detectors, and I learned important basics at that time. Dr. Kazuhiro Terasawa is the first person who taught me about experiment. From Prof. Masaki Yamashita, I learned many technical things and how interesting experiment is.

Prof. Satoshi Mihara developed the gamma ray detector of the MEG as the group leader. I could gain valuable experience when I try to complete tasks suggested by him. I learned a lot of things during working with Dr. Wataru Ootani, or enjoying interesting logical discussions. The development and operations of the gamma ray detector wouldn't be done without Dr. Toshiyuki Iwamoto's much reliable works. I learned about software and computers from Dr. Shuei Yamada.

I learned many things from Dr. Kenji Ozone during the prototype tests. Without his support, I couldn't have been involved in the experiments as I could. Dr. Hajime Nishiguchi mainly worked for the development of the drift chamber. However actually, he contributed also for the development and experiments for the gamma ray detector very much. I thank him also for his helps in my Swiss life. Yasuko Hisamatsu made grate contributions to the development of the PMT. Her contribution for analysis and simulation are also important. I thank her help in Tokyo for my activities in Switzerland. Analysis of the gamma ray detector would be incomplete without contributions of Yusuke Uchiyama. He is contributing not only to the gamma ray detector, but also for analysis of positron spectrometer and physics. Works of Hiroaki Natori may not be highly visible necessarily, but his reliable works were important to develop the gamma ray detector. Calibration of the gamma ray detector by using pion decays could be done by using a tagging detector developed by Yasuhiro Nishimura. I would appreciate Toshiya Mitsuhashi and Takefumi Yoshimura for works for the large prototype tests and PMT development. I would like to appreciate Prof. Satoru Yamashita for comments and advices.

The operation of the liquid xenon system is done by using refrigerators developed by Prof. Tom Haruyama. He contributed whole the design of the liquid xenon system. He also supported activities of MEG group during the large prototype tests in KEK. I thank grate technical supports by Katsuyu Kasami. I would like to appreciate Prof. Akihiro Maki for comments and advices.

The development of the gamma ray detector and its analysis were done by cooperation of Japanese group and INFN Pisa group lead by Prof. Alessandro Baldini. Dr. Donato Nicoló and Dr. Giovanni Signorelli have been working together with me since the large prototype tests. Dr. Fabrizio Cei has been contributing analysis and simulations also since the large prototype tests. Giovanni Gallucci participated the construction of the gamma ray detector. Calibration of the gamma ray detector by using nuclear reactions could be done by a C.W. accelerator proposed, prepared and operated by Prof. Calro Bemporad, Dr. Giovanni Signorelli and Angela Papa.

Dr. Stefan Ritt was my super visor in Switzerland. He developed great DAQ system, DRS and slow control system. I learned practice of designing systems from discussions with him and his works. Dr. Matthias Schneebeli developed the framework of the MEG analysis software. He improved the framework from our feedback in the prototype tests. He developed a software library for DRS readout and analysis of the drift chambers. Analysis of the drift chamber used in this thesis was done by implementation of mainly by him and Fedor Ignatov. Dr. Jonny Egger and Dr. Malte Hildebrandt developed the drift chambers. Dr. Malte Hildebrandt helped me not only for experiment, but also for my life in Switzerland. The muon beam line system was built by Dr. Peter-Raymond Kettle and Dr. Dimitri Grigoriev. I thank Dr. Valeri Markshin who has been supporting the computing system of MEG.

Discussions with Prof. William Molzon and his group members, Dr. Vladimir L. Tumakov, Paul Huwe, Feng Xiao, Christina Topchan and Ben Golden were very constructive. The group prepared the gas control system of the spectrometer and the muon target. The timing counter system construction was lead by Prof. Giorgio Cecchet, Dr. Flavio Gatti and Dr. Simeone Dussoni. Analysis and simulation of the timing counter is done by a coordination of Dr. Paolo Cattaneo. The trigger system were successfully prepared to take physics data by great works by Dr. Marco Grassi, Dr. Donato Nicoló and Luca Galli.

There are no words to express my deep appreciation to my parents Tetsuhide and Reiko Sawada.